

2009

Tribological behavior and film formation mechanisms of carbon nanopearls

Chad Nicholas Hunter
University of Dayton

Follow this and additional works at: https://ecommons.udayton.edu/graduate_theses

Recommended Citation

Hunter, Chad Nicholas, "Tribological behavior and film formation mechanisms of carbon nanopearls" (2009). *Graduate Theses and Dissertations*. 3434.
https://ecommons.udayton.edu/graduate_theses/3434

This Dissertation is brought to you for free and open access by the Theses and Dissertations at eCommons. It has been accepted for inclusion in Graduate Theses and Dissertations by an authorized administrator of eCommons. For more information, please contact mschlange1@udayton.edu, ecommons@udayton.edu.

**TRIBOLOGICAL BEHAVIOR AND FILM FORMATION
MECHANISMS OF CARBON NANOPEARLS**

Dissertation

Submitted to

**The School of Engineering of the
UNIVERSITY OF DAYTON**

In Partial Fulfillment of the Requirements for

The Degree

Doctor of Philosophy in Materials Engineering

by

Chad Nicholas Hunter

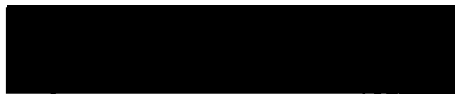
UNIVERSITY OF DAYTON

Dayton, Ohio

May 2009

TRIBOLOGICAL BEHAVIOR AND FILM FORMATION MECHANISMS OF
CARBON NANOPEARLS

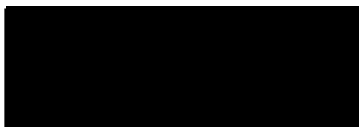
APPROVED BY:



Andrey A. Voevodin, Ph.D.
Committee Chairman
Professor, Materials Engineering



Charles E. Browning, Ph.D.
Committee Member
Professor, Materials Engineering



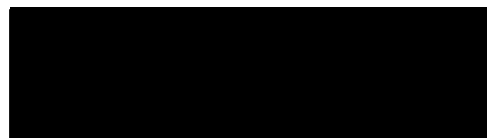
Daniel Eylon, D.Sc.
Committee Member
Professor and Director,
Materials Engineering



Christopher Muratore, Ph.D.
Committee Member
Research Scientist,
Universal Technology Corporation



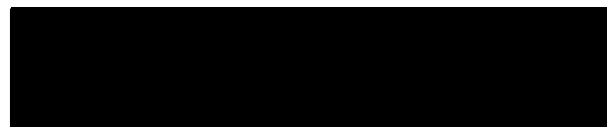
P. Terrence Murray, Ph.D.
Committee Member
Professor, Materials Engineering



Gerald J. Shaughnessy, M.S.
Committee Member
Associate Professor, Mathematics



Malcolm W. Daniels, Ph.D.
Associate Dean
School of Engineering



Joseph E. Saliba, Ph.D., P.E.
Dean, School of Engineering

ABSTRACT

Carbon nanopearls (CNPs) are amorphous carbon spheres that contain concentrically-oriented nanometer-sized graphitic flakes. Because of their spherical shape, size (~150 nm), and structure consisting of concentrically oriented nano-sized sp^2 flakes, CNPs are of interest for tribological applications, in particular for use in solid lubricant coatings. These studies were focused on investigating mechanisms of CNP lubrication, development of methods to deposit CNP onto substrates, synthesizing CNP-gold hybrid films using Matrix Assisted Pulsed Laser Evaporation (MAPLE) and magnetron sputtering, and studying plasmas and other species present during film deposition using an Electrostatic Quadrupole Plasma (EQP) analyzer. CNPs deposited onto silicon using drop casting with methanol showed good lubricating properties in sliding contacts under dry conditions, where a transfer film was created in which morphology changed from nano-sized spheres to micron-sized agglomerates consisting of many highly deformed CNPs in which the nano-sized graphene flakes are sheared from the wrapped layer structure of the CNPs. The morphology of carbon nanopearl films deposited using a MAPLE system equipped with a 248 nm KrF excimer laser source was found to be influenced by multiple factors, including composition of the matrix solvent, laser energy and repetition rate, background pressure, and substrate temperature. The best parameters for depositing CNP films that are disperse, droplet-free and have the maximum amount of material deposited

are as follows: toluene matrix, 700 mJ, 1 Hz, 100°C substrate temperature, and unregulated vacuum pressure.

During depositions using MAPLE and sputtering in argon, electron ionization of toluene vapor generated from the MAPLE target and charge exchange reactions between toluene vapor and the argon plasma generated by the magnetron caused carbon to be deposited onto the gold sputter target. Thin films deposited under these conditions contained high amounts of undesired carbon (99.36 atomic % carbon as measured by XPS) because carbon rather than gold was sputtered from the magnetron target surface. Carbon impurities of co-deposited films were reduced with increasing oxygen concentration using argon-oxygen mixtures; EQP analysis showed that reactive oxygen species such as O and O⁺ effectively remove unwanted carbon during co-deposition processes. The tribological behavior of films deposited using simultaneous MAPLE and magnetron sputtering was similar to hydrogenated Diamond-like Carbon (DLC) in that a structure transformation (graphitization) occurred in the wear track during cyclic loading resulting in low friction coefficients. In fact, carbon and hydrocarbon fragments from solvent vapor were incorporated into the films leading to formation of hydrogenated DLC-gold composites. This behavior occurs for frozen toluene MAPLE targets regardless of whether they are loaded with CNPs. The exception to this is in a humid air environment where higher friction coefficients are observed for CNP-loaded targets. In these studies, the potential of carbon nanopearls to create environmentally stable solid lubricants has been demonstrated for future aerospace needs. This development could drastically change

current approaches of lubrication for space applications. Additionally a new MAPLE-sputtering process in which solvent-dispersed nano-scale materials are incorporated into metal and ceramic matrices was developed to enable synthesis of novel nanostructured hybrid materials for a variety of applications.

ACKNOWLEDGEMENTS

I would like to acknowledge my Ph.D. advisory committee members for guidance and assistance with preparing my dissertation: Dr. Andrey Voevodin (advisor), Dr. Charles Browning, Dr. Danny Eylon, Dr. Christopher Muratore, Dr. Terry Murray, and Dr. Gerald Shaughnessy. In addition, I would like to thank the following people from AFRL/RX (Materials and Manufacturing Directorate) for technical assistance and discussion: Scott Apt, Nicholas Baine, John Bultman, Michael Check, Steve Fairchild, Carl Hagar, Jianjun Hu, Michael Jespersen, Young Kang, Linda Kasten, Chris Muratore, Jose Nainaparampil, Shanee Pacley, Steve Patton, Art Safriet, Andrey Voevodin, Adam Waite, Willem Wennekes, and Bob Wheeler.

TABLE OF CONTENTS

ABSTRACT.....	iii
ACKNOWLEDGEMENTS.....	vi
LIST OF FIGURES.....	xi
LIST OF TABLES.....	xx
LIST OF ABBREVIATIONS.....	xxi
1 INTRODUCTION.....	1
2 BACKGROUND.....	4
2.1 Overview of carbon structures.....	4
2.1.1 Graphite.....	4
2.1.2 Diamond.....	7
2.1.3 Diamond-like carbon.....	7
2.1.4 Fullerenes.....	11
2.1.5 Carbon onions.....	12
2.1.6 Carbon nanotubes.....	15
2.1.7 Carbon nanopearls.....	17
2.1.8 Summary of properties of carbon forms.....	22
2.2 Tribology of solids.....	25
2.2.1 Historical perspective.....	25
2.2.2 Definitions and mechanisms.....	26

2.2.3 Major laws governing friction and wear of solid lubricants.....	27
2.2.4 Limitations of liquid lubricants.....	30
2.2.5 Materials of interest for aerospace tribological applications.....	31
2.3 Tribology of carbon materials and carbon-based solid lubricants.....	32
2.3.1 Graphite.....	32
2.3.2 Diamond-like carbon.....	32
2.3.3 Fullerenes.....	33
2.3.4 Carbon onions.....	34
2.3.5 Carbon nanotubes.....	40
2.4 Summary of literature analyses and hypothesis for tribology of carbon nanoparticles.....	41
2.5 Potential deposition methods for carbon nanoparticle films.....	42
2.6 MAPLE.....	44
2.7 Electrostatic Quadrupole Plasma (EQP) mass spectroscopy analysis.....	46
2.8 Summary.....	48
3 RESEARCH OBJECTIVES.....	50
4 EXPERIMENTAL METHODS.....	52
4.1 Substrate and test materials.....	52
4.2 Carbon nanoparticle film deposition methods.....	53
4.2.1 Drop cast deposition.....	53
4.2.2 MAPLE.....	54
4.2.2.1 Equipment.....	54
4.2.2.2 MAPLE process study experimental details.....	56
4.2.3 MAPLE with magnetron sputtering experimental details.....	59

4.3 Film formation studies using EQP.....	61
4.4 Experimental details for tribological testing of carbon nanopearl films...	63
4.4.1 Fretting wear experiments.....	63
4.4.2 Ball-on-disk sliding experiments.....	64
4.5 Characterization of carbon nanopearl film morphology, structure, and chemistry.....	65
5 RESULTS AND DISCUSSION.....	69
5.1 Process development and film formation mechanisms for carbon nanopearls.....	69
5.1.1 Drop cast process for carbon nanopearl films.....	69
5.1.2 MAPLE processing studies of carbon nanopearl films.....	70
5.1.2.1 Influence of laser repetition rate.....	71
5.1.2.2 Influence of laser energy.....	73
5.1.2.3 Influence of background pressure.....	75
5.1.2.4 Influence of substrate temperature.....	77
5.1.2.5 Influence of matrix solvent.....	78
5.1.2.6 MAPLE target study.....	81
5.1.2.7 Summary of carbon nanopearl deposition studies using MAPLE.....	83
5.1.3 Studies of hybrid process combining MAPLE deposition of CNPs with magnetron sputtering of gold.....	84
5.1.3.1 Simultaneous MAPLE and magnetron sputtering: argon background.....	85
5.1.3.2 Simultaneous MAPLE and magnetron sputtering: oxygen background.....	87
5.1.3.3 Simultaneous MAPLE and magnetron sputtering: argon and oxygen background.....	89

5.1.3.4 Summary of MAPLE and magnetron sputtering process studies.....	91
5.2 Structure, morphology, and tribological characterization of carbon nanopearl films.....	92
5.2.1 Drop cast carbon nanopearl films.....	92
5.2.2 MAPLE-deposited carbon nanopearl films.....	105
5.2.3 MAPLE and magnetron sputter-deposited gold/CNP films....	109
5.3 Process-property-tribological correlations and mechanisms.....	119
6 CONCLUSIONS.....	122
7 FUTURE STUDIES.....	126
REFERENCE LIST.....	127

LIST OF FIGURES

Figure 2.1.1	Molecular structure of graphite.....	6
Figure 2.1.2	Raman spectra for diamond and graphite.....	6
Figure 2.1.3	Schematic ternary phase diagram illustration of DLC films with respect to their sp^2 and sp^3 bond characters and hydrogen contents.....	8
Figure 2.1.4	D and G vibration modes in carbon.....	10
Figure 2.1.5	Schematic diagram of influences on the Raman spectra of DLC.....	10
Figure 2.1.6:	Molecular configuration of C_{60}	11
Figure 2.1.7	Raman spectrum of C_{60}/C_{70} fullerene material.....	12
Figure 2.1.8	Carbon onions: a) spherical, b) faceted.....	13
Figure 2.1.9	Raman spectrum of carbon onions.....	14

Figure 2.1.10 Raman spectra of SWCNTs with different (n,m) values.....	16
Figure 2.1.11 Raman spectrum of MWCNTs synthesized by pyrolysis of diethyl ether and nickelocene after purification.....	17
Figure 2.1.12 SEM micrograph of carbon spheres synthesized at 1100°C.....	18
Figure 2.1.13 Nucleation of a pentagon (a), which grows to a spiral shell carbon particle (d).....	18
Figure 2.1.14 EELS spectra of (A) nanospheres, (B) non-graphitic carbon, (C) graphite.....	19
Figure 2.1.15 Carbon spheres produced by CVD using Ar carrier gas, flow rate 80 ml/min.....	20
Figure 2.1.16 UV-laser Raman spectrum of carbon spheres.....	20
Figure 2.1.17 Foam-like structure of the carbon nanopearls.....	21
Figure 2.1.18 HRTEM image of a carbon nanopearl.....	21
Figure 2.1.19 High magnification image at the surface of a carbon nanopearl.....	22
Figure 2.1.20 Raman spectrum of a carbon nanopearl.....	22
Figure 2.2.1 Picture found on a wall of a grotto in El-Bersheh showing Egyptians transporting a colossus ca 1800 BC.....	26

Figure 2.2.2 Relationship between actual contact area, shear stress, and friction coefficient for different contact regimes.....	29
Figure 2.3.1 Friction coefficient variations for carbon onions, graphite, diamond clusters, and C ₆₀ /C ₇₀ on Si (1 0 0) as a function of sliding distance in a) air at 55% relative humidity; b) vacuum at 1.3x10 ⁻³ Pa.....	36
Figure 2.3.2 Wear scars on steel balls after friction testing in vacuum using: a) no lubricant; b) graphite; c) C ₆₀ /C ₇₀ ; d) carbon onions synthesized from diamond clusters; e) carbon onions synthesized from diamond particles.....	37
Figure 2.3.3 Friction coefficients as a function of surface roughness for (100) Si discs (a) in air and (b) in vacuum.....	38
Figure 2.3.4 Schematic illustration of tribological behavior of carbon onions on sliding surfaces.....	39
Figure 2.4.1 Hypothetical contact mechanisms for carbon nanopearls: a) Ball bearing effect in which CNPs remain intact and roll past opposing surfaces and each other; b) Nanopearls are flattened and smeared and the graphene flakes are distributed between the opposing contact surfaces.....	42
Figure 2.6.1 Schematic illustrations of a) pulsed laser deposition and b) MAPLE	44
Figure 2.7.1 Schematic illustration of EQP analyzer.....	47
Figure 4.2.1 MAPLE system used to deposit carbon nanopearl thin films.....	55
Figure 4.2.2 EQP analyzer.....	55

Figure 4.2.3	Glove box used for preparation of frozen MAPLE targets. Arrow indicates sealable chamber for transporting frozen targets from the glovebox to the deposition chamber.....	56
Figure 4.2.4	Optical image of CNPs deposited onto a silicon wafer by MAPLE after image processing using MATLAB program.....	58
Figure 4.4.1	Contact geometry of ellipsoid sample used in fretting wear test.....	64
Figure 4.4.2	Tribometer.....	65
Figure 4.5.1	SEM/EDS system.....	66
Figure 4.5.2	Raman microscope.....	67
Figure 4.5.3	X-Ray diffractometer system.....	67
Figure 4.5.4	XPS system.....	68
Figure 5.1.1	Methanol drop-cast CNPs on silicon.....	70
Figure 5.1.2	MAPLE samples synthesized at several laser repetition rates. Area fraction covered with carbon nanopearls listed in parentheses.....	72
Figure 5.1.3	Schematic illustration of the effect of laser repetition rate on frozen MAPLE targets.....	73

Figure 5.1.4 MAPLE samples synthesized at several laser energies. Area fraction covered with carbon nanopearls listed in parentheses.....74

Figure 5.1.5 MAPLE samples synthesized at several background pressures. Pressure for sample deposited in vacuum was unregulated. Area fraction covered with carbon nanopearls listed in parentheses.....76

Figure 5.1.6 MAPLE samples synthesized at several background pressures and temperatures. Area fraction covered with carbon nanopearls listed in parentheses...78

Figure 5.1.7 MAPLE samples synthesized using various matrix solvents. Area fraction covered with carbon nanopearls listed in parentheses. Vapor pressure (P), Melting Temperature (T), and Absorbance at 248 nm (A) for each matrix solvent are listed.....80

Figure 5.1.8 Frozen MAPLE targets after 1.5 hours of laser ablation: a) 0.08 wt. % carbon nanopearls in toluene, b) toluene. Diameter of target reservoir = 25.4 mm...82

Figure 5.1.9 Counts vs. atomic mass per unit charge for: a) magnetron sputtering with gold target (30W output power in argon at 20mTorr @ 100sccm) and b) magnetron sputtering with gold target operating (30W output power in argon at 20mTorr @ 100sccm) and simultaneous MAPLE operation (target: 0.08% carbon nanopearls in toluene, 700 mJ, 1 Hz).....86

Figure 5.1.10 Mechanisms on a gold target surface in argon plasma during simultaneous MAPLE and magnetron sputtering: 1) Sputtering of Au atoms in Ar plasma; 2) Toluene/argon ion exchange; 3) Deposition of carbon onto gold target surface; 4) Sputtering of carbon from gold target surface.....87

Figure 5.1.11 Mass spectra of neutral species in oxygen background (20 mTorr, 100 sccm) during MAPLE (target: 0.08% carbon nanopearls in toluene, 700 mJ, 1 Hz) with and without the magnetron operating (Au target, 60W power).....88

Figure 5.1.12 Mechanisms in oxygen plasma during simultaneous MAPLE and magnetron sputtering: 1) Sputtering of Au atoms in oxygen plasma; 2) Example reaction of toluene vapor with oxygen plasma; 3) Oxygen plasma reaction with carbon deposit on gold target surface.....89

Figure 5.1.13 Species concentration vs. oxygen flow rate (where oxygen flow rate + argon flow rate = 100).....	90
Figure 5.1.14 Toluene ion concentration (90 to 95 amu) vs. scan time for a range of oxygen to argon ratios.....	91
Figure 5.1.15 Integrated toluene ion area (90 to 95 amu) vs. oxygen flow rate at 8 minutes of simultaneous MAPLE and magnetron sputtering.....	91
Figure 5.2.1 Raman spectrum of methanol drop cast carbon nanopearls on silicon	93
Figure 5.2.2 Friction coefficients in ball-on-disk tribometer tests on silicon wafers with methanol-dispersed nanopearl material and graphite powder in 40% and 0% relative humidity.....	94
Figure 5.2.3 SEM micrographs of CNP coated surface of silicon wafer in the middle of a wear track after ball-on-disk tribometer test (40% relative humidity)....	95
Figure 5.2.4 EDS area composition maps (carbon and oxygen) of the wear track on CNP-coated surface of silicon wafer after ball-on-disk tribometer test (40% relative humidity). Dotted lines indicate wear scar area; arrow indicates sliding direction (Note: scale marker size approximate).....	96
Figure 5.2.5 SEM micrographs of surface of 440C steel ball after pin-on-disk tribometer test in contact with silicon wafer containing carbon nanopearls (40% relative humidity).....	97
Figure 5.2.6 SEM micrographs of nanopearl-coated surface of silicon wafer after ball-on-disk tribometer test in contact with 440C steel ball bearing (0% relative humidity).....	98
Figure 5.2.7 EDS area composition maps (carbon and oxygen) of the wear track on CNP-coated surface of silicon wafer after ball-on-disk tribometer test (0% relative humidity). Oval indicates wear scar area; arrow indicates sliding direction (Note: scale marker size approximate).....	98

Figure 5.2.8 SEM micrographs of surface of 440C steel ball after ball-on-disk tribometer test in contact with silicon wafer containing carbon nanopearls (0% relative humidity). Arrow indicates sliding direction; oval indicates contact area...99

Figure 5.2.9 Friction coefficient vs. number of cycles for M50 steel ellipsoid on M50 flat fretting wear test.....101

Figure 5.2.10 EDS compositional map (oxygen and carbon) of surface of M50 ellipsoid sample after fretting wear test in humid air environment. Oval indicates contact area; arrow indicates sliding direction.....102

Figure 5.2.11 EDS compositional map (oxygen and carbon) of surface of M50 ellipsoid sample after fretting wear test in dry air environment. Oval indicates contact area; arrow indicates sliding direction.....103

Figure 5.2.12 Optical micrograph and Raman spectrum of MAPLE film (target: 0.08% carbon nanopearls in methanol, 500 mJ, 3 Hz, 7 minute deposition time, 100°C substrate temperature) deposited onto a silicon wafer. Oval indicates region from which the Raman spectrum was collected. Methanol drop cast Raman spectrum shown for comparison.....105

Figure 5.2.13 Friction coefficient of MAPLE film (target: 0.08% carbon nanopearls in methanol, 500 mJ, 3 Hz, 7 minute deposition time, 100°C substrate temperature) deposited onto a silicon wafer during ball-on-disk tribometer testing in dry nitrogen (0% relative humidity). Inset: optical micrographs and Raman spectra of wear tracks. Ovals indicate regions from which the Raman spectra were collected.....107

Figure 5.2.14 Friction coefficient of MAPLE film (target: 0.08% carbon nanopearls in methanol, 500 mJ, 3 Hz, 7 minute deposition time, 100°C substrate temperature) deposited onto a silicon wafer during ball-on-disk tribometer testing in humid air (40% relative humidity). Inset: optical micrograph and Raman spectrum of wear track. Oval indicates region from which the Raman spectrum was collected.....108

Figure 5.2.15 XPS spectra and cross sectional SEM micrographs of thin films deposited using simultaneous MAPLE (target: 0.08% carbon nanopearls in toluene, 700 mJ, 1 Hz) and magnetron sputtering (Au target, 30W power): a) in 20% oxygen and 80% argon, and b) 90% oxygen and 10% argon as background gases.....110

Figure 5.2.16 SEM micrographs of thin films deposited using simultaneous MAPLE and magnetron sputtering (Au target, 30W power): a) AISI 440C substrate, MAPLE target 0.08% CNPs in toluene, 700 mJ, 1 Hz, 15 mTorr, background gas 75 sccm oxygen/25 sccm argon, 20°C substrate temperature; b) AISI 440C substrate, MAPLE target toluene, 700 mJ, 1 Hz, 15 mTorr, background gas 75 sccm oxygen/25 sccm argon, 20°C substrate temperature. Sample c) deposited using sputtering only (Au target, 30W power, 20 mTorr argon @ 100 sccm, 100°C substrate temperature) no MAPLE.....112

Figure 5.2.17 Sample ID# MM-18: Optical micrograph and Raman spectrum of film deposited using simultaneous MAPLE (target: 0.08% carbon nanopearls in toluene, 700 mJ, 1 Hz, 45 minute deposition time, 20°C substrate temperature, 150V substrate bias, 75 sccm oxygen+25 sccm argon background gases) and magnetron sputtering (Au target, 30W). Oval indicates region from which the Raman spectrum was collected.....112

Figure 5.2.18 Sample ID# MM-19: Optical micrograph and Raman spectrum of film deposited using simultaneous MAPLE (target: toluene, 700 mJ, 1 Hz, 45 minute deposition time, 20°C substrate temperature, 150V substrate bias, 75 sccm oxygen+25 sccm argon background gases) and magnetron sputtering (Au target, 30W). Oval indicates region from which the Raman spectrum was collected.....113

Figure 5.2.19 Friction coefficients during ball-on-disk tribometer testing under dry nitrogen atmosphere (0% relative humidity) of films deposited using toluene MAPLE targets with and without carbon nanopearls. Inset: optical micrographs and Raman spectra of wear tracks. Ovals indicate regions from which the Raman spectra were collected.....114

Figure 5.2.20: Friction coefficients during ball-on-disk tribometer testing under humid air atmosphere (40% relative humidity) of films deposited using toluene MAPLE targets with and without carbon nanopearls. Inset: optical micrographs and Raman spectra of wear tracks. Ovals indicate regions from which the Raman spectra were collected.....116

Figure 5.2.21 Schematic drawing showing morphological changes under friction loading for simultaneous MAPLE and sputter-deposited film with CNP in a gold matrix.....116

Figure 5.2.22 Cross-sectional SEM micrograph of sequentially-deposited CNP-gold film (sample ID# MM-23 in Table 4.2.2). Arrows indicate sheets of gold that completely delaminated from the gold/chromium interlayer.....118

Figure 5.3.1 Drop cast film of CNP on M50 steel after fretting wear test. Arrows indicate contact region where CNPs are flattened and smeared.....120

LIST OF TABLES

Table 2.1.1	Hardness and friction coefficients of DLC films.....	9
Table 2.1.2	Summary of typical physical properties of carbon in its various forms	24
Table 4.2.1	List of investigated MAPLE process settings.....	57
Table 4.2.2	List of thin films deposited using MAPLE and magnetron sputtering	60
Table 4.3.1	List of experimental conditions within the MAPLE deposition chamber evaluated using EQP.....	62

LIST OF ABBREVIATIONS

a-C	amorphous diamond-like carbon
a-C:H	hydrogenated amorphous diamond-like carbon
AFM	atomic force microscopy
CNP	carbon nanopearl
CNT	carbon nanotube
DC	direct current
DLC	diamond-like carbon
DMF	dimethyl formadine
DMSO	dimethyl sulfoxide
EDS	energy dispersive spectrometer
EELS	electron energy loss spectroscopy
EQP	electrostatic quadrupole plasma
ESA	energy sector analyzer
ESR	electron spin resonance
Et-Ace	ethyl acetate
FFM	frictional force microscopy
HRTEM	high resolution transmission electron microscopy
MAPLE	matrix assisted pulsed laser evaporation
MEMS	microelectromechanical system

MtOH	methanol
MWCNT	multi-walled carbon nanotube
PAO	polyalphaolefin
PE-CVD	plasma enhanced chemical vapor deposition
PLD	pulsed laser deposition
PTFE	polytetrafluoroethylene
PVD	physical vapor deposition
QMS	quadrupole mass spectrometer
RBM	radial breathing mode
RF	radio frequency
RH	relative humidity
SEM	scanning electron microscopy
SEM	secondary electron analyzer
SWCNT	single walled carbon nanotube
ta-C	tetragonal amorphous diamond-like carbon
ta-C:H	hydrogenated tetragonal amorphous diamond-like carbon
TEM	transmission electron microscopy
UHV	ultra high vacuum
UV	ultraviolet
UV-vis	ultraviolet-visible spectrometer
XPS	X-Ray photoelectron spectroscopy
XRD	X-Ray diffraction

1. INTRODUCTION

Future aerospace systems face tough challenges to tribological surfaces and interfaces to enable reliable performance in extreme environments, including dramatic reduction in friction energy losses, operation life extension, and system miniaturization.

Currently, due to large friction losses in space and aircraft components, the US Air Force needs large power driving engines, which leads to more energy waste and system weight increases, and limits aerospace system capabilities for air and space lift. Loss of tolerances and off-set of vibrations lead to losing targeting capabilities, which is a failure for many air and space mission. Air Force systems have a variety of movable mechanisms, which suffer degraded performance and fail because of tribological problems. In some instances, new design concepts cannot be realized because of friction and wear issues. All of these problems are especially detrimental for Air Force aerospace systems capabilities which have to operate across multiple extreme environments during space and air missions. The successful development of new surface engineering technologies, such as coatings, monolayers, and boundary lubrication additives are strongly dependent on understanding basic fundamental mechanisms in tribological contact surfaces and interfaces. In addition, these challenges require investigation of novel materials such as carbon nanopearls and development of processes to utilize these materials. This research is being conducted in order to establish a fundamental understanding of processing and tribological

contact mechanisms of carbon nanopearls. It correlates structure, chemistry, and morphology of carbon nanopearls to their friction and wear behavior and highlights major mechanisms of CNP performance in sliding and fretting wear contacts on the substrates and environments relevant to potential aerospace applications. Carbon nanopearls, closed spherical structures ~150 nm in diameter consisting of concentric shells of amorphous material containing 2-6 nm sized graphitic flakes synthesized by catalyzed chemical vapor deposition (CVD) [2], were selected for these studies because their size, spherical shape, and graphitic structure may make them ideal lubricants in both humid air and vacuum environments. In order to effectively study tribological properties of CNPs it is necessary to develop a method to anchor the CNPs into a film so that their properties can be studied as wear of the film is taking place. An advantageous technique identified for deposition of CNPs is matrix assisted pulsed laser evaporation (MAPLE) because deposition can be accomplished with little or no damage to the transported material [3,4,5,6]. The process studies were performed and methodology was developed to optimize MAPLE for depositing carbon nanopearls while investigating the influence of experimental parameters on the morphology of the deposited films. The optimum MAPLE parameters were established to synthesize a nanostructured hybrid film by combining MAPLE with magnetron sputtering. Electrostatic quadrupole plasma (EQP) mass spectroscopy was used to study the combined MAPLE and magnetron sputtering processes to gain insights into the nature of the deposition processes and the relationship between neutral and ionic species and substrate film morphology and composition. Tribological studies of thin films deposited using three processes (drop casting,

MAPLE, and MAPLE combined with magnetron sputtering) were performed, and the structure, chemistry, and morphology of carbon nanopearls is discussed in correlation to their tribological behavior. These results lead to conclusions on both optimal routes of CNP processing to create CNP thin films and on fundamental tribological mechanisms of CNPs in sliding and fretting contacts. Finally, directions for future research are outlined based on the detailed scientific studies of this work.

Major research results were published in the following archived refereed journals:

C.N. Hunter, M.H. Check, A.A Voevodin, and C.H. Hager, Tribological properties of carbon nanopearls synthesized by nickel-catalyzed chemical vapor deposition, Tribology Letters 30, 169-176 (2008).

C.N. Hunter, M.H. Check, J.E. Bultman, A.A. Voevodin, Development of Matrix Assisted Pulsed Laser Evaporation (MAPLE) for deposition of disperse films of carbon nanoparticles, Surface & Coatings Technology 203, 300-306 (2008).

2. BACKGROUND

2.1 Overview of carbon structures

Carbon is the 4th most abundant element in the solar system after hydrogen, helium, and oxygen, and is mostly found in the form of hydrocarbons and other compounds, with a concentration in the earth's crust of 180 ppm. Diamond and natural graphite are the only carbon minerals found in nature; all other carbon products are synthetic materials derived from carbonaceous precursors. Natural carbon-containing compounds are used in many industrial processes to produce a wide variety of carbon materials including coals, carbon black, molded and pyrolytic graphite, carbon fibers, diamond-like carbon coatings, carbon nanotubes and fullerenes, carbon foam, hydrocarbon complexes such as petroleum, tar and asphalt, hydrocarbon gases such as methane, and synthetic diamond [7].

2.1.1 Graphite

Graphite in natural mineral form is commonly classified into three general types: flake, found in metamorphosed silica-rich quartzite, gneisses, and marbles; crystalline (vein), found in transverse, igneous, or metamorphic rocks and formed by the transformation of oil precursors; and amorphous graphite, which results from

metamorphosis of coal exposed to high pressure. The types of graphite vary in physical properties, appearance, chemical composition, and impurities. These differences result from the type of precursor material and the natural process by which the graphite was formed. Natural graphites are used for a variety of industrial applications, including fabrication of refractory crucibles, lubricating oils and greases, dry-film lubricants, batteries, conductive coatings, electrical brushes, carbon additives, paints, and pencil manufacturing. However, a large majority of graphite and carbon products are synthetic. Major categories of synthetic graphite and carbon products are as follows: molded graphite and carbon; vitreous (glassy) carbon; pyrolytic graphite and carbon; carbon fibers; carbon composites and carbon-carbon; carbon and graphite powders and particles; and carbon nanoparticles (e.g. nanotubes and fullerenes) [7].

Graphite is a planar molecule with carbon atoms arranged in a hexagonal structure within each layer. Each carbon atom is joined to three adjacent carbon atoms by covalent (σ) bonds with sp^2 orbital hybridization; the fourth unhybridized electron creates a van der Waals (π) bond, which is delocalized across the hexagonal atomic sheet of carbon. Adjacent planes are bonded together by Van der Waals type forces, which are much weaker than the σ bonds within the planes (Figure 2.1.1). The large difference between intra-planar and inter-planar binding energies within graphite leads to a high degree of anisotropy of many properties. For example, the thermal conductivity of pyrolytic graphite is controlled by lattice vibrations and is 390 W/m-

K within plane and 2 W/m-K normal to the plane. Planar graphite is characterized by a Raman spectrum with a sharp peak at 1570 cm^{-1} (Figure 2.1.2).

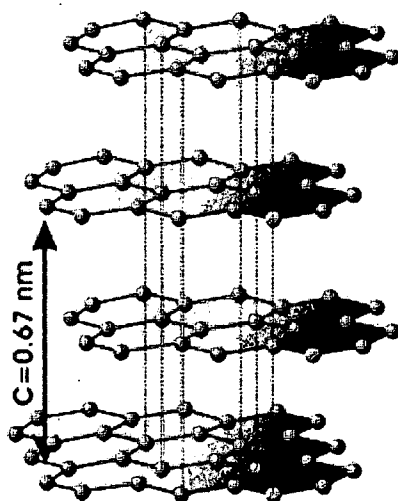


Figure 2.1.1: Molecular structure of graphite [8]

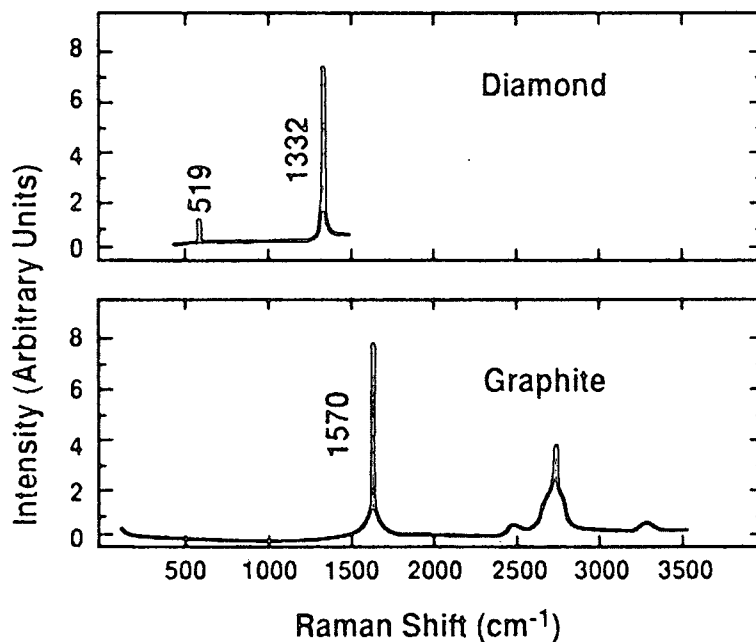


Figure 2.1.2: Raman spectra for diamond and graphite [7]

2.1.2 Diamond

Diamond is a naturally occurring mineral with several crystalline polytypes, of which cubic diamond is the most common and stable. Diamond has a number of outstanding properties, including extremely high index of refraction, thermal conductivity, hardness, strength and rigidity. It also has excellent optical transmission properties, is an excellent semiconductor material, and has an excellent natural lubricity in air. While these properties make diamond a desirable material for many application areas, natural diamonds are scarce and very expensive. Fortunately, synthetic diamond can be produced in industrial scale quantities using methods such as high pressure forming, explosive detonation, and chemical vapor deposition (CVD).

In contrast to graphite, structure and properties of diamond are essentially isotropic due to the sp^3 hybridization of the carbon atoms. Each carbon atom is bonded to four other carbon atoms with strong covalent bonds. Diamond is characterized by a Raman spectrum with a sharp narrow peak at 1332 cm^{-1} (Figure 2.1.2) [7].

2.1.3 Diamond-like carbon

Diamond-like carbon (DLC) refers to metastable carbon usually produced as a thin film that can be highly tailored by adjusting processing parameters to affect structure (ratio of sp^2 to sp^3 bonds) and composition (hydrogen concentration). The structure is

primarily amorphous with a mixture of small sp^3 and sp^2 -bonded domains forming a disordered network. The larger the percentage of sp^3 bonding in the network, the more the properties of the material approach those of diamond. In general, DLC can be divided into amorphous (a-C) and hydrogenated amorphous (a-C:H) DLC, which have a predominance of sp^2 bonding in crystallites, and tetragonal amorphous (ta-C) and hydrogenated tetragonal amorphous (ta-C:H) DLC, which have a predominance of sp^3 bonds. Hydrogen in DLC films acts as a terminator of carbon-carbon bonds and has an effect on a number of properties, including optical bandgap, electrical resistivity, and mechanical characteristics. In addition, hydrogen stabilizes the random covalent network and prevents its collapse into a graphitic phase [9]. A ternary phase diagram summarizing classifications of carbon films with respect to their hydrogen concentration and sp^2 and sp^3 bond characters is shown in Figure 2.1.3.

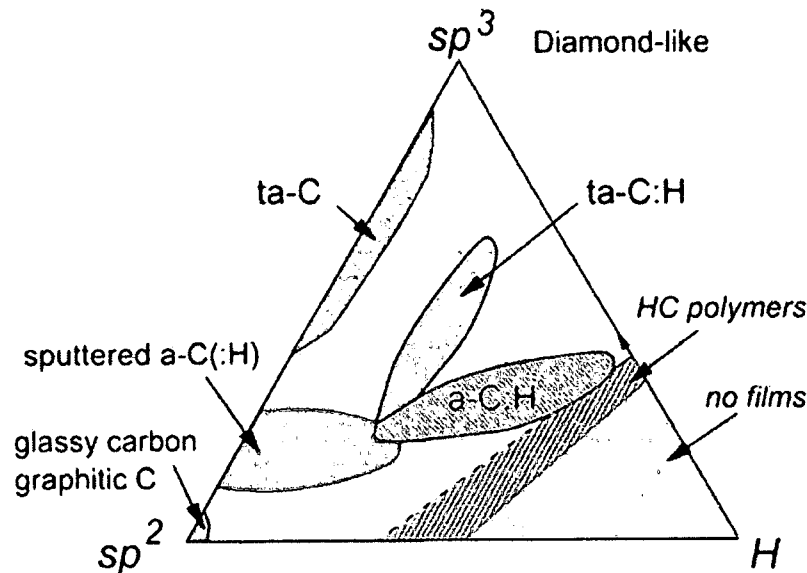


Figure 2.1.3: Schematic ternary phase diagram illustration of DLC films with respect to their sp^2 and sp^3 bond characters and hydrogen contents [10]

DLC films are deposited using two main classifications of deposition techniques: physical vapor deposition (PVD) (i.e. pulsed laser deposition, cathodic arc deposition, ion beam sputtering, magnetron sputtering, ion assisted deposition), in which the carbon source for the film is a solid carbon target; and plasma enhanced chemical vapor deposition (PE-CVD), in which the carbon source for the film is hydrocarbon gases. Depending on characteristics of the film—hydrogen concentration, carbon hybridization ratio, and nature of bonds—a wide range of mechanical properties are exhibited [9]. Hardness and friction coefficient data for several DLC films are shown in Table 2.1.1.

Synthesis method	DLC Type	Hardness (GPa)	Friction coefficient (air)	Friction coefficient (vacuum)
PLD (graphite target)	a-C	55-70	0.06-0.12	0.06-0.11
PLD (polycarbonate target)	a-C:H	12-20	0.05-0.19	0.09-0.26
Plasma assisted CVD	a-C:H	3.5-13.5	0.12-0.18	<0.01-0.55*

Table 2.1.1: Hardness and friction coefficients of DLC films [11,12]

DLC films are characterized by Raman spectra typical of disordered graphite, containing prominent D and G bands located at around 1350 cm^{-1} and 1590 cm^{-1} respectively. The G band arises from in-plane bond stretching motion of pairs of carbon sp^2 -bonded atoms, while the D band involves breathing modes of aromatic rings and only becomes active in disordered carbon [12]. Carbon atom motions leading to D and G vibration modes are shown schematically in Figure 2.1.4. Raman

spectra characteristics of DLC films depend fundamentally on the configuration of sp^2 sites within sp^2 -bonded clusters, bond disorder, the presence of sp^2 rings and chains, and the sp^2/sp^3 ratio [13]. The influence of these factors on the Raman spectra is depicted in Figure 2.1.5.

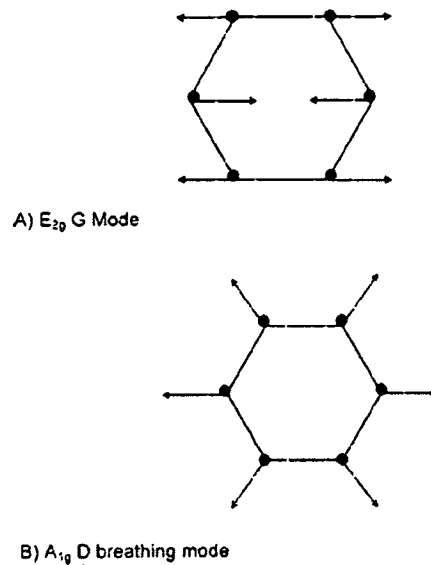


Figure 2.1.4: D and G vibration modes in carbon [13]

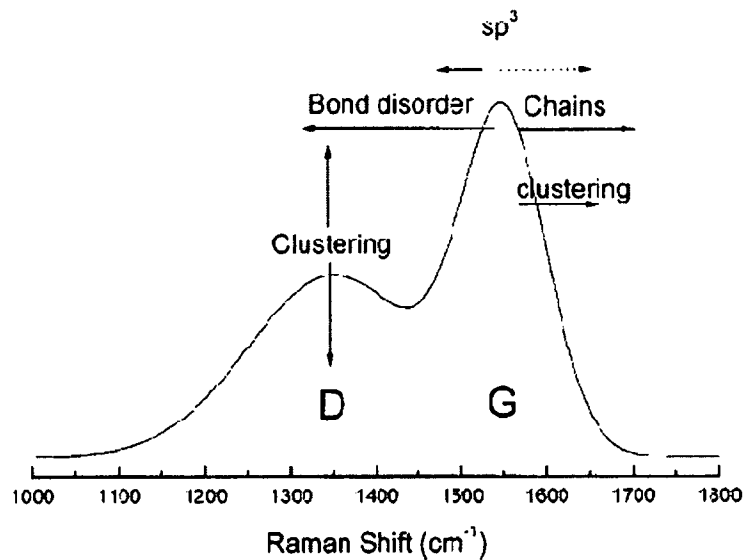


Figure 2.1.5: Schematic diagram of influences on the Raman spectra of DLC [13]

2.1.4 Fullerenes

Buckminsterfullerene (C_{60}) is a closed sp^2 -hybridized molecule consisting of 60 carbon atoms arranged in a soccer ball configuration (Figure 2.1.6) which was discovered in 1985 by Kroto et al. during experiments on laser vaporization of graphite in order to understand mechanisms of long-chain carbon molecules in interstellar space [14]. C_{60} and other closed graphitic structures with similar molecular configurations (e.g. C_{70} , C_{84}) are known as fullerenes. A large volume of research has been conducted since bulk production of C_{60} was achieved a few years after its initial discovery [15]. Though molecular properties of C_{60} (e.g. high modulus, electrical and thermal conductivity, etc.) provide the potential for applications in many areas, this potential has yet to be fully realized. At the present, a few active applications exist including fullerene complex superconducting materials, photovoltaics, and cosmetics, and fullerene-like materials (e.g. CNx) have applications as field emitters and in tribological coatings. C_{60} is characterized by a Raman spectrum with an identifying peak at around 1467 cm^{-1} (Figure 2.1.7).

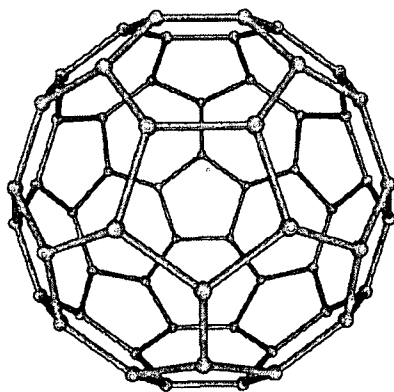


Figure 2.1.6: Molecular configuration of C_{60}

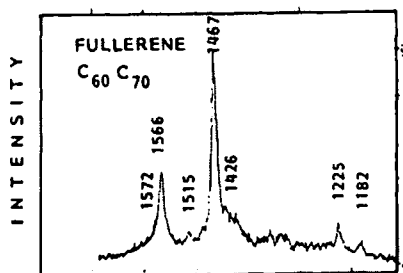


Figure 2.1.7: Raman spectrum of C_{60}/C_{70} fullerene material [16]

2.1.5 Carbon onions

Carbon onions are closed graphitic networks that consist of concentric spherical or faceted fullerene shells (Figure 2.1.8). Fully formed onions have few obvious defects, and have a central shell of approximately 0.7-1 nm in diameter, i.e. close to the diameter of C_{60} [17]. Ugarte discovered carbon onions while studied irradiation of carbon nanoparticles with gold and lanthanum oxide encapsulates in a TEM. During electron irradiation, nanoparticles undergo a transformation from faceted hollow or encapsulating fullerene shells to nearly perfect concentric spheres, down to a 0.7-1 nm central shell [18,19]. Size variations ranging from two-shell configurations (diameter \sim 1.4 nm) up to onions with hundreds of shells and diameters in the micron range have been observed [20]. Depending on the method of production and processing parameters, variations in shape and composition can occur. Faceted and/or hollow shaped carbon onions have been observed, as well as those containing encapsulates such as diamond or metal crystal.

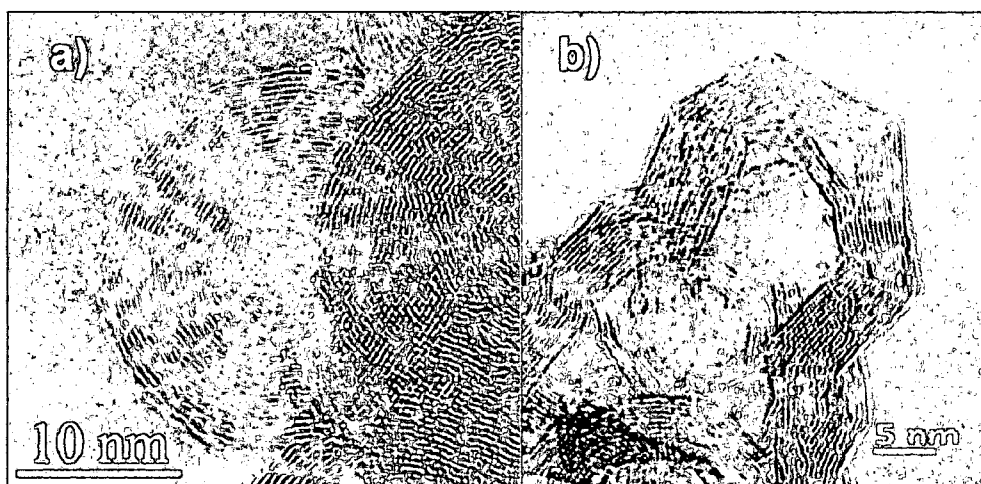


Figure 2.1.8: Carbon onions: a) spherical, b) faceted [21,22]

Several other production methods for carbon onions exist: annealing soot or diamond nanoparticles in vacuum [23,1], carbon ion implantation into copper or silver at high temperatures [24], RF plasma CVD [25], arc discharge of graphite under water [26,21,27], and laser ablation methods [28]. Recently, milligram quantities of carbon onions have been produced by Rettenbacher, et al. using arcing of graphite under water [27] and Hirata, et. al. using heat treatment of diamond clusters or particles [1]. Several applications for carbon onions have been proposed, including optical limiting [29], catalysis [30], gas storage [21], photovoltaic applications, and tribology [22,1,31,32].

Tomita, et. al. studied electronic properties of carbon onions using high-resolution TEM (HRTEM) and Electron Spin Resonance (ESR) and concluded that π electrons (those associated with a van der Waals bond) in carbon onions are localized in small domains of the graphitic sp^2 sheets and do not act as conduction electrons [33]. The

ESR spectra showed only a narrow signal corresponding to dangling bond spins associated with structural defects. Thermal stability of carbon onions has not been studied extensively, although Street, et al. observed that faceted carbon nanoparticles are stable in air up to 750°C [22]. Also, it has been observed that heat treatment of carbon onions above ~1900°C results in transformation from spherical to faceted structure [33]. A survey of recent literature revealed an absence of studies of mechanical properties of carbon onions, though they are presumed to possess extremely high strength and modulus.

Carbon onions contain Raman peaks at 1100, 861, 700, 450, and 250 cm^{-1} that are not present in the Raman spectrum of graphite (Figure 2.1.9). The curvature of the graphene planes in the shells is presumed to be responsible for the appearance of the additional Raman peaks [34].

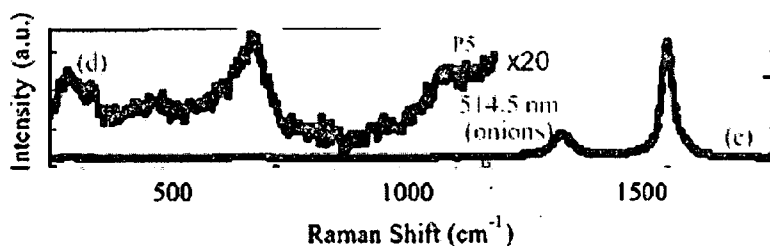


Figure 2.1.9: Raman spectrum of carbon onions [34]

2.1.6 Carbon nanotubes

Carbon nanotubes (CNTs) are graphene cylinders consisting entirely of sp^2 C-C bonds usually closed at both ends by fullerene hemispheres. Discovery of CNT's was made in 1991 by Iijima while studying carbon soot produced by arc evaporation. Since then, several bulk synthesis methods have been developed and include arc discharge, laser ablation, and CVD. The simplest CNT structure is a single wall CNTs (SWCNT), which consists of a single sheet of carbon atoms arranged in hexagon configuration (known as graphene) rolled into a cylinder one atom thick, which have a typical diameter of ≈ 1 nm. Multi wall CNTs (MWCNT) are nested coaxial SWCNTs arranged in a Russian doll configuration and can have diameters up to several thousand times larger than SWCNTs. The structure of a SWCNT is completely described, except for its length, by the chiral vector. The direction of the chiral vector is perpendicular to the direction of the nanotube axis, and the magnitude of the chiral vector is equal to the circumference of the nanotube [35].

CNTs exhibit extraordinary strength, unique electrical properties, and are efficient conductors of heat. Young's modulus values (≈ 1 TPa) of CNTs are larger than any other known material. CNTs are also extremely resilient; irreversible yielding occurs only at extreme temperatures and loads. Electronic properties of CNTs are extremely sensitive to the diameter, helicity, and defect structure of the tubes. SWCNTs can behave as metals or small to large band gap semiconductors depending on their chirality [36]. Properties of carbon nanotubes are also highly anisotropic. Because of

their extraordinary properties, nanotubes are being explored and utilized in many application areas, including: conductive and high-strength composites; energy storage and energy conversion devices; sensors; field emission displays and radiation sources; hydrogen storage media; nanometer-sized semiconductor devices, probes, and interconnects; and tribology.

Raman spectra of SWCNTs are characterized by G band features at around 1582 cm^{-1} and radial breathing mode (RBM) bands at $100\text{-}500\text{ cm}^{-1}$ (Figure 2.1.10). RBM is a bond-stretching out-of-plane phonon mode for which all the carbon atoms move coherently in the radial direction [37]. In MWCNTs, the G band splitting is less intense and smeared out due to the effect of diameter distribution and non-uniformity of nanotubes present in samples used for experiments (Figure 2.1.11) [37].

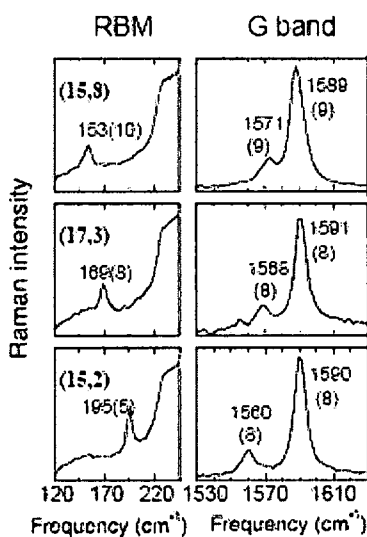


Figure 2.1.10: Raman spectra of SWCNTs with different (n,m) values [37]

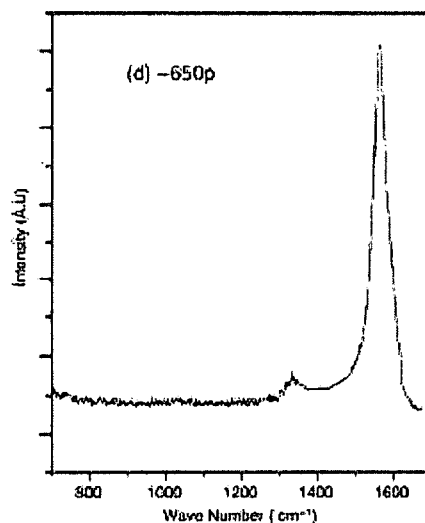


Figure 2.1.11: Raman spectrum of MWCNTs synthesized by pyrolysis of diethyl ether and nickelocene after purification [38]

2.1.7 Carbon nanopearls

Carbon nanopearls (CNPs), also known as carbon spheres or carbon nanospheres, are composed of amorphous carbon that contains concentrically-oriented nano-sized graphitic flakes. A number of researchers have synthesized and characterized these materials. This section summarizes results of CNP studies in the literature.

Wang and Kang synthesized carbon spheres in 1996 using an oxide catalytic CVD process. The spheres had an average diameter of 210 nm and were composed of flat graphitic flakes in the size range 1-30 nm (Figure 2.1.12). The authors suggested a model of carbon sphere formation and growth, with nucleation from a pentagon carbon ring followed by a spiral shell growth (Figure 2.1.13). Structural characterization (Raman, XRD, etc.) was not performed in this study [39].

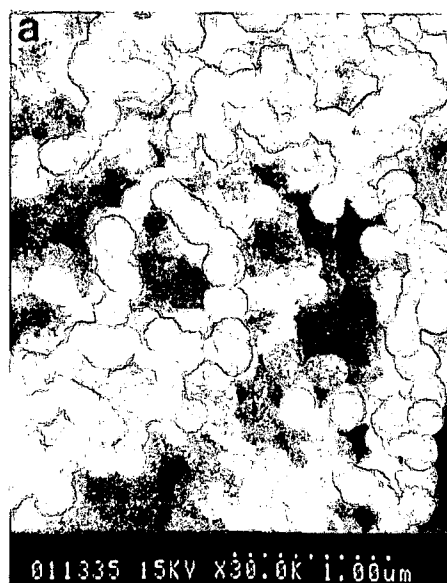


Figure 2.1.12: SEM micrograph of carbon spheres synthesized at 1100°C [39].

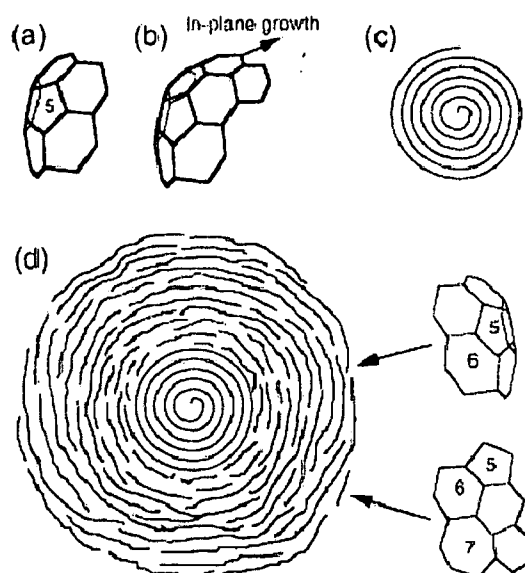


Figure 2.1.13: Nucleation of a pentagon (a), which grows to a spiral shell carbon particle (d) [39].

Serp, et al. synthesized milligram quantities of nanospheres by CVD at 1100°C using a mixture of $\text{CH}_4\text{-H}_2$ in the presence of a metallic iron catalyst. The particles were well dispersed and had diameters ranging between 100 and 300 nm. EELS spectra of the nanospheres exhibited a well-defined graphitic character with a π^* peak at 285 eV

and σ^* structures above 290 eV (Figure 2.1.14). The authors described the carbon spheres as similar to those produced by Wang and Kang [40].

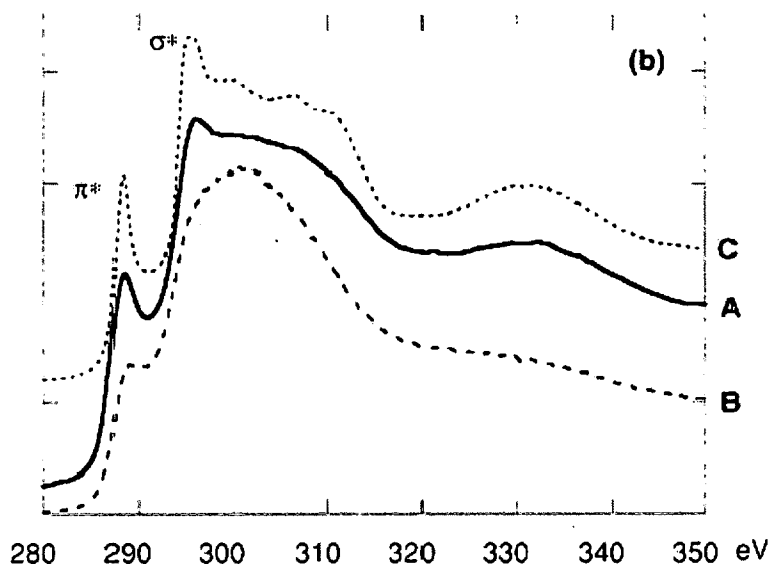


Figure 2.1.14: EELS spectra of (A) nanospheres, (B) non-graphitic carbon, (C) graphite [40].

Qian, et al. synthesized carbon spheres 60 nm - 1 μ m in diameter by a non-catalytic CVD method using toluene (Figure 2.1.15). The particle size was controlled by changing the composition of the carrier gas and the gas flow rate. UV-laser Raman spectroscopy (Figure 2.1.16) and XRD performed on the carbon spheres indicated a mixed graphitic and amorphous structure, ($I_D/I_G \sim 0.84$).

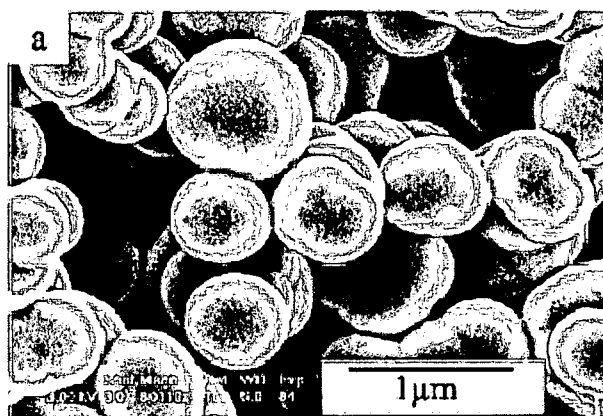


Figure 2.1.15: Carbon spheres produced by CVD using Ar carrier gas, flow rate 80 ml/min [41].

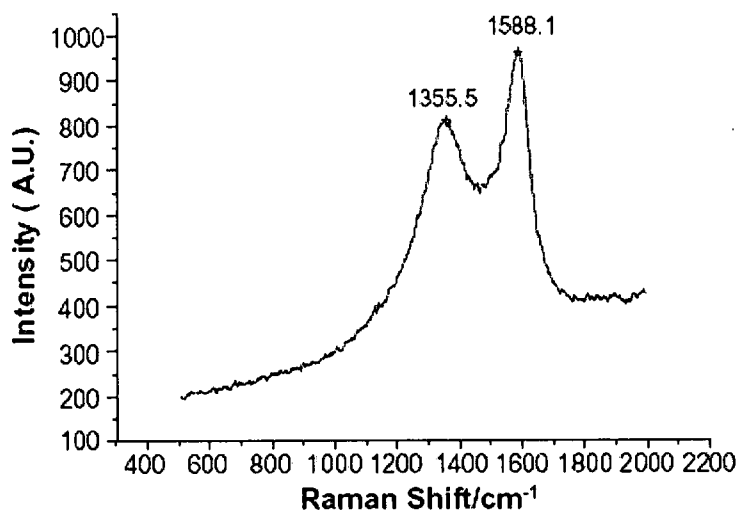


Figure 2.1.16: UV-laser Raman spectrum of carbon spheres [41].

Levesque, et al. synthesized carbon nanopearls by CVD using nickel nanocluster-catalyzed dissociation of acetylene at 700 °C. The synthesized material had a macroscopic foam-like appearance (Figure 2.1.17). The nanopearls were spherical with uniform diameter ≈ 150 nm (Figure 2.1.18). High magnification images indicated that the spheres were composed of flakes approximately 2-6 nm in size and organized in concentric layers (Figure 2.1.19). Raman spectroscopy indicated that the nanopearls were composed of graphitic and amorphous structure (Figure 2.1.20).

Raman and XRD analysis indicated that the average size of the nanocrystalline regions in the nanopearls was approximately 2 nm [2].



Figure 2.1.17: Foam-like structure of the carbon nanopearls [2].

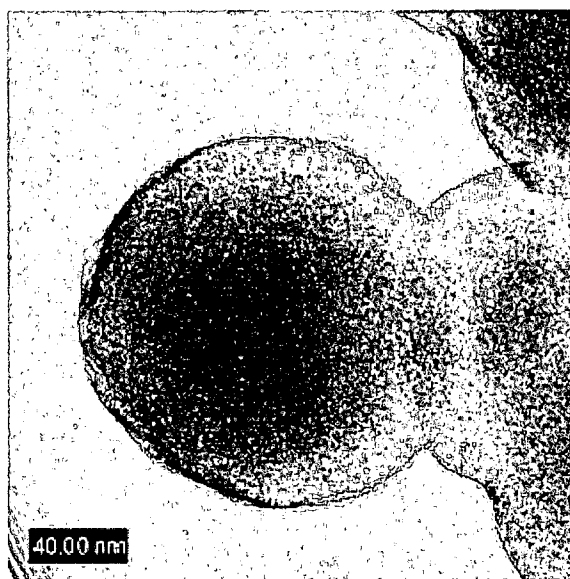


Figure 2.1.18: HRTEM image of a carbon nanopearl [2].

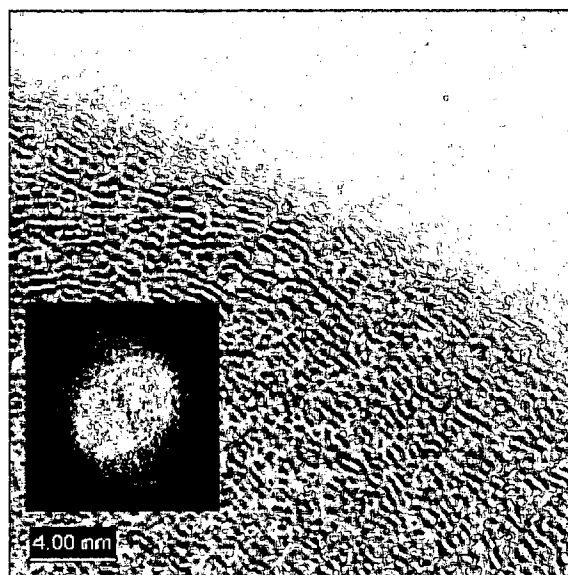


Figure 2.1.19: High magnification image at the surface of a carbon nanopearl [2].

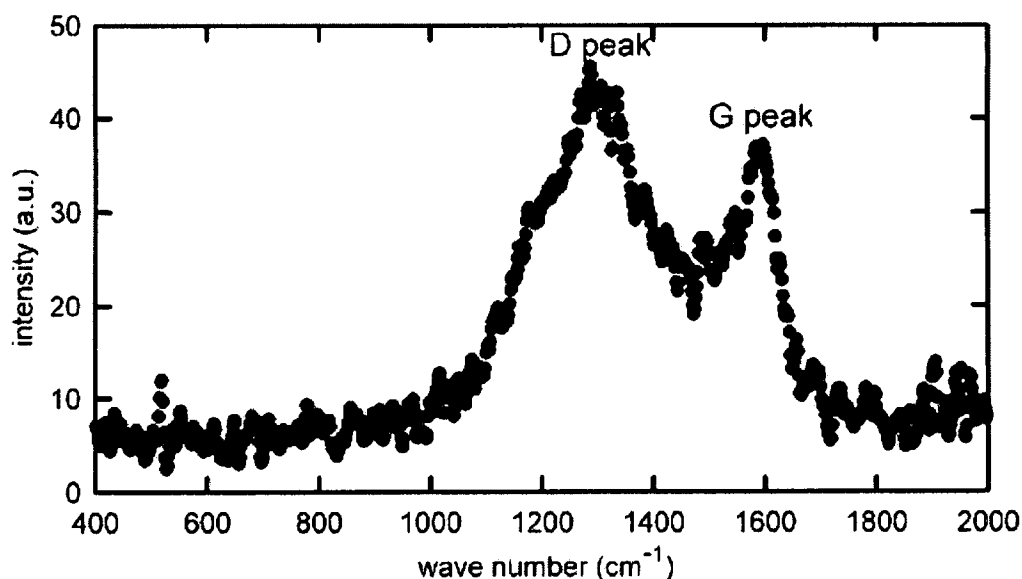
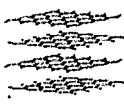



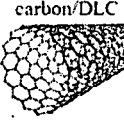




Figure 2.1.20: Raman spectrum of a carbon nanopearl [2].

2.1.8 Summary of properties of carbon forms

The ability of carbon atoms to undergo sp^2 and sp^3 orbital hybridization and to form large molecules (nanotubes and fullerenes) leads to vast ranges of properties in different forms of carbon. Typical properties of various forms of carbon are listed in

Table 2.1.2. In the next section, background information on tribology is presented, starting with historical perspective, definitions, and mechanisms and leading into a discussion of the tribological behavior of various carbon materials. Because of their spherical shape and concentrically oriented nano-sized sp^2 flakes, CNPs are promising for use in tribological solid lubricant coatings. While synthesis and characterization of CNPs has been documented in the literature, mechanical and tribological property studies have not been conducted to date.

Carbon allotrope or form	Bonding hybridization	Isotropy	Typical friction coefficients	Melting Point at 1 atm (K)	Density (g/cm ³)	Elastic modulus (GPa)	Electrical resistivity (Ω·m)	Thermal conductivity at 293 K (W/m·K)
 Graphite	sp ²	anisotropic	0.05-0.15 (air), 1 (vacuum)	4000 (sublimation occurs)	1.8 (commercial)	10 (commercial)	5-30 e-6 (commercial)	25-450 (commercial)
 Diamond	sp ³	isotropic	0.05-0.1 (air), 1 (vacuum)	3823	3.5	910-1250	10 ⁻¹¹	600-1000
 Fullerene (C ₆₀)	sp ²	isotropic	0.05-0.10, 0.4-0.6 (air), 0.5-0.7 (vacuum)	800K (sublimation occurs)	1.7			0.4
 Amorphous carbon/DLC	sp ² and sp ³	isotropic	0.07 (air), 0.17 (vacuum) [for DLC]	4000 (sublimation occurs)	1.8-2.8		10 ⁻¹¹ -10 ⁻¹²	400-1000
 Carbon nanotube	sp ²	anisotropic	0.2 (air), 0.2-0.7 (dry)			0.9	Wide range, depends on orientation	6600
 Carbon onion	sp ²	varies	<0.05 (air), <0.05 (vacuum)					
 Carbon nanopearl	sp ² and sp ³	isotropic	No data in literature					

CNPs: not investigated in literature but potentially useful for tribology

Table 2.1.2: Summary of typical physical properties of carbon in its various forms

2.2 Tribology of solids

2.2.1 Historical perspective

Tribology is defined as the science of the mechanisms of friction, lubrication, and wear of interacting surfaces that are in relative motion. Knowledge of tribology dates to ancient Egypt. A picture found on a wall of a grotto in El-Bersheh shows a colossus on a large sled being dragged along a heavy track by 172 Egyptians (Figure 2.2.1). One of the Egyptians is seen standing on the sled pouring a liquid onto the track in front of the sled to lubricate the track, with an estimated coefficient of friction of 0.23 [42]. In the late 1500's Leonardo Da Vinci first conceived of friction coefficient as a frictional force divided by normal load for sliding surfaces, and produced remarkably accurate conceptual sketches of modern bearings and friction test apparatus, though the notebooks containing these ideas were not revealed to the world until hundreds of years later [8]. Fundamental experimental laws governing friction of solid bodies were formulated by Coulomb in 1785 and are as follows: static friction may be greater than kinetic friction; friction is independent of sliding velocity; friction force is proportional to applied load; friction force is independent of contact area. Coulomb's laws are applicable in many instances but break down under numerous conditions [43].

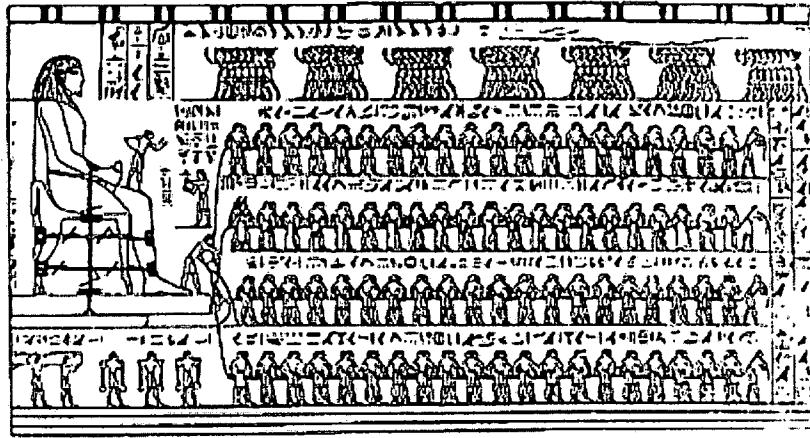


Figure 2.2.1: Picture found on a wall of a grotto in El-Bersheh showing Egyptians transporting a colossus ca 1800 BC.

2.2.2 Definitions and mechanisms

Friction force is defined as the resisting force tangential to the common boundary between two surfaces when there is relative motion between the surfaces as a result of external forces. Wear is defined as surface damage involving loss of material.

Friction and wear are system properties containing many interrelated factors including: asperity size distribution; surface finishing processes such as macrodeviations, waviness, roughness, and microroughness; segregation of solute or impurity atoms to the surface; reconstruction of surface layers due to change in composition; chemisorptions; chemical and mechanical compound formation; sub-surface microstructure (e.g. strain and plastic deformation in metals); surface lubrication condition (i.e. dry, lubricated, or boundary lubricated); environmental conditions such as temperature, pressure, humidity, and the presence of electrochemical species; and laboratory testing conditions and conditions of the test apparatus such as vibrations and specimen clamping [43].

Many interrelated mechanisms for friction and wear of materials exist. Some of these include: adhesion; mechanical interaction of surface asperities; plowing of asperities; deformation and/or fracture of surface layers such as oxides; interference and local plastic deformation caused by trapped (primarily wear) particles; shear fracture; extrusion; chip formation; tearing; brittle fracture; fatigue fracture; chemical dissolution; and diffusion [43].

2.2.3 Major laws governing friction and wear of solid lubricants

Relationships between friction force and metal substrate hardness derived and studied by Bowden and Tabor [44] can illustrate the beneficial effect of solid lubricant films for engineering design for low friction. Starting with the assumption that asperities on contact surfaces undergo deformation and reach a contact pressure equal to the indentation hardness of the material, the actual contact area is given by:

$$A_r = \frac{N}{H}$$

Where:

N = normal load

H = flow hardness

If friction is assumed to be due to shearing of bonds in asperities, the friction coefficient μ is given by:

$$\mu = \frac{F}{N} = \frac{A_r \tau}{A_r H} = \frac{\tau}{H}$$

Where:

F = friction force

τ = shear stress

Using the relation $F = A_r \tau$, the following scenarios (illustrated in Figure 2.2.2) show the effects of a hard metal in contact with a) a soft metal; b) a hard metal; and c) a hard metal with a solid lubricant thin film in the form of a soft metal. Scenarios a) (high contact area) and b) (high shear stress) lead to high friction coefficients while scenario c (low contact area and shear stress) lead to low friction coefficients [43,44].

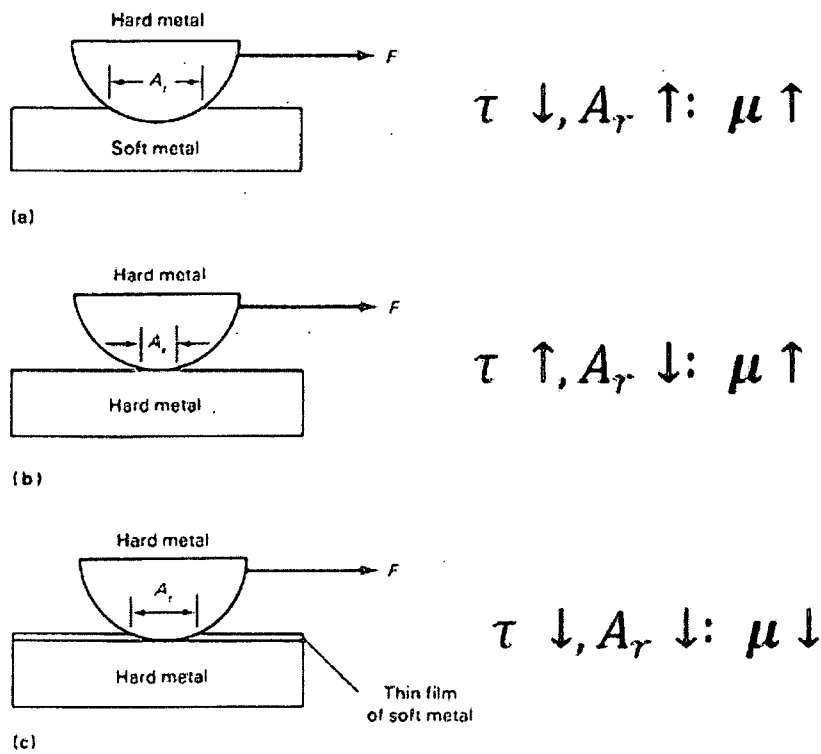


Figure 2.2.2: Relationship between actual contact area, shear stress, and friction coefficient for different contact regimes [43]

Because of the large number of variables governing wear of surfaces, and the lack of fundamental understanding of the effects and interactions of many of these variables, no equation exists that can reliably determine wear rates of surfaces. The best known equation was formulated by Archard in 1953 [45]:

$$Y = k \frac{WV}{H}$$

Where:

Y = wear rate

k = material-dependent wear coefficient

W = applied load

V = sliding speed

H = hardness (of the softer material of the pair)

The Archard equation and other wear rate formulas cannot be applied to all situations; in fact, some circumstances lead to contradictory conclusions. For example, some hardenable steels wear faster at low sliding speeds than they do at high sliding speeds [43]. For this reason, these relationships are used as broad engineering guidelines only.

2.2.4 Limitations of liquid lubricants

A lubricant is a gas, liquid, or solid substance introduced between two sliding surfaces in order to accommodate sliding of interfaces by self-shearing and thus reduce contact surface friction and wear, and to carry away heat and debris generated during the sliding process. Liquid lubricants such as oils and greases are extremely effective for many tribological applications; however, many applications require the use of solid lubricants, defined as thin films composed of a single solid or a combination of solids introduced between sliding surfaces for the purpose of reducing friction and wear. Liquid lubricants typically cannot be used in extreme environments such as temperatures above 500°C or space due their tendency to oxidize or decompose at high temperatures and vaporize or creep away from the interface under low pressures or vacuum conditions [43]. Liquid lubricants also

cannot be used in certain gear and bearing applications with excessive vibrations where they would be squeezed from the interface while solid lubricants would remain and protect surfaces from fretting corrosion and galling, or at temperatures below the freezing point of liquids.

2.2.5 Materials of interest for aerospace tribological applications

Solid lubrication is used for a number of aerospace applications in which the tribological behavior of various materials is of importance. In space environments, MoS₂, polytetrafluoroethylene (PTFE), and gold are commonly used solid lubricants because of their ability to provide lubrication in vacuum and under wide temperature ranges. Gold films deposited using magnetron sputtering are advantageous because the shear strength of the film in sliding contacts and thus its ability to provide lubrication does not depend on atmospheric pressure or the presence of water vapor. Structural materials of interest are high strength steels such as AISI 440C, a martensitic stainless steel with hardness ~58 HRC used for ball bearings and other applications requiring high strength and good oxidation resistance, and AISI M50, a tool/bearing steel with hardness ~61 HRC used in bearings for missiles and aircraft engines and applications requiring high wear resistance and strength up to 425°C. Another example application is microelectromechanical systems (MEMS), which contain microscopic moving parts carved from silicon wafers. Control of surface forces for MEMS devices such as contact-type RF MEMS switches, which contain gold at contact points, can be a primary factor controlling performance [46,47].

2.3 Tribology of carbon materials and carbon-based solid lubricants

2.3.1 Graphite

Graphite is a planar molecular with carbon atoms arranged in a hexagonal structure within each layer (Figure 2.1.1). As was discussed in Section 2.1.1, adjacent planes are bonded together by Van der Waals type forces. These forces are much weaker than the σ bonds within the planes and separate easily, accounting for the typical low friction of graphite [8]. However, the efficacy of graphite as a solid lubricant depends on the presence of water vapor [48]. Though the water molecules were previously believed to weaken the interplanar shear strength by an intercalation mechanism, recent evidence showed that the near-surface basal plane separation of graphite exposed to humid air is the same as that of the bulk [49,50]. This suggests that the molecules in the condensed vapors are instead absorbed selectively to the edge sites and saturate the dangling bonds, which reduces the adhesion to the mating surface resulting in lower friction [8].

2.3.2 Diamond-like carbon

During cyclic friction loading of DLC films, a graphitic or graphite-like interfacial transfer film is developed in the wear track during the run-in period of the test, which is characterized by a significant amount of film wear [50]. The tribological response of the system relates to the shear strength of transfer film layer and depends primarily

on environmental conditions (i.e. partial pressures of oxygen and water vapor) and the hydrogen content of the films [9]. For hydrogen-free DLC films, low friction and wear is observed in a humid environment as the shear process induces a carbon bonding structure change from sp^3 to sp^2 and friction is reduced by a molecular absorption mechanism similar to what occurs in graphite [50,12]. Also consistent with graphite behavior, friction coefficients higher than 0.35 have been observed for low hydrogen content DLCs in vacuum [9].

Hydrogenated DLC films may exhibit excellent friction and wear performance in vacuum or inert conditions if hydrogen is present near the surface of the film [51,52]. Highly hydrogenated DLC films (> 40 atomic % H) in inert or UHV conditions can exhibit ultralow friction ($\mu < 0.01$) by a mechanism in which the carbon film is passivated by hydrogen bonding to available carbon surface dangling bond sites, resulting in interfacial shear of hydrocarbon layers bound by weak van der Waals interactions [9]. Ultralow friction can also occur in hydrogenated films of lower hydrogen concentration if there is an available reservoir of unbounded hydrogen at the interface, brought about by introducing a gaseous hydrogen atmosphere to the test chamber [9].

2.3.3 Fullerenes

Tribological properties of fullerene thin films have been studied by many researchers because of the potential for C_{60} molecules to act as nano-sized rolling ball bearings in

friction contacts. Both nanometer to micron scale studies using Atomic Force Microscopy (AFM) or Frictional Force Microscopy (FFM) [53,54,55,56,57,58] as well as macro scale tests [59,60,61,62,63,1] have been performed. Results of these studies have not been consistent in regard to lubricity of C₆₀ films. The ability of C₆₀ to exhibit low friction coefficients appears to be sensitive to the magnitude of the normal load [54,55], and the dispersion of C₆₀ molecules in the film [57,58].

Inconsistencies could also be due to different surfaces and counter-faces used in the friction testing and a film thickness effect. Researchers have observed that under some test conditions C₆₀ powder tends to form dense clumps characterized by high shear strength in friction contacts, leading to high friction coefficients [59,61,62].

2.3.4 Carbon onions

While a relatively few number of tribological studies of carbon onions have been reported in the literature, carbon onion films have exhibited superior friction and wear performance both in raw form and as a lubricant additive [1,22,31,64,65,66]. Results of these studies are summarized in the following section.

Hirata, et. al., studied the solid lubricant properties of carbon onions produced by heat treatment of detonation-synthesized diamond clusters (5-10 nm in diameter) or diamond particles (with size distributions of <0.1, 0.25, or 0.5 μm) [1]. Friction coefficients and wear rates in air and vacuum were measured using a ball-on-disk type tribometer, which consisted of a 1/8" diameter steel ball bearing and a (1 0 0)

silicon wafer with a mirror-finished surface. Carbon onions produced using the diamond clusters and diamond particles $< 0.1 \mu\text{m}$ were evaluated, along with three reference lubricants: raw diamond clusters used to produce the onions; graphite particles with an average diameter of $25 \mu\text{m}$; and a mixture of C_{60} and C_{70} particles. Ten milligrams of each specimen were spread over a wafer, and friction coefficients at a normal force of 0.95 N and a sliding speed of 6.3 mm/sec were measured [1].

In air, the graphite powder and the two types of carbon onions reduced the friction coefficient compared to the unlubricated specimen. The diamond cluster-prepared carbon onions had the lowest friction coefficient of any of the lubricants tested, which remained stable over the duration of the test (Figure 2.3.1). The friction coefficients for carbon onions prepared using diamond particles $< 0.1 \mu\text{m}$ increased to values higher than those of graphite during the test. The increase was attributed to the dissipation of the carbon onions during the test due to their larger particle size compared to diamond cluster-prepared onions [1].

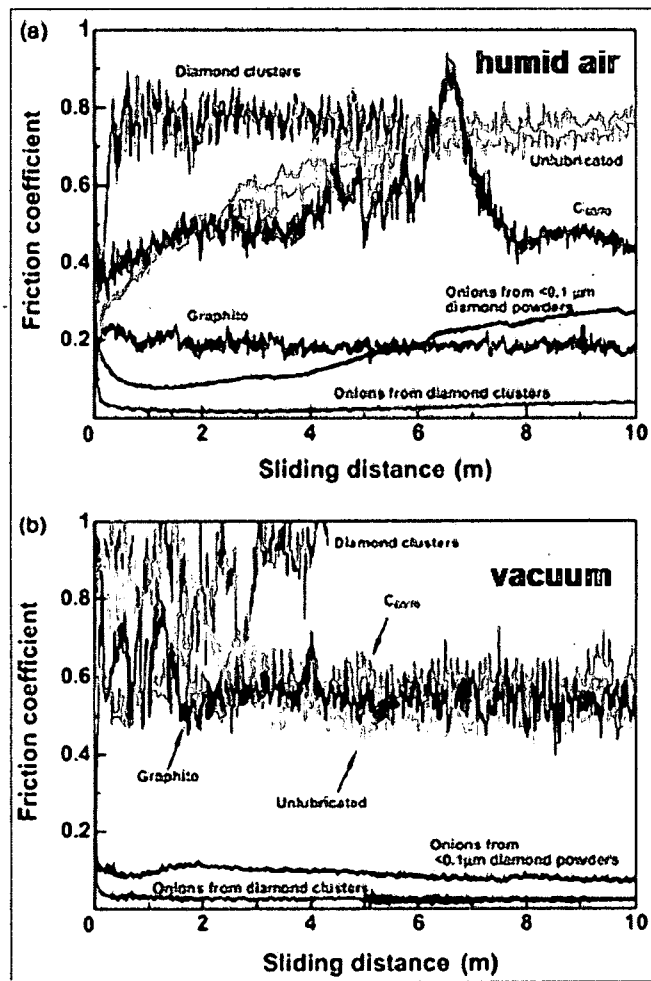


Figure 2.3.1: Friction coefficient variations for carbon onions, graphite, diamond clusters, and C₆₀/C₇₀ on Si (1 0 0) as a function of sliding distance in a) air at 55% relative humidity; b) vacuum at 1.3×10^{-3} Pa [1].

In vacuum, the graphite particles were not effective as a lubricant, while both types of carbon onions maintained low friction coefficients throughout the test. The improved friction behavior in vacuum of the carbon onions was attributed to the closed structure of the graphene sheets, which produces only weak π electrons bonds on the outer shell. Figure 2.3.2 shows wear scars on steel balls after friction testing. The wear rates of the carbon onion specimens were $10^{-10} - 10^{-12}$ mm³/N-m, compared to $10^{-6} - 10^{-7}$ mm³/N-m for graphite and C₆₀/C₇₀ [1].

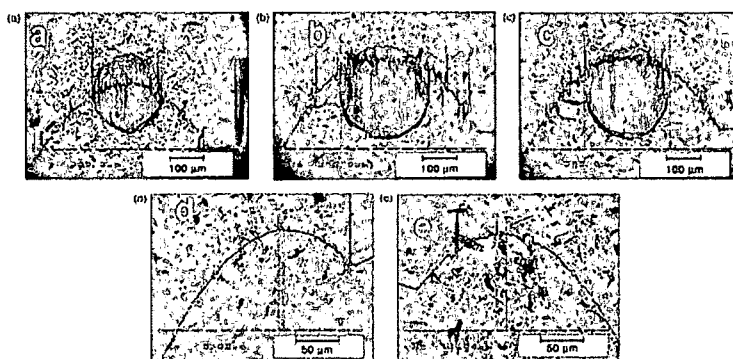


Figure 2.3.2: Wear scars on steel balls after friction testing in vacuum using: a) no lubricant; b) graphite; c) C_{60/70}; d) carbon onions synthesized from diamond clusters; e) carbon onions synthesized from diamond particles

Additional tests were performed in order to evaluate the effect of surface roughness on the friction behavior of the carbon onions. Friction coefficient was measured on silicon wafers scratched with alumina powders to give a range of surface roughness values, at a normal force of 0.11 N and a sliding distance of 5 m, in both air and vacuum. The results are shown in Figure 2.3.3. In air, the friction coefficient for carbon onions prepared using diamond clusters increased with surface roughness because the surface asperities are larger than the carbon onions, whereas the carbon onions produced by diamond particles maintain a lower friction coefficient at higher roughness (Figure 2.3.3a). This effect was attributed to aggregation of onions produced by diamond particles in the humid air environment. In vacuum, the friction coefficients increased as surface roughness increased for all except the largest carbon onions, those produced using diamond particles $< 0.5 \mu\text{m}$ (Figure 2.3.3b). The carbon onions are believed to segregate easily in the absence of moisture, which allows them to hide in the bottom of the asperities on the rougher surfaces, except for the largest carbon onions (produced using diamond particles $< 0.5 \mu\text{m}$).

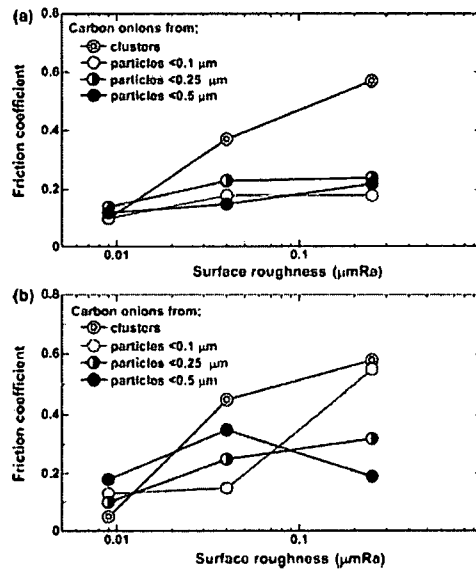


Figure 2.3.3: Friction coefficients as a function of surface roughness for (100) Si discs (a) in air and (b) in vacuum [1].

The authors suggest a mechanism for the tribological behavior of carbon onions, depicted in Figure 2.3.4. Low friction and wear is believed to be caused by the weak interaction between the outermost shell of the carbon onions and the counterpart surfaces, which results in very low adhesion and the ability to provide a lubricating layer between the surfaces. High friction results when the outermost shells of the carbon onions contain defects or if they are small enough to hide below the surface asperities.

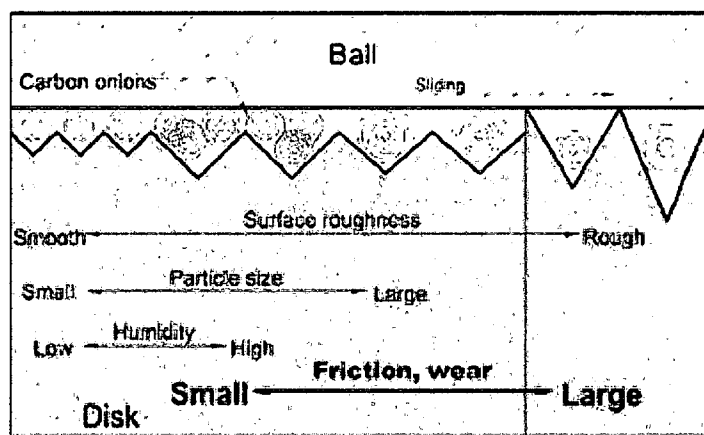


Figure 2.3.4: Schematic illustration of tribological behavior of carbon onions on sliding surfaces.

A number of researchers have studied the tribological properties of carbon onions as a lubricant additive. Carbon onions added to poly-alpha-olefin (PAO) base oil have been found by several researchers to reduce friction [31,64]. Another study found that carbon onions had superior friction and wear performance compared to graphite powder used as additives to PAO base oil and attributed the friction performance to the carbon onions' role in conversion of large abrasive wear particle to ultrafine lubricious iron oxide particles [65]. Street, et al. studied the effect of a suspension of faceted, hollow carbon onions (Figure 2.1.8b) in Krytox 143AB lubricating oil on tribological behavior of 440C stainless steel surfaces. No improvement in lifetime or friction coefficient was observed vs. the control (Krytox 143AB without nano-onions) in a vacuum environment. However, the authors state that a significant improvement in lifetime occurred in an air environment with the nano-onion addition. The improvement was attributed to the ability of the onions to act as a back-up lubricant [22]. Yao, et al. studied tribological properties of carbon onions synthesized using arc discharge in water between graphite electrodes added to commercial lubricating

oil. The authors reported a reduction in friction coefficient with the addition of carbon onions to the lubricating oil [66].

In summary, carbon onions reduce friction coefficients both in as-synthesized form and as lubricant additives. Superior friction performance of carbon onions has been attributed to the weak interaction between the outermost shell of the carbon onions and the counterpart surfaces, which results in very low adhesion, and to the ability of carbon onions to convert large abrasive wear particles to ultrafine iron oxide particles on steel surfaces.

2.3.5 Carbon nanotubes

Carbon nanotubes (CNT) are another example of closed wrapped graphene plane nanostructures which have been evaluated for tribological applications, with mixed results [67,68,69,70]. Friction properties of multi-walled carbon nanotubes were found to be highly anisotropic. Multi-walled nanotubes aligned perpendicular to the contact plane showed consistently high friction coefficients while those laying flat on the contact surface showed low friction coefficients [69]. In another study, vertically aligned multi-walled CNT arrays were found to have low friction coefficients under lower contact loads and high friction coefficients under high friction loads, and the CNT arrays were compressed to form graphite-like films [70]. These studies with CNTs suggest that in order to reduce friction with carbon nanostructures, the graphene planes should be oriented parallel to the sliding direction. In addition, many

researchers have investigated CNT composites due to enhanced wear resistance of these materials (for example, Jacobs, et al. [71]).

2.4 Summary of literature analyses and hypothesis for tribology of carbon nanopearls

Graphitic structures are effective for lubrication because of very strong in-plane σ bonds and weak π bonds between planes that allow easy sliding of planes in humid environments, where condensed vapor molecules bond to basal plane edge sites and saturate the dangling bonds. Closed graphitic structures are even more desirable because of the absence of edge sites that can form strong bonds in the absence of absorbed vapor molecules and cause high friction and wear. Furthermore, spherical structures offer an advantage over CNT due to their isotropy – the lubrication effect does not depend on orientation. Because of their concentrically-oriented graphene flake structure and larger size, carbon nanopearls have the potential to provide more effective solid lubrication for macro-level contacts compared to closed shell carbon nanostructures. One possible mechanism by which carbon nanopearl lubrication could occur is for the CNPs to act as nano-scale rolling ball bearings, as has been proposed for fullerenes and carbon onions. Because of their larger size (> 100 nm) compared to C_{60} and carbon onions, CNPs have the advantage of being larger than asperities on smooth contact surfaces, enabling effective lubrication without the “hiding” effect observed with carbon onions. Since mechanical properties of CNP have not been investigated in the literature, it is not known if CNPs have sufficient

strength to retain their spherical shape under contact loading, or if they would undergo deformation, either by exfoliating graphene flakes and amorphous carbon as they roll between surfaces or by being highly deformed and flattened. If permanent deformation occurs, the individual flakes might be peeled off and cover the sliding contact surface with graphene basal planes aligned parallel to the sliding direction. These scenarios are depicted schematically in Figure 2.4.1. In order to investigate these mechanisms, detailed experimentation is needed to understand the behavior of CNP in tribological contacts. These experiments involve synthesis of thin films composed of CNP. Methodology for CNP film synthesis is described in the following sections.

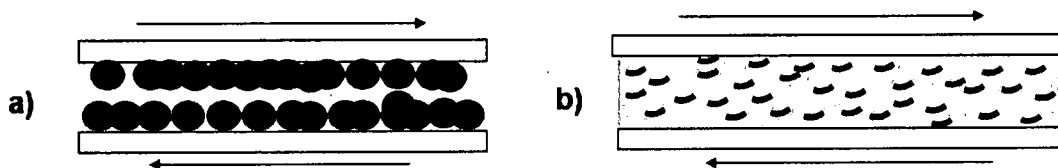


Figure 2.4.1: Hypothetical contact mechanisms for carbon nanopearls: a) Ball bearing effect in which CNPs remain intact and roll past opposing surfaces and each other; b) Nanopearls are flattened and smeared and the graphene flakes are distributed between the opposing contact surfaces.

2.5 Potential deposition methods for carbon nanopearl films

Tribological studies of CNPs would consist of placing the material, which has a foam-like powder form, onto surfaces in the as-synthesized condition. Using a drop-casting method in which the CNPs are dissolved in a solvent and dropped onto a surface would allow the material to be flattened and spread out on the surface.

Another method that has the potential to produce films with suitable distribution of

CNPs for tribological testing is matrix assisted pulsed laser evaporation (MAPLE).

MAPLE is a vacuum deposition technique related to pulsed laser deposition in which solute particles are suspended in a volatile solvent and frozen into solid laser targets and will be described in greater detail in a subsequent section.

It would also be useful to study the behavior of a solid lubricant CNP composite film, which would allow insights into the ability of CNPs to reduce friction as coating wear takes place, with the added advantage that the CNPs would remain anchored in place as part of the composite film rather than possibly being pushed to the side of a sliding contact in a friction test. A gold-CNP composite system would be ideal since gold is a non-reactive metal with relatively low wear resistance and has applications as a vacuum lubricant and in MEMS devices.

In order to synthesize these gold-CNP composite materials, a novel technique which combines MAPLE and magnetron sputtering has been developed. Because of the nature of the pulsed laser deposition process and the potential for interaction of solvent vapors with sputter plasmas, there is a need to understand the interaction of neutral and ionic species during composite film formation. In order to perform this study, Electrostatic Quadrupole Plasma (EQP) mass spectroscopy, a plasma diagnostic technique that allows quantitative measurement of the energy and mass-to-charge ratio distributions of ions, neutrals, and radicals, will be used. Information on MAPLE and EQP techniques will be presented in the following sections.

2.6 MAPLE

MAPLE is a technique in which a polymer or other organic material is deposited on a substrate surface in a vacuum chamber using an excimer laser to evaporate a frozen target consisting of polymer or other organic compound dissolved in a volatile solvent matrix. The laser pulses vaporize the solvent and heat the polymer or organic molecules, causing them to enter the gas phase. A coating from the evaporated solute material is formed on the substrate surface, while the volatile solvent molecules are evacuated by the vacuum pump in the deposition chamber [3]. The process is similar to pulsed laser deposition, in which material is ablated from the (usually organic) target surface in the form of small molecules, ions, and atoms and settles onto the substrate to form crystalline bonds. In MAPLE, the energy from laser pulses are absorbed primarily by the frozen solvent matrix, and thus allows film deposition to occur with little or no damage to the transported solute material [3,4,5,6]. These processes are illustrated schematically in Figure 2.6.1.

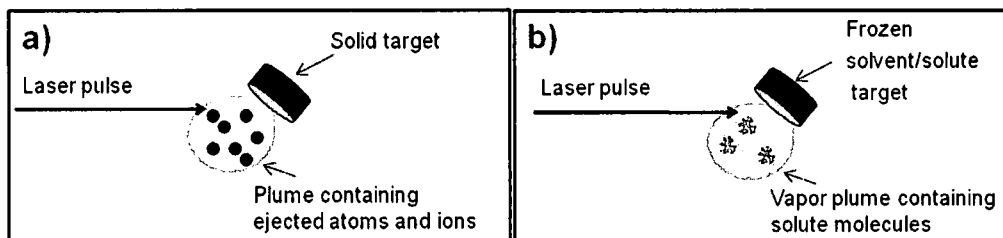


Figure 2.6.1: Schematic illustrations of a) pulsed laser deposition and b) MAPLE

A wide range of solvents have been studied using MAPLE, including distilled water, dichloromethane, DMSO/PBS (Dimethyl sulfoxide/ phosphate buffered solution),

chloroform, ethyl-acetate, DMSO, dimethylformamide, benzene, toluene, acetone, and phys. serum [72]. Typically, solvents having a high absorption at the applicable laser energy are selected, though low wavelength absorbing solvents can be also used due to the laser energy trapping on inhomogeneities and cracks of the frozen target surfaces [72]. Solvent selection is a critical component for the successful homogenous deposition of a selected material. Some of the key parameters include: solubility and surface wettability of the desired solute material, laser absorption coefficient of the solvent material, solution vapor pressure, laser penetration depth, solution freezing temperature, and heat capacity. Since the extent to which each of these effects has on the final film is largely unknown, it is important to look a large group of solvents before optimization of deposited films continues.

MAPLE can be used to deposit broad range of polymeric, organic, and biomaterial films for a variety of applications. Examples of include films of fibrogen, cryoglobulin, PVA (polyvinyl alcohol), pullulan (Triacetate, Cinnamate, Tosylate), SnAcAc (Tin(IV) acetylacetonate dichloride), PhNi (Nickel(II) phtalocyanine), CTPP/CHCl₃ (Cu(II) para-paramethylphenylporphyrin), polypyrrol, Glycolid, BSA (bovine serum albumin), and PEG (polyethylene glycol) [72].

There have been only a limited number of studies of MAPLE processes for depositing carbon nanostructures. Because of its ability to transport molecules using vapor to deposit disperse films while keeping the molecular structure and properties of solute material intact, MAPLE is a promising technique for depositing CNP films. In developing the deposition process, the effect of various deposition parameters (e.g.

laser energy and repetition rate, background pressure and gas composition, substrate temperature) would need to be investigated to optimize the process. These studies have not been performed in the literature to date. In addition, hybrid processes could be developed combining MAPLE with other deposition techniques such as magnetron sputtering to create a bonding matrix to encapsulate the relatively inert CNPs by creating a composite material. Development of these processes would necessitate understanding the species that would evolved within the deposition chamber as the dual processes are occurring, which can be accomplished using Electrostatic Quadrupole Plasma (EQP) mass spectroscopy analysis. The technique is described in the following section.

2.7 Electrostatic Quadrupole Plasma (EQP) mass spectroscopy analysis

Electrostatic Quadrupole Plasma (EQP) analysis is a plasma diagnostic technique that allows quantitative measurement of the energy and mass-to-charge ratio distributions of ions, neutrals, or radicals generated in a source plasma. Early studies of sputtering and etching discharges using EQP were performed by Coburn and Kay [73,74]. The key components on an EQP (shown schematically in Figure 2.7.1) are the energy sector analyzer (ESA) and the quadrupole mass spectrometer (QMS). The ESA consists of two curved plates which are positively (outside plate) and negatively (inside plate) charged. Ions generated by the plasma enter the EQP but only those with a specific kinetic energy, for which the centrifugal and electrostatic forces are

equal, can pass through the ESA and enter the Secondary Electron Multiplier (SEM) detector. Analysis of neutrals can also be performed by activating the ionizer [75].

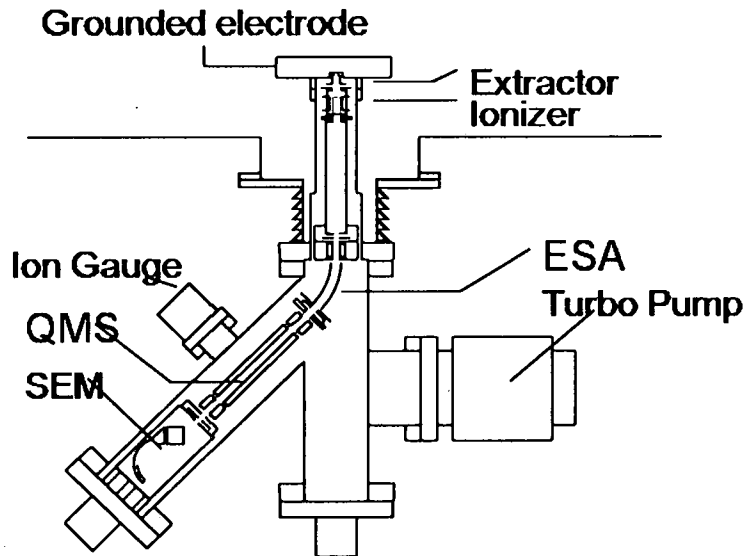


Figure 2.7.1: Schematic illustration of EQP analyzer

The QMS consists of four cylindrical rods that produce a two-dimensional quadrupole by superimposing radio frequency (RF) and direct current (DC) potentials on the rods. When the RF and DC potentials are set to a certain critical ratio, only ions of a specific mass to charge ratio can pass through the rods to the SEM detector [75].

The ESA and QMS enable measurement of the mass distributions of neutral or ion species at a specific energy and the energy distributions of neutral or ion species of a specific mass-to-charge ratio. A detailed discussion of the operation of EQP instruments can be found in a thesis by Muratore [75]. Because it allows quantitative

measurement of species generated by plasma and other vacuum processes, EQP is an ideal tool to study mechanisms of film formation during simultaneous MAPLE/magnetron sputtering. This is particularly true because during MAPLE a pulsed laser vaporizes solvent contained in the frozen target and this vapor has the potential to interact with other processes taking place during the deposition, i.e. sputtering and film formation. The EQP analysis will allow a detailed understanding of the interaction of these dual processes.

2.8 Summary

The ability of carbon atoms to undergo sp^2 and sp^3 orbital hybridization and to form large molecules such as nanotubes and fullerenes leads to vast ranges of properties in different forms of carbon. For tribological applications, graphite is useful as a solid lubricant because of very strong in-plane σ bonds and weak π bonds between planes that allow easy sliding of basal planes. Fullerenes and carbon onions are closed spherical graphitic structures that are advantageous for tribological applications because of their isotropy and the fact that they can remain effective in dry and vacuum environments due to the absence of edge sites. Carbon nanopearls, which are spherical amorphous carbon structures containing concentrically-oriented nano-sized sp^2 flake structure, are larger than carbon onions and have the potential to provide more effective solid lubrication for macro-level contacts. Possible mechanisms by which carbon nanopearl lubrication could occur are for the CNPs to remain intact and act as nano-scale rolling ball bearings or they may undergo deformation, either by

exfoliating graphene flakes and amorphous carbon as they roll between surfaces or by being completely highly deformed and flattened, as has been proposed for fullerenes and carbon onions. In order to investigate these mechanisms, detailed experimentation is needed to understand the behavior of CNP in tribological contacts.

In order to conduct the necessary tribological experiments, thin films composed of CNP must be synthesized. Deposition methods will include drop casting, MAPLE, and MAPLE with magnetron sputtering using a gold sputter target to create a nanostructured hybrid film. The advantage of the latter is that the CNPs would remain anchored in place as part of the composite film rather than possibly being pushed to the side of a sliding contact in a friction test. Since there have been only a limited number of studies of MAPLE processes for depositing carbon nanostructures, the effect of various deposition parameters would need to be investigated to optimize the process. Because of the nature of the pulsed laser deposition process and the potential for interaction of solvent vapors with sputter plasmas, there is a need to understand the interaction of neutral and ionic species during composite film formation. In order to perform this study, Electrostatic Quadrupole Plasma (EQP) mass spectroscopy, a plasma diagnostic technique that allows quantitative measurement of the energy and mass-to-charge ratio distributions of ions, neutrals, and radicals, will be used. A statement of objectives, along with a list of associated tasks to meet these objectives, will be given in the next chapter.

3. RESEARCH OBJECTIVES

The objectives of this research program are as follows:

To investigate the structure, chemistry, morphology, and formation mechanisms of carbon nanopearl films prepared by different methods: drop casting, MAPLE, and MAPLE with magnetron sputtering.

To accomplish this objective, CNP films need to be deposited and characterized. This is accomplished by drop cast deposition using CNP/methanol solution, by developing and optimizing methodology to deposit CNP films using MAPLE, and by developing processes to deposit nanostructured hybrid films consisting of CNPs in a gold matrix by combining MAPLE and magnetron sputtering. Development of MAPLE to deposit CNP films requires study of the effect of processing parameters on the morphology of the films as assessed by optical microscopy and image analysis. Process development for MAPLE with magnetron sputtering requires a study of species present using EQP. In this study, neutral and ionic species are monitored within the deposition chamber for a number of experimental conditions. Deposited films are characterized using optical microscopy, Scanning Electron Microscopy with Energy Dispersive Spectrometry (SEM/EDS), X-ray Photoelectron Spectroscopy (XPS), and Raman spectroscopy. In addition, a discussion of the relationship

between processing parameters and the nature of the nanostructured hybrid thin films deposited by MAPLE and magnetron sputtering is presented.

To correlate the structure, chemistry, morphology of carbon nanopearl films with their friction and wear behavior.

Tribological testing is performed on the deposited CNP films in humid air and dry nitrogen environments using a ball-on-disk tribometer and a fretting wear tester, during which friction coefficient measurements is performed. Wear surfaces are characterized using optical microscopy, SEM/EDS, and Raman spectroscopy.

To establish a fundamental understanding of tribological contact mechanisms of carbon nanopearl films.

Comparison of friction coefficient data of the CNP films to results from the characterization of the as-deposited and wear surfaces reveals insights into the underlying mechanisms of CNP lubrication. These conclusions are compared to the hypotheses suggested in the previous chapter.

4. EXPERIMENTAL METHODS

Carbon nanopearls synthesized using a CVD process [2] were obtained for this study. As-received carbon nanopearls were characterized using SEM, TEM, XRD, and Raman spectroscopy; results of these studies will be described in Chapter 5. In this chapter, the materials substrates used for thin films, deposition methods for carbon nanopearl thin films, tribological testing of carbon nanopearl thin films including ball-on-disk and fretting wear, and characterization of carbon nanopearl thin films are described. In addition, methods for studying film formation using EQP during MAPLE and MAPLE with magnetron sputtering will be discussed.

4.1 Substrate and Test Materials

CNP thin films were deposited onto substrates consisting of silicon wafers, AISI 440C steel, or AISI M50 steel disks, which were identified in section 2.2.5 as important materials for sliding and rolling friction components for aerospace mechanisms. Counter surfaces for tribological tests consisted of a M50 steel ellipsoid for fretting wear tests and 440C steel ball bearings for ball-on-disk tribometer tests. The silicon wafer substrates were 25.4 mm in diameter, either 254 or 525 μm in thickness, and doped with either phosphorus or boron for low resistivity ($\geq 0.1 \Omega\text{-cm}$ for B-doped, 2-8 $\Omega\text{-cm}$ for P-doped). The surfaces were (100)-oriented and polished

to a mirror finish. The 440C steel was heat treated to a hardness of 59 HRC. The dimensions of the AISI 440C steel disks were 2.54 cm diameter and 0.30 cm thickness, and the surface was polished to an ultra-smooth (< 50 nm) finish. Counter surfaces for ball-on-disk tribometer tests consisted of 25.4 mm diameter AISI 440C steel ball bearings. The AISI M50 steel disks used for fretting wear tests were 12.7 mm in diameter and 4 mm in thickness, and had a surface roughness of approximately 100 nm. The AISI M50 ellipsoid used for the fretting wear tests were 12 mm in diameter at the center and 12.7 mm in length, with a roughness of approximately 45 nm.

4.2 Carbon nanopearl film deposition methods

4.2.1 Drop cast deposition

Carbon nanopearls were applied to the surfaces of 1 inch diameter flat silicon wafer disks and 0.5 inch diameter M50 steel disks using a drop casting method. CNPs were mixed with methanol, ultrasonically agitated, and applied to the substrates using a pipette dropper. The methanol was then allowed to evaporate, leaving behind the deposited CNP film.

4.2.2 MAPLE

4.2.2.1 Equipment

The MAPLE system is contained within a vacuum chamber equipped with two load locks each containing separate turbo pumps that allow frozen MAPLE targets and film substrates to be inserted and removed without the need to vent the vacuum system to atmosphere (Figure 4.2.1). Two magnetron sputtering sources are installed containing gold and chromium targets, which can be operated simultaneously with the MAPLE process to create nanostructured hybrid films consisting of nanoparticles embedded in metal matrices. The specimen assembly utilizes a translation stage to allow control of the distance and angle of the specimen from the laser target and the magnetron sputtering source. The substrate stage and the MAPLE target stage are attached to variable speed motors to enable rotation. The specimen stage is configured to apply up to 1 kV negative potential bias to the substrate and control the temperature from room temperature to 500°C. The vacuum chamber also contains a Hiden EQP analyzer which enables quantitative measurement of mass distributions of ion and neutral species (Figure 4.2.2). A Lambda Physik LPX 305i KrF 248 nm excimer laser source with a maximum rated pulse energy of 1200 mJ operating at 5 Hz and 23 kV is used for the MAPLE process.

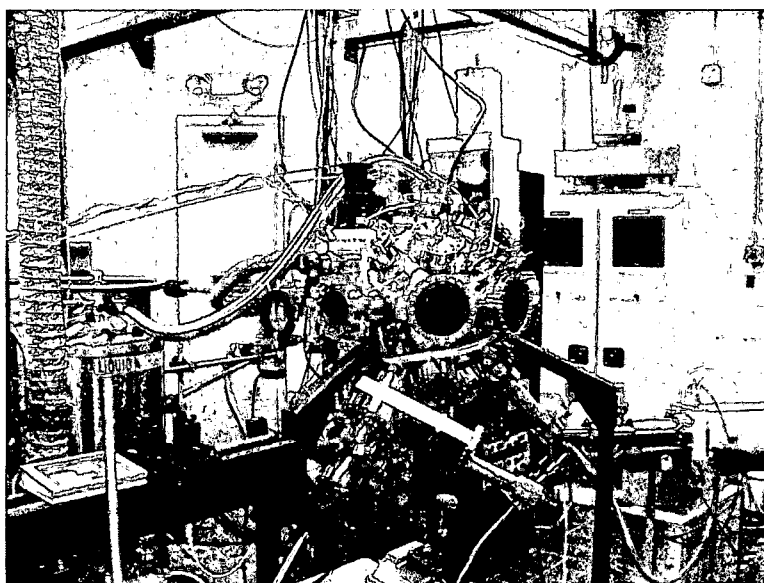


Figure 4.2.1: MAPLE system used to deposit carbon nanopearl thin films

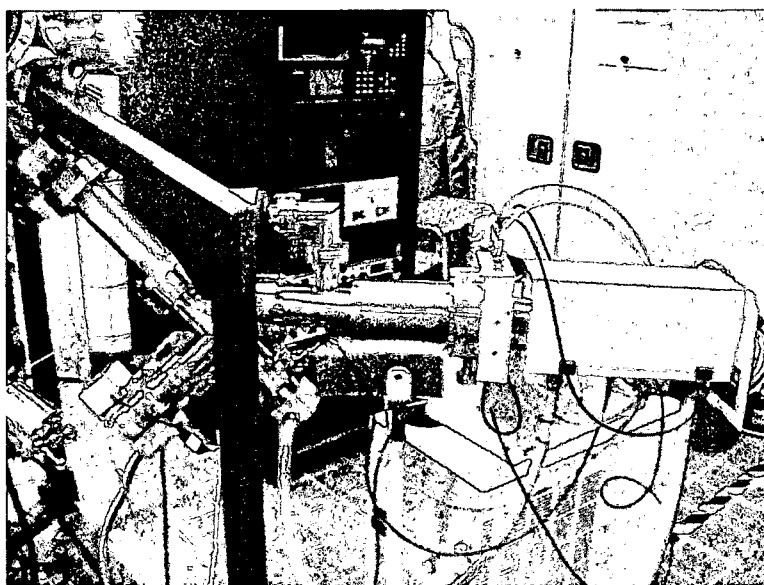


Figure 4.2.2: EQP analyzer

A glove box filled with dry nitrogen gas positive pressure (shown in Figure 4.2.3) is used to prepare laser targets in order to avoid introducing moisture to the vacuum chamber through the load lock. A beaker containing the target solution is placed

within the glove box and agitated ultrasonically to mix the CNPs with the solvent, which is necessary to obtain uniform targets because the CNPs tend to agglomerate into large clusters. The target solution is applied to copper target holder via pipette, and the holder is lowered into a reservoir of liquid nitrogen to freeze the dispersed solution. The frozen target is placed into a transfer chamber (Figure 4.2.3) which is sealed via a gate valve then removed from the glove box and loaded onto vacuum chamber load lock. The load lock chamber is then evacuated. Once the vacuum pressure is sufficiently low the load lock gate valve is opened and the target is attached with a transfer arm onto the liquid nitrogen-chilled target stage within the vacuum chamber.

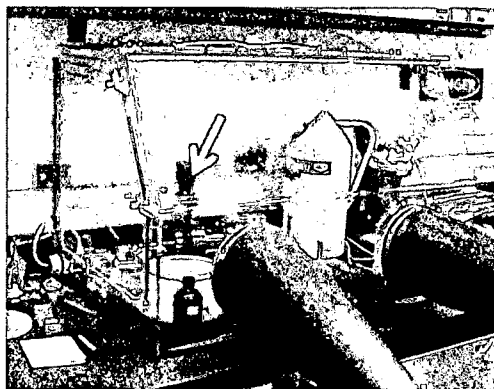


Figure 4.2.3: Glove box used for preparation of frozen MAPLE targets. Arrow indicates sealable chamber for transporting frozen targets from the glovebox to the deposition chamber

4.2.2.2 MAPLE process study experimental details

Target solutions were made by adding carbon nanopearls to various solvents at an approximate concentration of 0.08 wt. %. Prior to freezing, the beaker containing the

target solution was placed in a small ultrasonic cleaner (maximum output power: 12W) for 1-5 minutes. During the deposition process for all synthesized films, the laser spot was focused onto the target in a square pattern approximately 17.7 mm per side. The laser target and substrate were rotated at 21 rpm for all depositions.

Carbon nanopearl films were deposited using MAPLE with eighteen different processing parameters (Table 4.2.1). This enabled study of: i) effects of solvent material - acetone, dimethyl sulfoxide (DMSO), dimethyl formadine (DMF), toluene, methanol (MtOH), and ethyl acetate (Et-Ace); ii) laser repetition rate - 1, 3, and 5 Hz; iii) laser pulse energy - 500, 600, and 700 mJ; iv) substrate temperature - 20, 100, and 200°C; and v) background pressure - vacuum (unregulated pressure, no background gas added), 2.67 Pa argon, and 13.33 Pa argon. The argon gas pressure in the vacuum chamber was regulated using a mass flow controller at 2.67 and 13.33 Pa.

Solvent	Laser repetition rate (Hz)	Laser energy (mJ)	Deposition time (min)	Substrate temperature	Background pressure	Background gas	Max deposition pressure	Area fraction covered (%)
Acetone	1	500	7	Ambient	2.67 Pa	Argon	2.67 Pa	8
Acetone	3	500	7	Ambient	2.67 Pa	Argon	2.67 Pa	8
Acetone	5	500	7	Ambient	2.67 Pa	Argon	2.67 Pa	15
Acetone	3	600	7	Ambient	2.67 Pa	Argon	2.67 Pa	15
Acetone	3	700	7	Ambient	2.67 Pa	Argon	2.67 Pa	19
Acetone	3	500	7	100 °C	2.67 Pa	Argon	2.67 Pa	10
Acetone	3	500	7	140 °C	2.67 Pa	Argon	2.67 Pa	8
Acetone	3	500	7	200 °C	2.67 Pa	Argon	2.67 Pa	4
Acetone	3	500	7	300 °C	2.67 Pa	Argon	2.67 Pa	1
Acetone	3	500	7	Ambient	Vacuum	N/A	2.67e-2 Pa	17
Acetone	3	500	7	100 °C	Vacuum	N/A	2.53e-2 Pa	12
Acetone	3	500	7	200 °C	Vacuum	N/A	3.2e-2 Pa	2
Acetone	3	500	7	Ambient	13.33 Pa	Argon	13.33 Pa	9
DMSO	3	500	7	Ambient	Vacuum	N/A	1.47e-2 Pa	2
DMF	3	500	7	Ambient	Vacuum	N/A	1.47e-2 Pa	18
Toluene	3	500	7	Ambient	Vacuum	N/A	2.53e-2 Pa	26
MtOH	3	500	7	Ambient	Vacuum	N/A	6.27e-2 Pa	2
Et-Ace	3	500	7	Ambient	Vacuum	N/A	6.27e-2 Pa	17

Table 4.2.1: List of investigated MAPLE process settings

The silicon wafers containing the deposited films were examined using an optical microscope at magnifications of 50X and 1000X. In addition, samples were

examined using SEM. The area fraction of sample surface covered with nanopearls was calculated using a MATLAB program. The mean threshold, minus one half of the standard deviation of the threshold, was computed by MATLAB and used to generate the binary image and compute the area fraction of surface covered by nanopearls, unless the assymetrical illumination effect was noticed. In that case the highest threshold for which the assymetrical effect could not be detected by eye was used to compute the area fraction. This analysis allowed comparison of the amount of material deposited on substrate surfaces under different experimental conditions. An example of a processed image is shown in Figure 4.2.4.

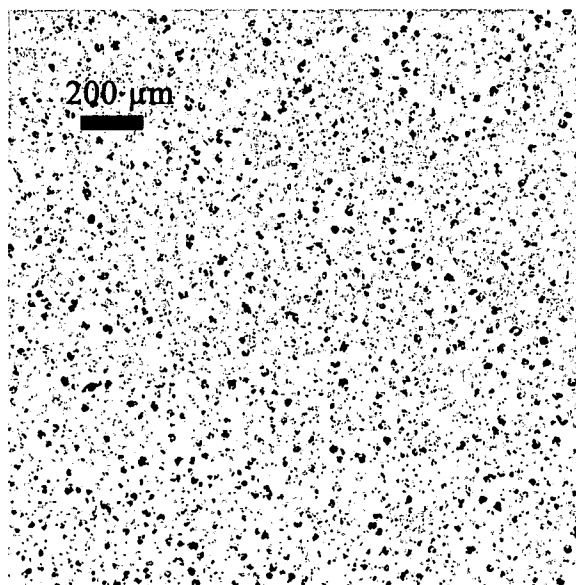


Figure 4.2.4: Optical image of CNPs deposited onto a silicon wafer by MAPLE after image processing using MATLAB program

4.2.3 MAPLE with magnetron sputtering experimental details

Fifteen nanostructured hybrid films were deposited onto silicon wafers or 440C steel disks using MAPLE combined with magnetron sputtering; Table 4.2.2 contains a list of MAPLE deposition parameters and process sequences used these films. After rinsing with methanol, substrates were inserted into the vacuum chamber and plasma etched by applying a substrate bias of 800-1000V in argon, regulated using a mass flow controller at a pressure of 2-13.33 Pa at a flow rate of 100 sccm. MAPLE targets consisting of 0.08 wt. % carbon nanopearls in toluene or toluene (neat) were prepared, using procedures discussed in the previous section, and inserted into the MAPLE chamber. The temperature of the substrate during the depositions was either 100°C or ambient laboratory temperature (~20 °C). For some films, an interfacial film layer consisting of gold or a mixture of chromium and gold was deposited onto the substrates using magnetron sputtering in an argon atmosphere at a pressure of 2.00 or 2.67 Pa. MAPLE was operated for 15-60 minutes with the laser energy set to 700 mJ and a repetition rate of 1 Hz for all depositions. The background pressure in the MAPLE chamber during depositions was 2.00 Pa or 2.67 Pa, regulated using mass flow controllers and a mixture of oxygen and argon gases, or unregulated vacuum pressure. For some films, magnetron sputtering using a gold sputter target was operated simultaneously during MAPLE, while for others sputtering was operated after the MAPLE deposition was complete.

Sample ID #	Substrate	MAPLE processing parameters	Process sequence
MM-1	silicon wafer	target: toluene + ~0.08wt.% cnp, 700 mJ, 1 Hz, 100C substrate temperature, 100V substrate bias	Prior to deposition: plasma etch 900V substrate bias in Ar 20-100 mTorr@100sccm for 2 hrs; co-deposit 60 min with magnetron (Au target, 40W) and laser, 20 mtorr Ar @ 100 sccm
MM-2	440C steel	target: toluene + ~0.08wt.% cnp, 700 mJ, 1 Hz, 100C substrate temperature, 100V substrate bias	Prior to deposition: plasma etch 900V substrate bias in Ar 20-100 mTorr@100sccm for at least 5 min; co-deposit 60 min with magnetron (Au target, 40W) and laser, 20 mtorr Ar @ 100 sccm
MM-3	440C steel	target: toluene + ~0.08wt.% cnp, 700 mJ, 1 Hz, 100C substrate temperature, 100V substrate bias	Steel surface scratched with 250 grit sand paper prior to putting in chamber; prior to deposition: plasma etch 900V substrate bias in Ar 20-100 mTorr@100sccm for at least 5 min; co-deposit 60 min with magnetron (Au target, 40W) and laser, 20 mtorr Ar @ 100 sccm
MM-5	440C steel	target: toluene + ~0.08wt.% cnp, 700 mJ, 1 Hz, 100C substrate temperature, 100V substrate bias	Prior to deposition: plasma etch 800V substrate bias in Ar 100 mTorr@100sccm for 20 min; co-deposit 60 min with magnetron (Au target, 60W) and laser, 20 mtorr O ₂ @ 100 sccm
MM-6	440C steel	target: toluene + ~0.08wt.% cnp, 800 mJ, 1 Hz, 100C substrate temperature, 100V substrate bias	Prior to deposition: plasma etch 800V substrate bias in Ar 100 mTorr@100sccm for 20 min; turn on magnetron for 3 min; then co-deposit 15 min with magnetron (Au target, 60W) and laser, 20 mtorr O ₂ @ 100 sccm
MM-7	440C steel	target: toluene + ~0.08wt.% cnp, 800 mJ, 1 Hz, 100C substrate temperature, 100V substrate bias	Steel surface scratched with 600 grit sand paper prior to putting in chamber; prior to deposition: plasma etch 800V substrate bias in Ar 100 mTorr@100sccm for 20 min; turn on magnetron for 3 min; then co-deposit 15 min with magnetron (Au target, 60W) and laser, 20 mtorr O ₂ @ 100 sccm
MM-8	440C steel	target: toluene + ~0.08wt.% cnp, 700 mJ, 1 Hz, 100C substrate temperature	turn on magnetron (Au target, 30W) 15mTorr Ar @ 25 sccm; after 1 min turn on laser; co-deposit for 60 min; turn off magnetron; deposit using MAPLE only for 1 minute; shut off laser
MM-9	440C steel	target: toluene + ~0.08wt.% cnp, 800 mJ, 1 Hz, 100C substrate temperature	turn on magnetron (Au target, 30W) 15mTorr Ar @ 12.5 sccm and O ₂ at 12.5 sccm; after 1 min turn on laser; co-deposit for 60 min
MM-18	440C steel	target: toluene + ~0.08wt.% cnp, 700 mJ, 1 Hz, 20C substrate temperature, 150V substrate bias	pre-clean Au target in oxygen then argon, plasma etch 10 min @ 800V in Ar @ 100 sccm, 35 mTorr; turn on magnetron Cr target 50W in Ar 15mTorr @ 100 sccm for 5min to sputter pure chromium; sputter Cr and Au for 1 min while decreasing Cr power to 0W and increasing Au to 30W; sputter Au for 1 min; turn on laser and co-deposit for 45 min @ 15mTorr @ 75 sccm O ₂ and 25 sccm Ar; turn off mag and run MAPLE only for 15 min in Ar at 15 mTorr, 100 sccm
MM-19	440C steel	target: toluene, 700 mJ, 1 Hz, 20C substrate temperature, 150V substrate bias	pre-clean Au target in oxygen then argon, plasma etch 10 min @ 800V in Ar @ 100 sccm, 45 mTorr; turn on magnetron Cr target 50W in Ar 15mTorr @ 100 sccm for 5min to sputter pure chromium; sputter Cr and Au for 1 min while decreasing Cr power to 0W and increasing Au to 30W; sputter Au for 1 min; turn on laser and co-deposit for 45 min @ 15mTorr @ 75 sccm O ₂ and 25 sccm Ar; turn off mag and run MAPLE only for 15 min in Ar at 15 mTorr, 100 sccm
MM-20	silicon wafer	target: toluene + ~0.08wt.% cnp, 700 mJ, 1 Hz, 20C substrate temperature	pre-clean Au target in oxygen then argon, plasma etch 15 min @ 800V in Ar @ 100 sccm, 100 mTorr; turn on magnetron Cr target 50W in Ar 15mTorr @ 100 sccm for 5min to sputter pure chromium; sputter Cr and Au for 1 min while decreasing Cr power to 0W and increasing Au to 30W; turn on laser and co-deposit for 45 min @ 15mTorr @ 90 sccm O ₂ and 10 sccm Ar; turn off mag and run MAPLE only for 15 min in Ar at 15 mTorr, 100 sccm
MM-21	silicon wafer	target: toluene + ~0.08wt.% cnp, 700 mJ, 1 Hz, 20C substrate temperature	pre-clean Au target in oxygen then argon, plasma etch 15 min @ 800V in Ar @ 100 sccm, 100 mTorr; turn on magnetron Cr target 50W in Ar 15mTorr @ 100 sccm for 5min to sputter pure chromium; sputter Cr and Au for 1 min while decreasing Cr power to 0W and increasing Au to 30W; turn on laser and co-deposit for 45 min @ 15mTorr @ 20 sccm O ₂ and 80 sccm Ar; turn off mag and run MAPLE only for 15 min in Ar at 15 mTorr, 100 sccm
MM-22	silicon wafer	target: toluene + ~0.08wt.% cnp, 700 mJ, 1 Hz, 20C substrate temperature	pre-clean Au target in oxygen then argon, plasma etch 10 min @ 800V in Ar @ 100 sccm, 80 mTorr; turn on magnetron Cr target 50W in Ar 15mTorr @ 100 sccm for 5min to sputter pure chromium; sputter Cr and Au for 1 min while decreasing Cr power to 0W and increasing Au to 30W; deposit Au for 5min at 30W; turn off magnetron; turn on laser for 1 hr in vacuum; turn off laser, sputter gold for 45min at 30W in Ar at 15 mTorr, 100 sccm
MM-23	silicon wafer	target: toluene, 700 mJ, 1 Hz, 20C substrate temperature	pre-clean Au target in oxygen then argon, plasma etch 10 min @ 800V in Ar @ 100 sccm, 80 mTorr; turn on magnetron Cr target 50W in Ar 15mTorr @ 100 sccm for 5min to sputter pure chromium; sputter Cr and Au for 1 min while decreasing Cr power to 0W and increasing Au to 30W; deposit Au for 5min at 30W; turn off magnetron; turn on laser for 1 hr in vacuum; turn off laser, sputter gold for 45min at 30W in Ar at 15 mTorr, 100 sccm

Table 4.2.2: List of thin films deposited using MAPLE and magnetron sputtering

4.3 Film formation studies using EQP

Ion and neutral mass scans were conducted with a Hiden electrostatic quadrupole plasma (EQP) analyzer. Spectra were monitored for a number of conditions, which are listed in Table 4.3.1. Energy scans were performed for the primary species detected in the processes, which were generally neutral or singly ionized toluene, Ar, O₂, and O. Mass scans were subsequently performed at the most probable kinetic energy of the desired species measured with the analyzer as determined for each new condition. Since the incident laser was pulsed, the evolution of species from the target exhibited a strong time dependence on the microsecond scale. To account for this time dependence, a long dwell time (200 ms) for acquisition of spectra was selected. Multiple spectra were obtained at each condition and the results were averaged.

Test condition

no MAPLE target, vacuum, magnetron off, neutrals
no MAPLE target, Ar 20mTorr@100sccm, magnetron off, neutrals
no MAPLE target, Ar 20mTorr@100sccm, magnetron on, 40W, Au target, neutrals
no MAPLE target, Ar 20mTorr@100sccm, magnetron on, 40W, Au target, ions
no MAPLE target, 15mTorr, Ar@12.5sccm, O2@12.5 sccm, magnetron off, neutrals
no MAPLE target, 15mTorr, Ar@12.5sccm, O2@12.5 sccm, magnetron on, 30W, Au target, neutrals
no MAPLE target, 15mTorr, Ar@12.5sccm, O2@12.5 sccm, magnetron on, 30W, Au target, ions
no MAPLE target, O2 20mTorr@100sccm, magnetron off, neutrals
no MAPLE target, O2 20mTorr@100sccm, magnetron on, 60W, Au target, neutrals
no MAPLE target, O2 20mTorr@100sccm, magnetron on, 60W, Au target, ions
no MAPLE target, vacuum, magnetron off, cold trap filled with liq. N2, neutrals
toluene+cnp MAPLE target, laser off, vacuum, magnetron off, neutrals
toluene+cnp MAPLE target, laser on 700mJ @ 1Hz, vacuum, magnetron off, neutrals
toluene+cnp MAPLE target, laser on 700mJ @ 1Hz, vacuum, magnetron off, ions
toluene+cnp MAPLE target, laser on 700mJ @ 1Hz, Ar 20mTorr@100sccm, magnetron off, neutrals
toluene+cnp MAPLE target, laser on 700mJ @ 1Hz, 15mTorr, Ar@12.5sccm, O2@12.5 sccm, magnetron off, neutrals
toluene+cnp MAPLE target, laser on 700mJ @ 1Hz, O2 20mTorr@100sccm, magnetron off, neutrals
toluene+cnp MAPLE target, laser on 700mJ @ 1Hz, O2 20mTorr@100sccm, magnetron on, 60W, Au target, neutrals
toluene+cnp MAPLE target, laser on 700mJ @ 1Hz, 15mTorr, Ar@12.5sccm, O2@12.5 sccm, magnetron on, 30W, Au target, neutrals
toluene+cnp MAPLE target, laser on 700mJ @ 1Hz, 15mTorr, Ar@12.5sccm, O2@12.5 sccm, magnetron on, 30W, Au target, ions
toluene+cnp MAPLE target, laser on 700mJ @ 1Hz, Ar 20mTorr@100sccm, magnetron on, 40W, Au target, neutrals
toluene+cnp MAPLE target, laser on 700mJ @ 1Hz, Ar 20mTorr@100sccm, magnetron on, 40W, Au target, ions
toluene+cnp MAPLE target, laser on 700mJ @ 1Hz, 20mTorr, various Ar/O2 ratios, magnetron on, 30W, Au target, ions
toluene+cnp MAPLE target, laser on 700mJ @ 1Hz, 20mTorr, various Ar/O2 ratios, magnetron on, 30W, Au target, neutrals
toluene+cnp MAPLE target, laser on 700mJ @ 1Hz, magnetron on, 30W, Au target, monitor 20/80, 50/50, 80/20, 0/100, 100/0, 60/40, 40/60 O2/Ar ratios over 12 minutes starting from clean targets

Table 4.3.1: List of experimental conditions within the MAPLE deposition chamber evaluated using EQP

In order to compare the effects of oxygen to argon gas mixtures and other experimental conditions it was necessary to measure the concentration of species detected by the EQP analyzer. This was accomplished using trapezoidal integration, with the assumption that the integrated area under a peak (or series of peaks) was proportional to the concentration of the species present within the processing system.

4.4 Experimental details for tribological testing of carbon nanopearl films

4.4.1 Fretting wear experiments

Carbon nanopearls were investigated in fretting wear tribological contacts with an ellipsoid-on-flat contact surface geometry. For these tests, CNPs were dispersed using the methanol drop-cast method onto a 12.7 mm diameter M50 steel disk, and the M50 steel ellipsoid was placed onto the surface of the disk as shown in Figure 4.4.1. During the test a normal load of 5N was applied, resulting in a maximum Hertzian contact stress of approximately 400 MPa, with a stroke length of 200 μm and a frequency of 2 Hz. Tests were conducted in both humid lab air and dry nitrogen environments up to 1,000 cycles. Fretting processes were monitored in real time by recording the hysteresis loop of the friction force versus actual contact displacement, using a laser positioning system and a piezoelectric transducer [76]. The frictional hysteresis was used as a process indicator to verify that the system was operating in the gross slip regime, characterized by quasi-rectangular shaped hysteresis loops [76]. Tests were also conducted under identical conditions without CNP material on the sample surfaces as a control. Friction coefficient vs. number of fretting wear cycles was recorded for both the CNP sample and the control. SEM analyses of wear tracks in both ball-on-disk and fretting wear tests was used to investigate wear debris and contact areas.

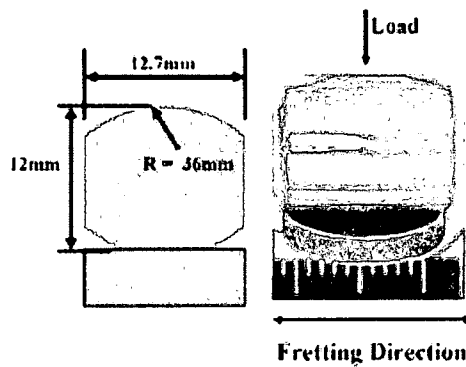


Figure 4.4.1: Contact geometry of ellipsoid sample used in fretting wear test

4.4.2 Ball-on-disk sliding experiments

Ball-on-disk tribometer tests of CNP films and methanol drop cast graphite powder (natural, briquetting grade, 200 mesh, 99.9995% metals basis) were performed in both humid air (40% relative humidity) and dry air (0% RH) using a 25g load (resulting in a Hertzian contact pressure of approximately 430 MPa) at a sliding rate of 0.03-0.05 m/s with the disk rotating at 100 rpm. The 6.35 mm diameter balls were made of 440C stainless ball bearing steel. All tests were repeated three times with the same conditions. Figure 4.4.2 shows the tribometer used for the experiments.

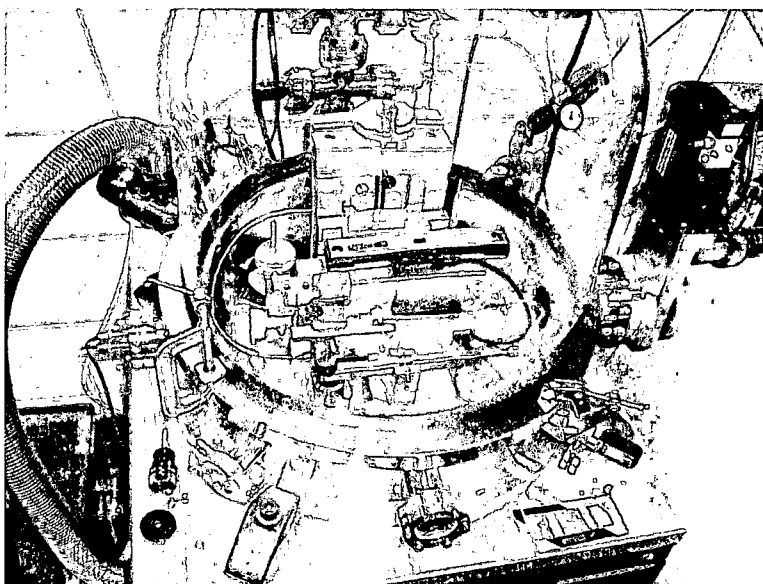


Figure 4.4.2: Tribometer

4.5 Characterization of carbon nanopearl film morphology, structure, and chemistry

Carbon nanopearl films were characterized using optical microscopy, SEM, Raman spectroscopy, XRD, and XPS. Wear surfaces of tribometer specimens were examined in addition to as-deposited films. Secondary electron SEM imaging was performed using a FEI Quanta ESEM I microscope equipped with an energy dispersive spectrometer (EDS) system capable of operating in 2D mapping mode (Figure 4.5.1). Raman spectra were collected using a Raman microscope equipped with an air cooled 514 nm argon ion laser with maximum output power 20 mW (Figure 4.5.2). At each spot of interest, four scans were accumulated from 100 to 3200 cm^{-1} during which the laser was operated at some fraction of the maximum output power, typically 10 or 20%, for 10 seconds per scan. XRD spectra were collected on as-received CNPs and graphite powder (natural, briquetting grade, 200

mesh, 99.9995% metals basis) using a Rigaku-D/max-1B X-ray diffractometer with a Cu K α X-ray source operating in coupled scan mode (Figure 4.5.3). XPS measurements were performed using a Surface Science Instruments (SSI) M-probe XPS equipped with an Al K α X-ray source (Figure 4.5.4). The XPS analysis chamber containing the substrates was maintained at a pressure of about 4 Pa, and samples were sputtered in argon for 30 seconds prior to the measurements to remove any possible surface contamination.

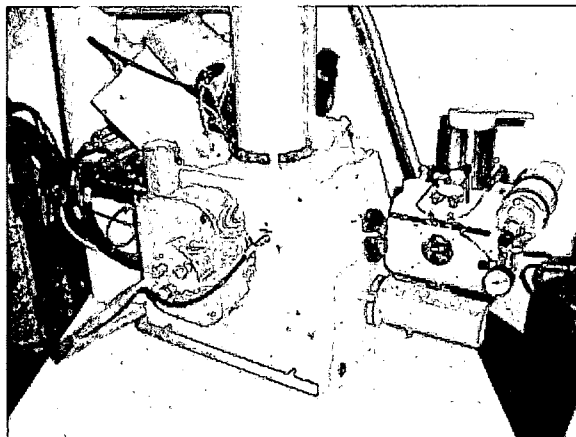


Figure 4.5.1: SEM/EDS system

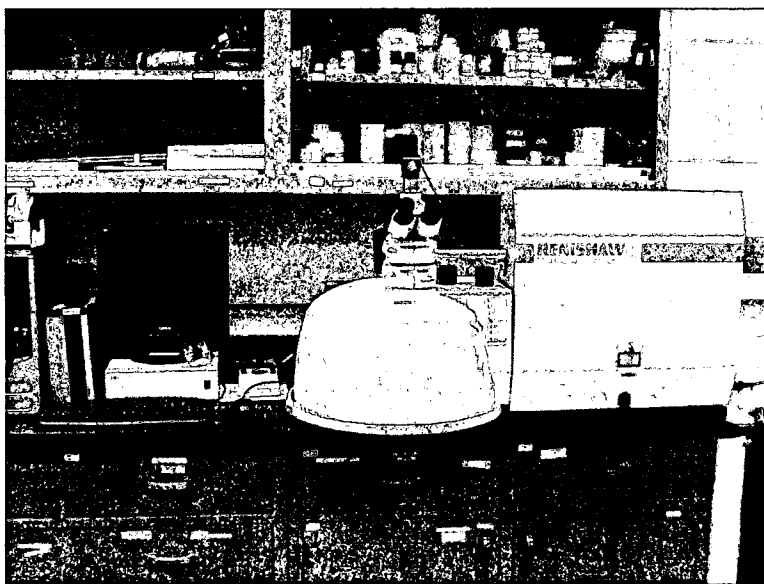


Figure 4.5.2: Raman microscope

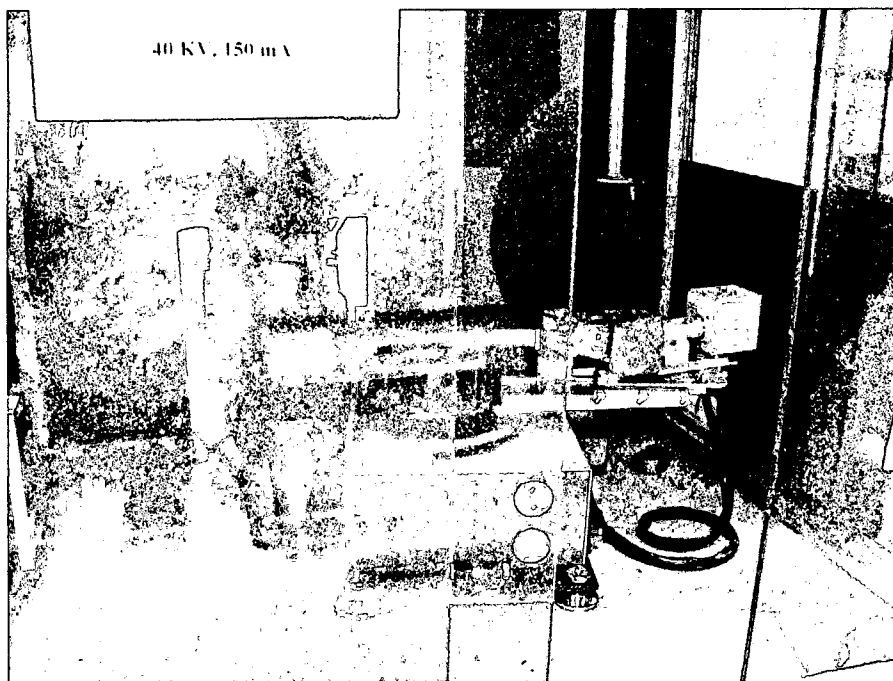


Figure 4.5.3: X-Ray diffractometer system

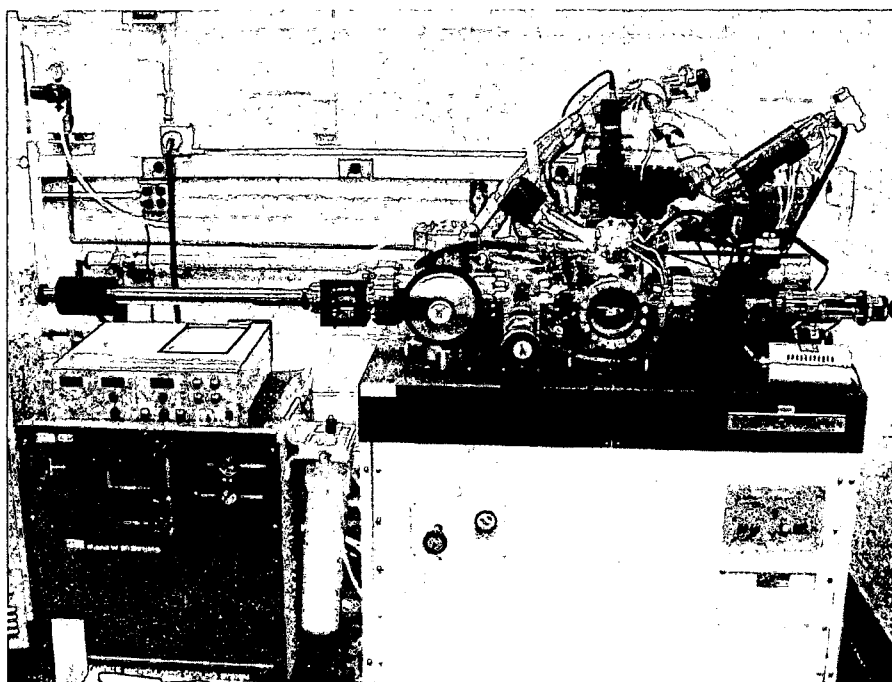


Figure 4.5.4: XPS system

Absorbance of CNPs dissolved in methanol was measured at 248 nm (wavelength of the KrF excimer laser used for the MAPLE experiments) using a UV-vis spectrometer. For this measurement, the absorbance of neat methanol was also measured by the spectrometer and subtracted from the CNP-methanol spectrum.

5. RESULTS AND DISCUSSION

5.1 Process development and film formation mechanisms for carbon nanopearls

In this section, development of processes for depositing CNP films using drop casting, MAPLE, and MAPLE combined with magnetron sputtering are described, as well as mechanisms for formation of CNP films. There are many parameters in the MAPLE process which control the properties of deposited films which have not been explored in the literature to date. MAPLE combined with magnetron sputtering is a novel technique for synthesis of nanostructured hybrid films, and as such it is important to explore film formation mechanisms during this dual process.

5.1.1 Drop cast process for carbon nanopearl films

As discussed in Chapter 4, CNP films were prepared by ultrasonically agitating CNP/methanol mixtures in an attempt to more effectively dissolve the CNPs prior to applying drops onto silicon wafer substrates. Ultrasonic agitation appeared to effectively disperse the CNP material, but larger agglomerates began to form quickly after the mixture was removed from the sonicator. As the methanol evaporated, the surface of the specimen did not get uniformly covered with CNP material.

Agglomerates of CNPs formed covering some areas of the surface while others areas

contained no CNP material that was evident visually (Figure 5.1.1). Deposition of CNP films using this drop-casting method resulted in a fairly wide distribution between replicate substrates in the surface area fraction covered with CNPs with a maximum of approximately 50% coverage. Ideally, CNP films deposited for the purpose of investigating the tribological properties of CNPs would have a high and uniform surface density with good adhesion, which could allow the CNPs to remain anchored in place within friction contacts. Methods for depositing more homogenous and well adhering films for tribological studies using MAPLE and MAPLE with magnetron sputtering are explored in the following sections.

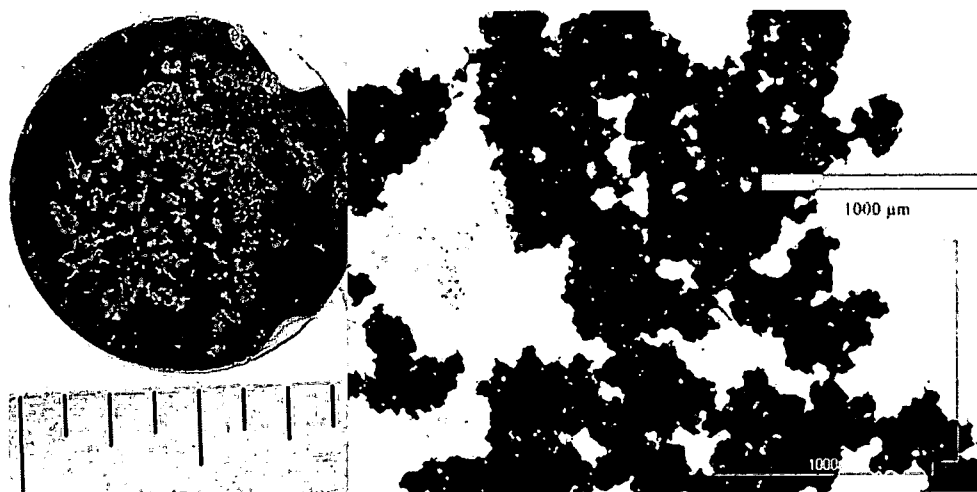


Figure 5.1.1: Methanol drop-cast CNPs on silicon

5.1.2 MAPLE processing studies of carbon nanopearl films

In this section, the influence of laser repetition rate, laser energy, background pressure, substrate temperature, and matrix solvent on the morphology of carbon

nanopearl films deposited onto silicon substrates using MAPLE is discussed. The motivation for this work was to obtain an optimal set of parameters for depositing homogenous films while maximizing the amount of material deposited.

5.1.2.1 Influence of laser repetition rate

The effect of laser repetition rate on MAPLE sample surface morphology was evaluated by comparing films produced at 1, 3, or 5 Hz laser repetition rates. For these experiments, 0.08 wt. % carbon nanopearls in acetone, 500 mJ laser energy, 7 minutes deposition time, ambient laboratory temperature (20°C), and 2.67 Pa pressure in argon were used. The area densities of the 1 Hz and 3 Hz samples are the same, however the morphology is different. The 1 Hz sample is more dispersed whereas the 3 Hz sample has more of the material clustered at droplets rather than spread out in smaller clusters. This may be because smaller clusters of CNPs reached the surface via evaporation at 1 Hz, whereas at 3 Hz most of the CNPs were transported by liquid droplets and concentrated in the areas where the droplets hit the surface. The number and size of droplets and area fraction covered with nanopearls were much higher at 5 Hz compared to 3 and 1 Hz (Figure 5.1.2). This result is in agreement with Sellenger et al., who showed that increasing laser fluence may increase the number density and size of surface features of deposited material [77].

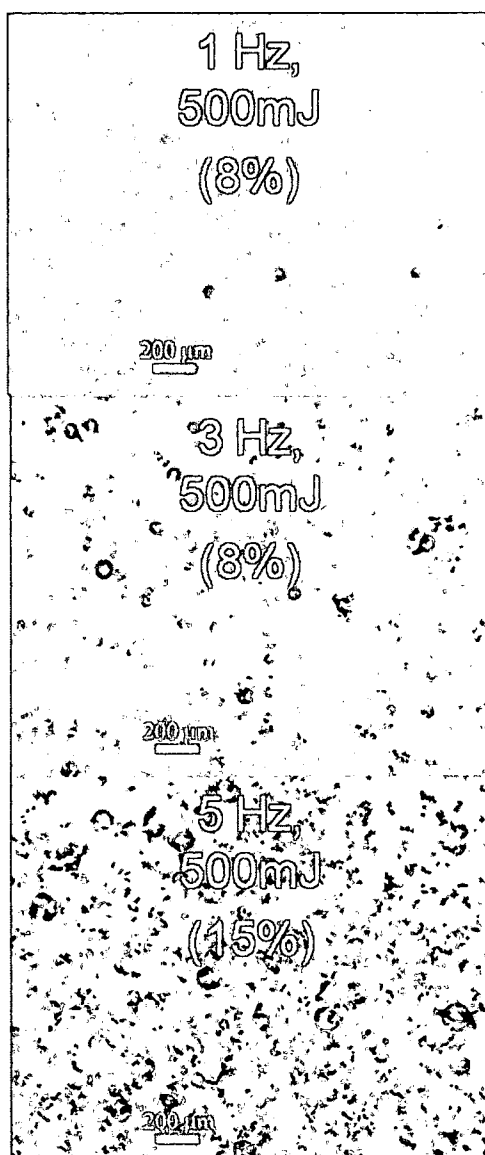


Figure 5.1.2: MAPLE samples synthesized at several laser repetition rates. Area fraction covered with carbon nanopearls listed in parentheses.

Laser pulses striking the target cause a layer of solvent on the outer surface to melt, and some of the liquid at the surface is vaporized. CNP material is carried to the substrate surface by solvent vapor and by liquid droplets ablated from the target surface. Since the target is maintained at liquid nitrogen temperature, well below the melting temperature of the solvent, the liquefied layer refreezes in the time between

laser pulses. At higher repetition rates, the target surface probably does not have time to completely refreeze before the next laser pulse strikes the target, leading to more and larger droplets transferred to the sample surface. Also at higher repetition rates, more of the target material is vaporized, so the overall result is more material is deposited on the substrate surface as the laser repetition rate is increased. These scenarios are depicted schematically in Figure 5.1.3

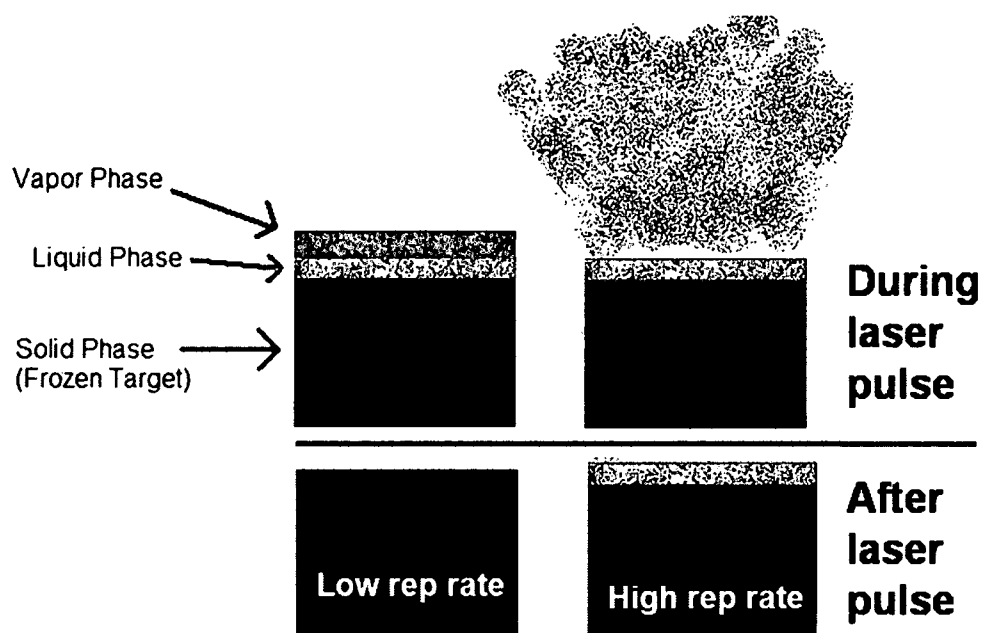


Figure 5.1.3: Schematic illustration of the effect of laser repetition rate on frozen MAPLE targets

5.1.2.2 Influence of laser energy

The effect of laser energy on MAPLE sample surface morphology was evaluated by comparing films produced at 500, 600, or 700 mJ laser pulse energy. For these experiments, 3 Hz laser repetition rate, 0.08 wt. % carbon nanopearls in acetone, 7

minutes deposition time, ambient laboratory temperature (20°C), and 2.67 Pa pressure in argon were used. The area fraction increased with increasing laser energy. Also, the nanopearl dispersion (smaller agglomerate mean size) was greater at 700 mJ compared to 500 and 600 mJ (Figure 5.1.4).

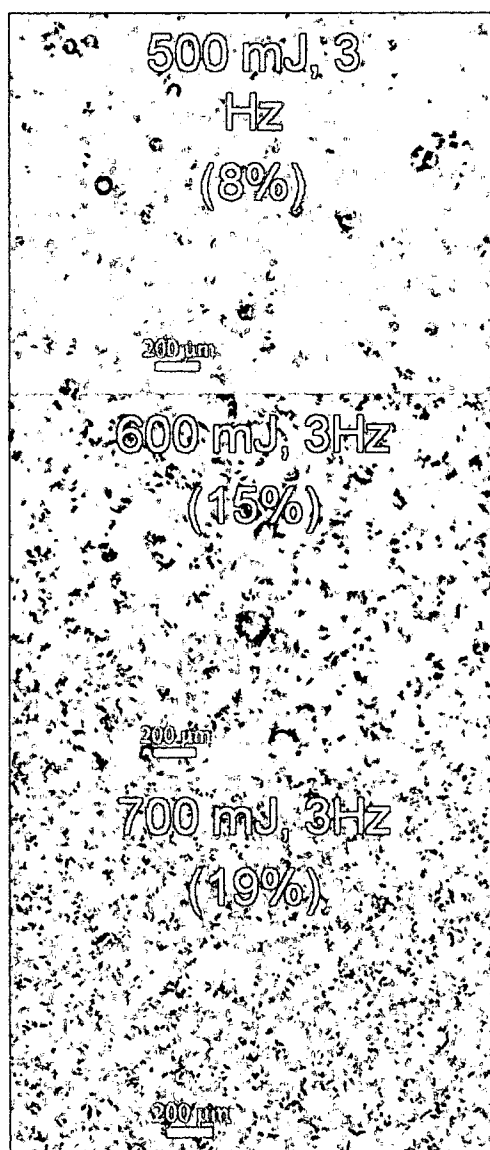


Figure 5.1.4: MAPLE samples synthesized at several laser energies. Area fraction covered with carbon nanopearls listed in parentheses.

At higher laser energies, more of the frozen target is converted to vapor per pulse, while at lower laser energies the target solvent material is converted to liquid (larger droplet sizes) so that most of the material on the substrate surface has been deposited by liquid droplets. However, higher laser energy with higher rep rates may cause even more droplets because the target does not have time to refreeze in between pulses. The optimal energy for depositing carbon nanopearls is 700mJ because of the higher deposition rate and greater dispersion.

5.1.2.3 Influence of background pressure

The effect of background pressure on MAPLE sample surface morphology was evaluated by comparing films produced at unregulated vacuum pressure, 2.67 Pa in argon, or 13.33 Pa in argon. For these experiments, the following settings were used: 3 Hz laser repetition rate, 500 mJ laser energy, 0.08 wt. % carbon nanopearls in acetone, 7 minutes deposition time, and ambient laboratory temperature (20°C). Depositions that occurred under vacuum pressure appeared to be the most disperse and had the highest area fraction of nanopearls on the surface (Figure 5.1.5).

At higher pressures there is less driving force for liquid to convert to vapor phase, and it can be seen from examining Figure 5.1.5 that the nanopearls are concentrated at larger droplet sites at the higher pressures. At the same time, at the lowest pressure there are droplet sites but also many smaller clusters of CNPs that were transported to the surface via vapor and much smaller liquid droplets. For using MAPLE in

conjunction with magnetron sputtering, it is necessary to use background gases and regulate the vacuum chamber pressure in order to generate plasma at the sputtering source. Therefore, use of argon at 2.67 Pa would be optimal for MAPLE and magnetron sputtering.

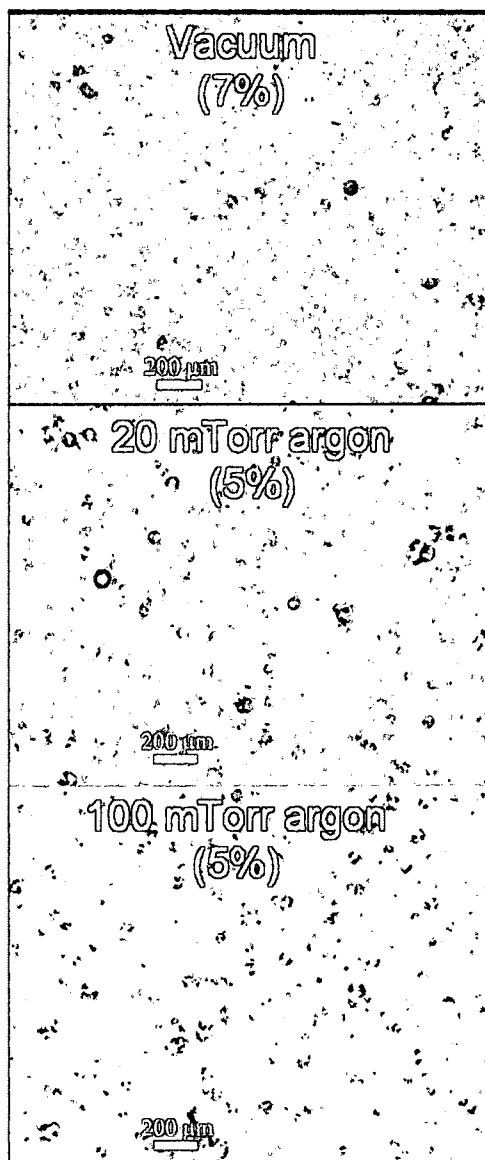


Figure 5.1.5: MAPLE samples synthesized at several background pressures. Pressure for sample deposited in vacuum was unregulated. Area fraction covered with carbon nanopearls listed in parentheses.

5.1.2.4 Influence of substrate temperature

The effect of substrate temperature on MAPLE sample surface morphology was evaluated by comparing films produced at ambient temperature (20°C), 100°C and 200°C. For these experiments films were deposited at 3 Hz laser repetition rate, 500 mJ laser energy, 0.08 wt. % carbon nanopearls in acetone, 7 minutes deposition time, and unregulated vacuum pressure or 2.67 Pa background pressure in argon. Optical micrographs of the deposited films are shown in Figure 5.1.6. At vacuum pressure, the largest area fraction of material is deposited at ambient temperature and decreases as the temperature increases, while the droplet size decreases with increasing temperature, with no evidence of droplets at 200 °C. At 2.67 Pa pressure, the area fraction of deposited material increases slightly between 20°C and 100°C and decreases between 100°C and 200°C. The optimal temperature for MAPLE deposition in argon background gas at 2.67 Pa pressure (which enables simultaneous magnetron sputtering) is 100°C.

There appears to be a correlation between temperature and pressure in determining the morphology of the deposited films. However, at the higher temperature of 200°C the morphology at both pressures is the same with no evidence of liquid droplets and with much smaller nanopearl clusters. A good compromise for deposition is 100 °C because the droplets are much smaller but there is still a good area fraction of material deposited.



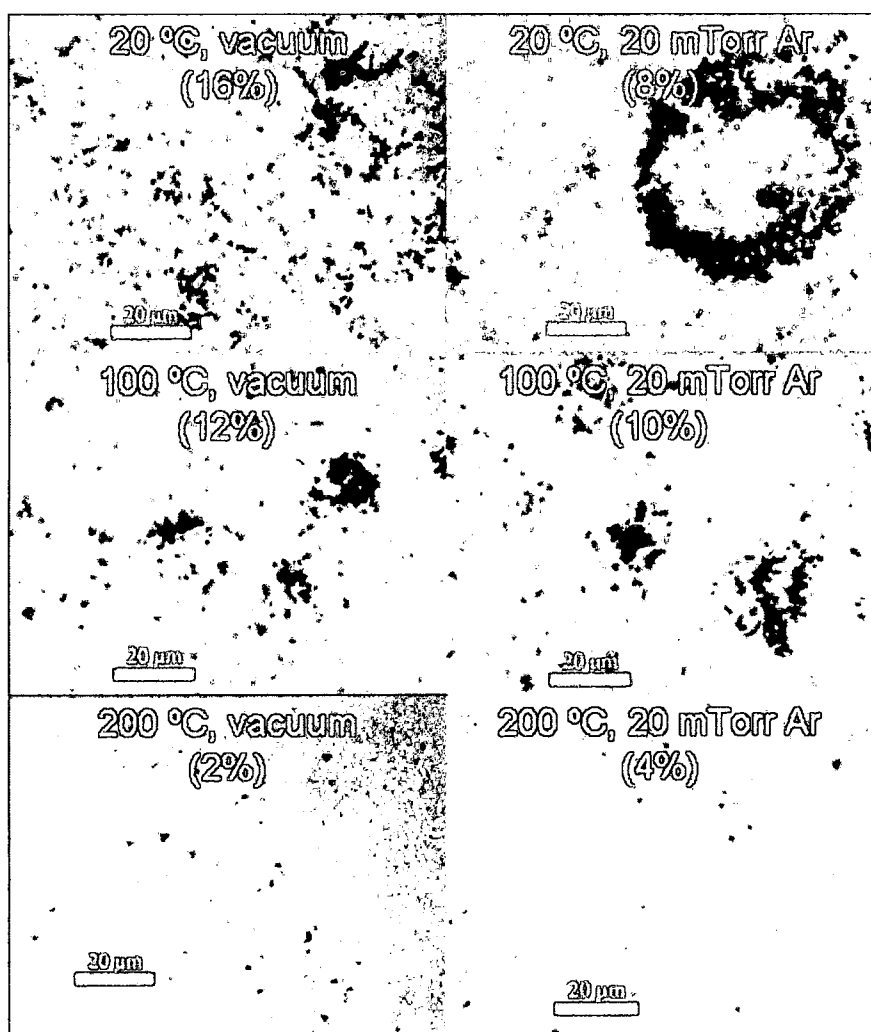


Figure 5.1.6: MAPLE samples synthesized at several background pressures and temperatures. Area fraction covered with carbon nanopearls listed in parentheses.

5.1.2.5 Influence of matrix solvent

Solvents were selected for evaluation in this study based on the following criteria: vapor pressure, melting temperature, absorbance at 248 nm, compatibility with vacuum systems, and toxicity. Target solutions containing 0.08 wt. % carbon nanopearls were made using acetone, DMSO, DMF, toluene, methanol, and ethyl acetate. Thin films were deposited onto silicon wafers using the MAPLE process

with the following deposition parameters: 3 Hz laser repetition rate, 500 mJ laser energy, 7 minutes deposition time, ambient laboratory temperature (20°C), and unregulated vacuum pressure. CNPs were deposited on the surface of all of the silicon wafer samples with varying surface coverage and morphology depending on the target solvent (Figure 5.1.7). The toluene sample had the densest surface coverage of all the solvents, with an area fraction of 26%. Circular features with high amounts of material concentrated at the edges were also present on the surfaces of the samples. The circles appear to be regions where liquid droplets hit the surface and evaporated, leaving behind nanoparticle material around the edges (Figure 5.1.7). These were minimized for DMSO and methanol.

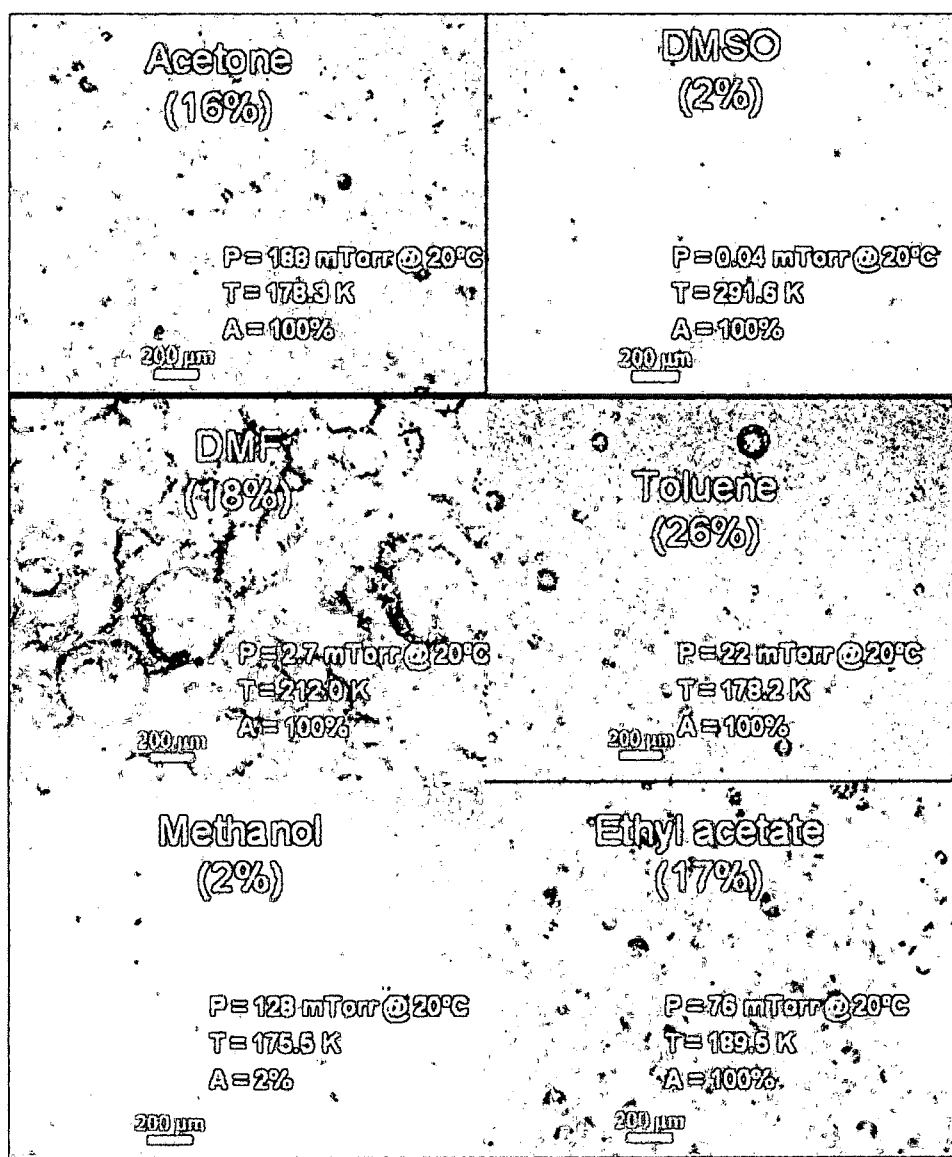


Figure 5.1.7: MAPLE samples synthesized using various matrix solvents. Area fraction covered with carbon nanopearls listed in parentheses. Vapor pressure (P), Melting Temperature (T), and Absorbance at 248 nm (A) for each matrix solvent are listed.

Morphology of films deposited by MAPLE is influenced by a number of factors including background pressure, solvent freezing and vaporization temperature, latent heat of freezing and vaporization of the solvent, heat capacity of the liquid and solid solvent phases, and absorbance of laser energy by the frozen solvent. There exists a

set of such parameters for maximizing the amount of material deposited, though quantitative study of the effect of these parameters was beyond the scope of the present research. However, some trends were observed. DMSO has a high (100%) absorbance at 248 nm but the amount of material deposited by MAPLE was low (2% surface coverage), probably due to the very low vapor pressure of DMSO. The amount of CNP material deposited using methanol as a matrix solvent was also low (2% surface coverage) probably because the absorbance of methanol at 248 nm is 2%. The maximum amount of material was deposited using toluene as the matrix solvent. Toluene possesses several characteristics favorable for deposition, including high absorbance, low melting temperature, and medium-range vapor pressure.

5.1.2.6 MAPLE target study

A MAPLE experiment was performed using a target solution of 0.08 wt. % carbon nanopearls in toluene to determine the ablation rate of frozen target material. A control experiment using a pure toluene target was also performed. The deposition conditions of these experiments were as follows: 700 mJ, 1 Hz, unregulated vacuum pressure, 20°C substrate temperature, and 1.5 hour deposition time. Examination of the frozen targets visually after the MAPLE experiments (Figure 5.1.8) showed that the amount of frozen material removed appeared to be roughly equal. The voided regions of the targets were refilled with toluene and refrozen using a pipette dropper with a volumetric scale. For both targets, the amount of liquid toluene necessary to refill the voided volume was 1 mL, meaning that the ablation rate was the same

whether or not the target was loaded with CNPs. The amount of target material removed per laser pulse was estimated to be 0.19 mg for both 0.08 wt. % carbon nanopearls in toluene and toluene MAPLE targets. This estimate was made by computing the density of frozen toluene (approximately 1.03 g/mL) and multiplied by the total volume of material removed (1 mL) and divided by the total number of pulses (5400).

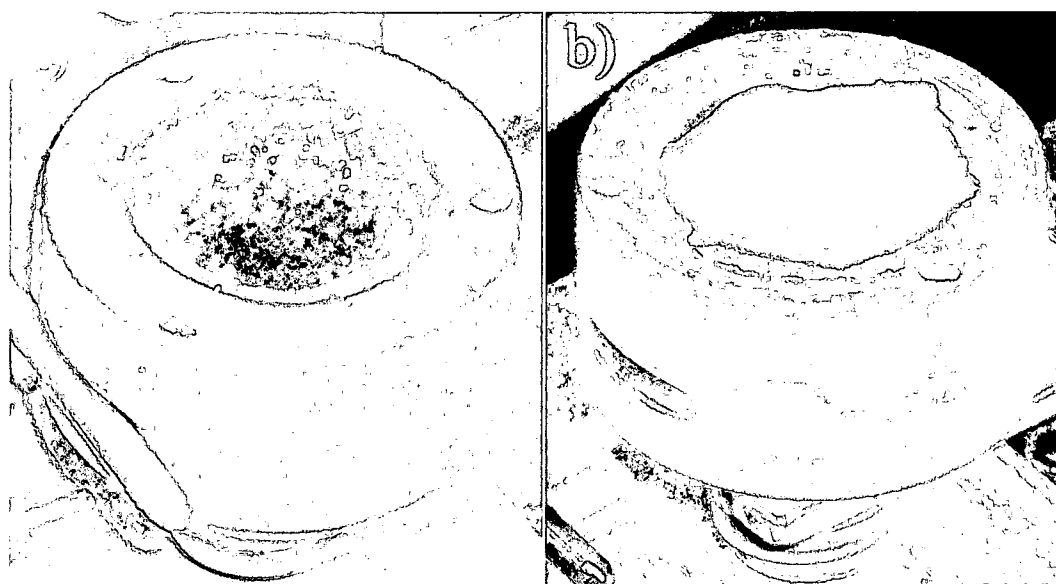


Figure 5.1.8: Frozen MAPLE targets after 1.5 hours of laser ablation: a) 0.08 wt. % carbon nanopearls in toluene, b) toluene. Diameter of target reservoir = 25.4 mm.

The absorbance at 248 nm of a CNP-methanol mixture was measured using a UV-vis spectrometer. The absorbance of neat methanol was also measured by the spectrometer and subtracted from the CNP-methanol spectrum. The absorbance of the CNP-methanol mixture at 248 nm was 3.2, corresponding to a transmittance of 0.06%. However, most of the energy of laser pulses striking CNP-loaded MAPLE targets is likely absorbed by the solvent because the volume fraction of CNPs in the

MAPLE targets is very low (approximately 0.0009). In addition toluene, the matrix solvent used for most of the MAPLE depositions, has a transmittance of 0 at 248 nm [72].

5.1.2.7 Summary of carbon nanopearl deposition studies using MAPLE

The morphology of carbon nanopearl films deposited using a MAPLE system equipped with a 248 nm KrF excimer laser source was found to be influenced by multiple factors, including composition of the matrix solvent, laser energy and repetition rate, background pressure, and substrate temperature. At ambient laboratory temperatures, the morphology of deposited films was characterized by highly concentrated areas of carbon nanopearls in the shape of hollow rings, caused by impingement of liquid droplets of the solvent/CNP suspension on the substrate surface followed by evaporation of the solvent. As the substrate temperature was increased, the size of the liquid droplets reaching the substrate surface decreased; however, the amount of material deposited via evaporation also decreased. The optimal temperature for minimizing droplets and maximizing amount of material deposited was around 100°C. The largest amount of material was deposited at high laser energy and repetition rates, and low (vacuum) pressures. However, there appeared to be correlations affecting the film morphology between the temperature and pressure, and between the laser energy and laser repetition rate. The best parameters for depositing disperse, droplet-free films of carbon nanopearls were found as follows: toluene matrix, 700 mJ, 1 Hz, 100°C substrate temperature, and

unregulated vacuum pressure. However, disperse and droplet-free films can also be deposited in argon at 2.67 Pa, which is advantageous for process hybridization with magnetron sputtering to produce nanostructured hybrid materials.

5.1.3 Studies of hybrid process combining MAPLE deposition of CNPs with magnetron sputtering of gold

The MAPLE-magnetron sputter hybrid process allows CNPs to be embedded into metal or ceramic matrices, leading to advanced tribological, mechanical, and physical properties. The main results of investigations of the MAPLE-magnetron sputter hybrid technique are described here. To the best knowledge of the author this is a pioneering investigation, as such hybrid process has not yet been described in the literature. Gold was selected for use as the matrix sputtering material, since it is an aerospace solid lubricant and its combination with carbon nanopearls could be of potential tribological interest, as discussed in section 2.2.5. For synthesizing nanostructured hybrid films, it is important to understand the plasma-chemical interactions that occur during combined MAPLE and sputtering processes, which are run at the same time within the deposition chamber to produce gold-CNP nanostructured hybrid films by embedding CNPs released from MAPLE target into metallic or ceramic sputtering material. During operation of this dual process, the potential exists for argon sputter plasmas to interact with hydrocarbon solvent vapors released by evaporation during laser pulsing of the frozen MAPLE target, which would result in deposition of undesired carbonaceous material on surfaces within the

deposition chamber, including the film substrate, the sputter targets, and the laser window. A potential countermeasure for this effect is the use of oxygen as a background sputter gas. In particular, neutral and ionized monatomic oxygen may react with volatile species to form CO and CO₂ instead of forming solid carbon deposits on surfaces within the deposition chamber. The focus of this section is to understand the effects of MAPLE and magnetron sputtering co-deposition on neutral and ionic species present during the process, to understand mechanisms for generation of carbon impurities in deposited films, and to propose methodologies for reducing the impact of these impurities.

5.1.3.1 Simultaneous MAPLE and magnetron sputtering: argon background

Ion mass counts were monitored during operation of MAPLE in vacuum environment (base pressure $\sim 10^{-6}$ Torr) with no sputtering using the EQP analyzer. The target material was 0.08% carbon nanopearls in toluene and the laser was operated at 700 mJ energy per pulse and a repetition rate of 1 Hz. The spectra contained zero counts across the mass spectrum and in particular no peaks were observed at 91 and 92 amu, the atomic masses corresponding to toluene ions.

Measurement of ionized species within the deposition chamber with argon background gas during simultaneous MAPLE and magnetron sputtering was performed with the EQP analyzer. During sputtering of gold in an argon background without MAPLE, argon ions were detected in abundance (Figure 5.1.9a). During

sputtering in argon with MAPLE, argon ions were still present but their flux to the probe was significantly reduced (Figure 5.1.9b). In addition, ionized toluene and fragments were present.

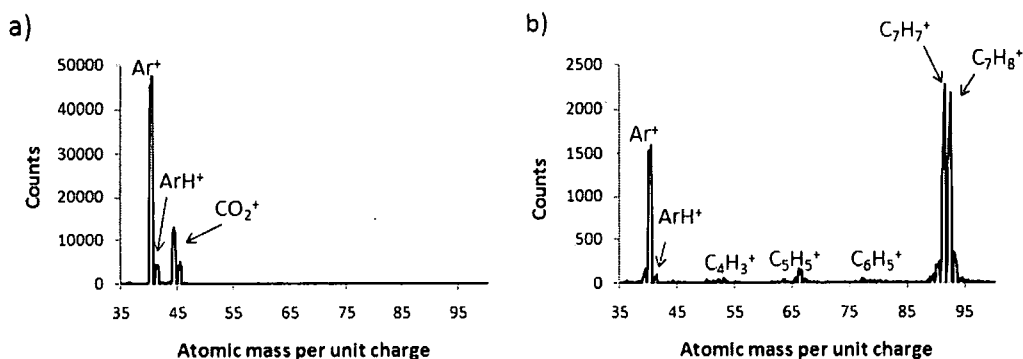


Figure 5.1.9: Counts vs. atomic mass per unit charge for: a) magnetron sputtering with gold target (30W output power in argon at 20mTorr @ 100sccm) and b) magnetron sputtering with gold target operating (30W output power in argon at 20mTorr @ 100sccm) and simultaneous MAPLE operation (target: 0.08% carbon nanopearls in toluene, 700 mJ, 1 Hz).

An explanation for the increased flux of ionized toluene species in the presence of argon during MAPLE is ionization of the toluene by electrons generated from the magnetron [78]. However, the drastic decrease in argon ions compared to sputtering without MAPLE would suggest that charge exchange mechanisms are dominant.

These proposed reactions (e.g. $\text{C}_7\text{H}_8 + \text{Ar}^+ \rightarrow \text{Ar} + \text{C}_7\text{H}_8^+$) have a very high rate on the order of $10^{-10} \text{ cm}^3/\text{sec}$ [79]. The ionized and neutral toluene species form a solid carbon film on surfaces within the vacuum chamber, including the sputter target, which was visibly coated after 1-3 minutes of MAPLE and sputtering in argon. Ultimately, the deposition rate of carbonaceous species on the gold target is faster than the sputter rate of the target itself, resulting in deposition of thin films with

nearly 0% gold content as the carbon on the target surface is continuously replenished by toluene species from the MAPLE target and the gold surface is never exposed to the incident ions for sputtering. These processes are summarized in a schematic drawing (Figure 5.1.10).

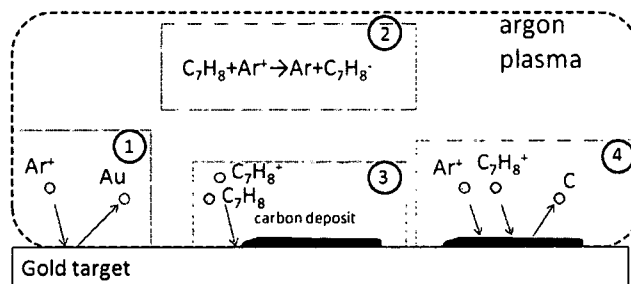


Figure 5.1.10: Mechanisms on a gold target surface in argon plasma during simultaneous MAPLE and magnetron sputtering: 1) Sputtering of Au atoms in Ar plasma; 2) Toluene/argon ion exchange; 3) Deposition of carbon onto gold target surface; 4) Sputtering of carbon from gold target surface

5.1.3.2 Simultaneous MAPLE and magnetron sputtering: oxygen background

The addition of oxygen to the process gas during magnetron-MAPLE co-deposition was investigated in an effort to eliminate carbon deposition on the sputtering target. Neutral and ionized atomic oxygen production in the magnetron glow discharge was characterized with the EQP analyzer, as shown in Figure 5.1.11. Removal of carbon from surfaces by reactive oxygen species is well documented and has been observed by previous researchers [80,81,82]. The efficacy with which the carbon was removed from surfaces within the chamber was observed qualitatively by depositing a carbon layer on the gold target by simultaneous MAPLE and magnetron sputtering in argon. After growth of a carbon layer on the gold target racetrack, the laser and magnetron

were shut off and the background gas was switched to oxygen. When the sputter process was reinitiated in the presence of oxygen, the surface of the gold target became visible, and the intensity of the plasma plume increased. In addition, the neutral mass spectrum was monitored during this process and the concentration of CO (28 amu) and CO₂ (44 amu) increased when the gas was switched to oxygen. The competition between carbon deposition and removal is illustrated schematically in Figure 5.1.12.

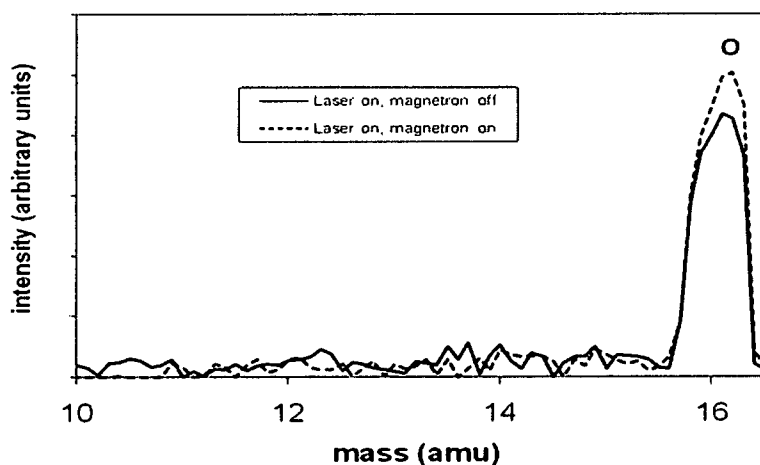


Figure 5.1.11: Mass spectra of neutral species in oxygen background (20 mTorr, 100 sccm) during MAPLE (target: 0.08% carbon nanopearls in toluene, 700 mJ, 1 Hz) with and without the magnetron operating (Au target, 60W power).

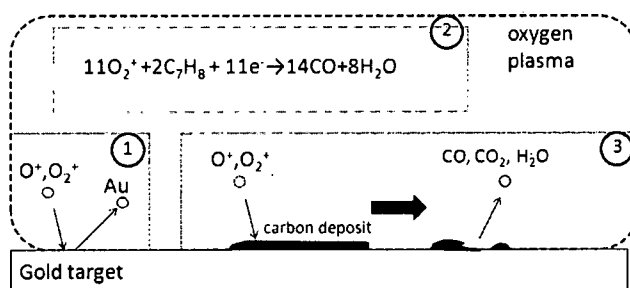


Figure 5.1.12: Mechanisms in oxygen plasma during simultaneous MAPLE and magnetron sputtering: 1) Sputtering of Au atoms in oxygen plasma; 2) Example reaction of toluene vapor with oxygen plasma; 3) Oxygen plasma reaction with carbon deposit on gold target surface

5.1.3.3 Simultaneous MAPLE and magnetron sputtering: argon and oxygen background

Simultaneous MAPLE and magnetron sputtering experiments were conducted using mixtures of oxygen and argon as the background gas to minimize carbon deposits on the target and substrate surfaces while maximizing the sputter rate of gold. Mass spectra of neutral and ionized species were collected from 0% to 100% oxygen. The gold target was cleaned by operating the magnetron in pure oxygen for 1 minute between measurements for each gas mixture. Three spectra were collected at each argon-oxygen ratio.

For the neutral species analysis, trapezoidal integration of the spectra was used to compute areas of atomic oxygen, carbon monoxide, carbon dioxide, and toluene. These areas were plotted vs. oxygen flow rate. Mass spectra of neutral species showed the amount of atomic oxygen, carbon monoxide, and carbon dioxide

increased with oxygen concentration while the amount of toluene decreased with increasing oxygen concentration (Figure 5.1.13).

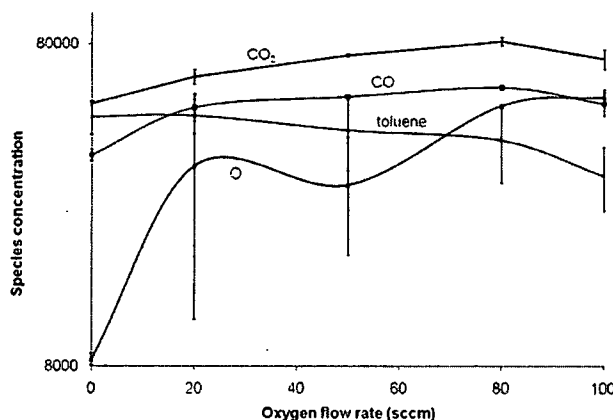


Figure 5.1.13: Species concentration vs. oxygen flow rate (where oxygen flow rate + argon flow rate = 100).

The effect of oxygen to argon concentration ratio on the toluene ion concentration was evaluated. Ionized toluene has characteristic major peaks at 91 ($C_7H_7^+$) and 92 ($C_7H_8^+$) amu as well as minor peaks at 93 and 94 amu. For the collected spectra, the toluene ion concentration was computed by trapezoidal integration from 90 to 95 amu. The toluene ion concentration reached steady state after 4-5 minutes of deposition for all mixtures but the magnitude of the steady state value depends on the gas ratio (Figure 5.1.14). Maximum toluene ion flux was observed at approximately 40% oxygen/60% argon. At greater than 80% oxygen the toluene ion concentration becomes negligible (Figure 5.1.15).

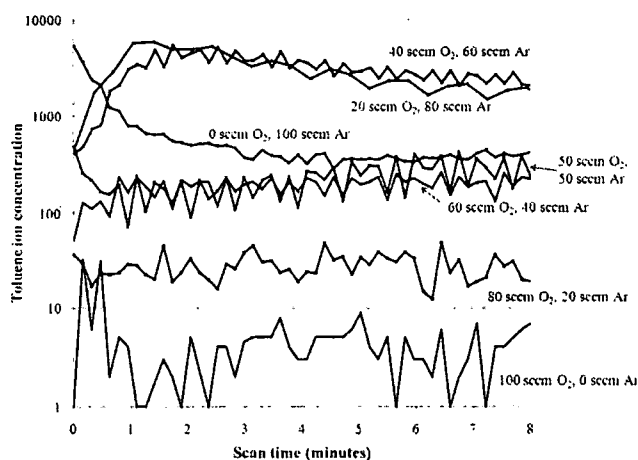


Figure 5.1.14: Toluene ion concentration (90 to 95 amu) vs. scan time for a range of oxygen to argon ratios.

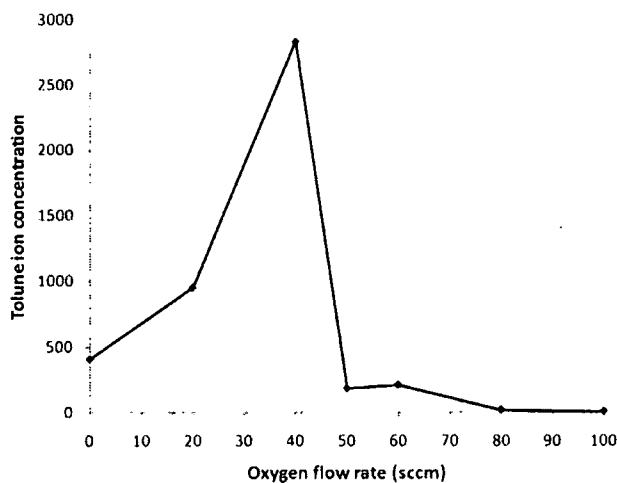


Figure 5.1.15: Integrated toluene ion area (90 to 95 amu) vs. oxygen flow rate at 8 minutes of simultaneous MAPLE and magnetron sputtering.

5.1.3.4 Summary of MAPLE and magnetron sputtering process studies

Carbon deposits on a gold magnetron sputter target and carbon impurities in deposited films were observed while co-depositing using MAPLE with a frozen CNP-loaded toluene target and magnetron sputtering in pure argon. Electrostatic Quadrupole Plasma (EQP) analysis was used to investigate the origin of carbon

impurities and determined that a likely mechanism was a charge exchange reaction between toluene vapor generated from the MAPLE target and the argon plasma originating from the magnetron target. Carbon impurities of co-deposited films were reduced with increasing oxygen concentration using argon-oxygen mixtures. EQP analysis showed that reactive oxygen species such as O and O⁺ effectively remove unwanted carbon during co-deposition processes.

5.2 Structure, morphology, and tribological characterization of carbon nanopearl films

In this section, results of tribological studies of CNP films are presented. Additionally, characterization studies were conducted using optical microscopy, SEM, EDS, Raman spectroscopy, and XPS in order to gain further understanding of tribological mechanisms of CNPs.

5.2.1 Drop cast carbon nanopearl films

A Raman spectrum of a methanol drop cast CNP film shows D and G bands, consistent with a disordered carbon structure containing sp²-bonded crystallites (Figure 5.2.1). Similar characteristics are observed in spectra from amorphous carbon and DLC coatings (see section 2.1.3).

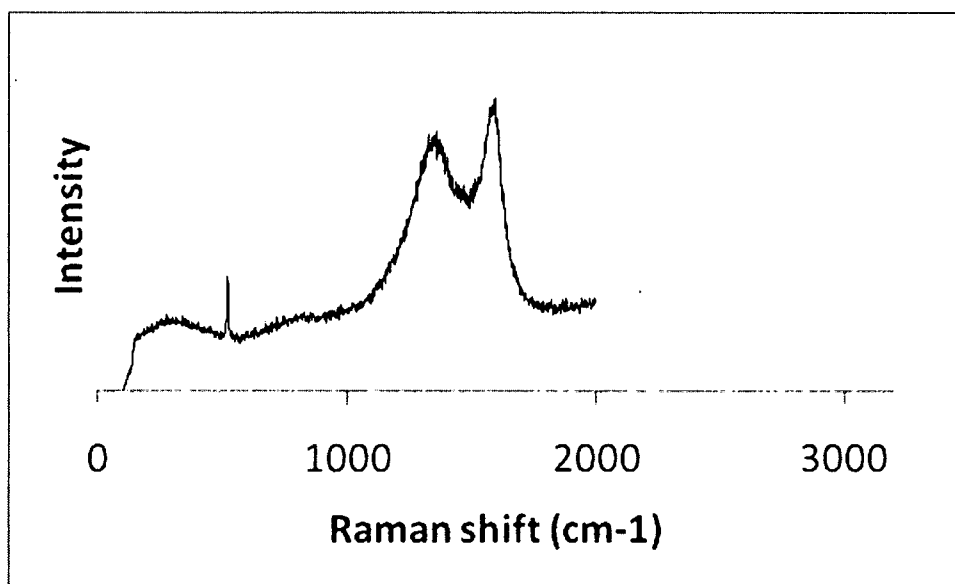


Figure 5.2.1: Raman spectrum of methanol drop cast carbon nanopearls on silicon

An XRD spectrum of graphite powder showed the (002) graphite peak centered at 26.6° diffraction angle, while the carbon nanopearl (002) peak was centered at 24.2° , which is expected for spherical carbon synthesized by CVD [83,2]. Applying Bragg's Law to the diffraction angle data, the interplanar spacing for graphite powder and carbon nanopearls are $3.35 \pm 0.03 \text{ \AA}$ and $3.57 \pm 0.03 \text{ \AA}$ respectively. The larger interplanar spacing indicates that the graphene planes within the nanosized flakes may be easier to shear because the interplanar π - π bond strength is lower. In summary, the higher compressive stress and greater interplanar spacing of nanocrystalline graphene flakes, and the presence of amorphous carbon regions in between the flakes could facilitate the shearing of individual graphene layers, generating lower friction coefficients.

In ball-on-disk tribometer tests of methanol drop cast CNP films, the CNP material effectively reduced the friction coefficient in both humid and dry air as compared to an uncoated Si wafer (Figure 5.2.2). The friction coefficient of CNPs was lower in dry air than humid air environment, in contrast to graphite (Figure 5.2.2). The differences in friction behavior of CNPs and graphite powder are likely due to the structure of the graphite contained in the two materials. The graphene planes within the nanopearls are curved, while pure graphite has a planar structure.

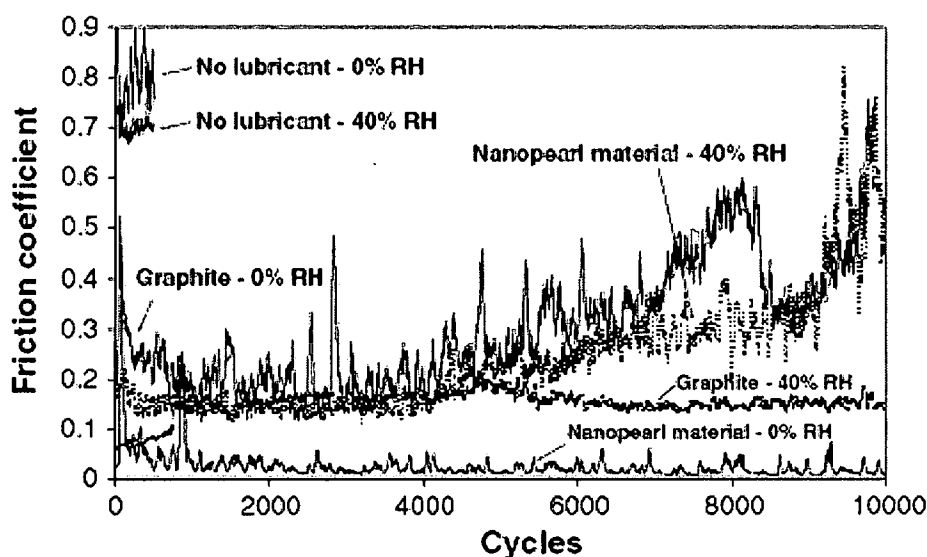


Figure 5.2.2: Friction coefficients in ball-on-disk tribometer tests on silicon wafers with methanol-dispersed nanopearl material and graphite powder in 40% and 0% relative humidity.

To understand the difference in humidity dependence of the nanopearl material from that of a typical graphitic material, a detailed analysis of wear areas was performed with SEM and energy dispersive spectrometry (EDS). For the humid air specimen, the wear track was distinguishable from the surrounding area by a light-colored streak that appeared to be largely featureless at a higher magnification, with the exception of

a few isolated objects (Figure 5.2.3). One such object is shown with a higher magnification in Figure 5.2.3. It is roughly spherical but appears to be deformed with a wrinkled, dimpled morphology. This could possibly be a clustered agglomerate containing deformed CNPs. An EDS spectrum of a region on the surface encompassing the wear scar showed that the composition was predominantly silicon. A compositional map of the wear scar created using EDS showed that the amount of carbon in the wear scar and the surrounding area was very low (Figure 5.2.4), indicating that the nanopearl carbon material was pushed out of the wear track by the ball. A region to the side of the wear track showing CNP material that has been pushed aside is shown in Figure 5.2.3.

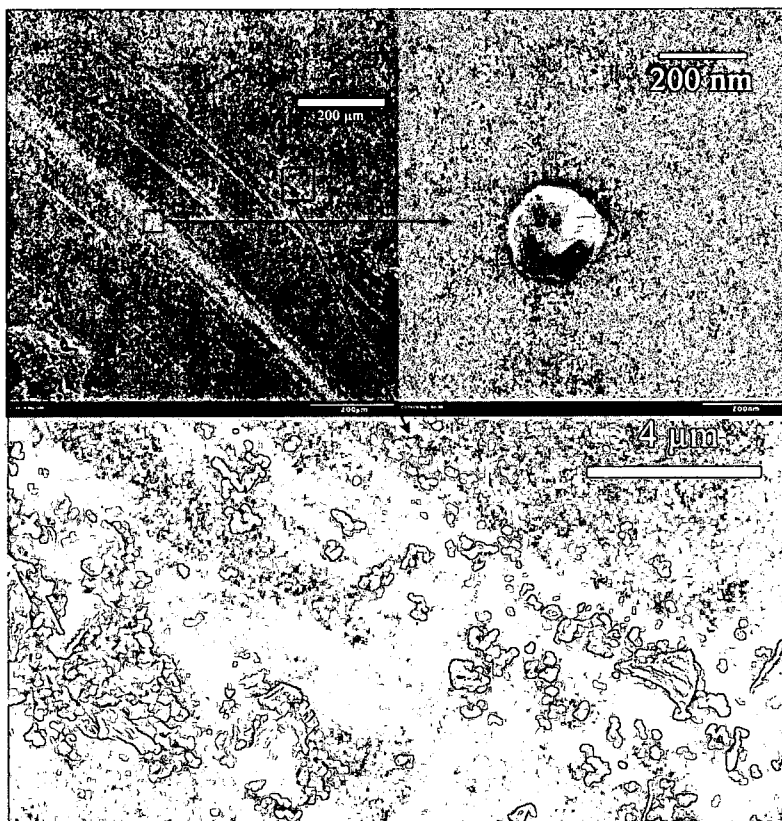


Figure 5.2.3: SEM micrographs of CNP coated surface of silicon wafer in the middle of a wear track after ball-on-disk tribometer test (40% relative humidity).

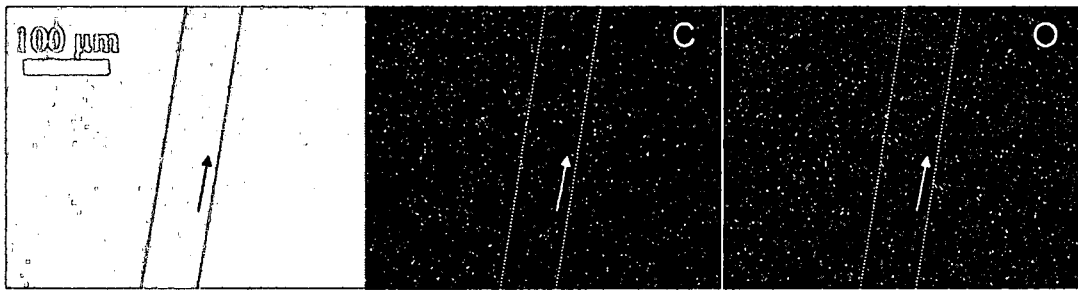


Figure 5.2.4: EDS area composition maps (carbon and oxygen) of the wear track on CNP-coated surface of silicon wafer after ball-on-disk tribometer test (40% relative humidity). Dotted lines indicate wear scar area; arrow indicates sliding direction (Note: scale marker size approximate).

The matching 440C steel ball wear scar from the humid air ball-on-disk tribometer test was also examined using SEM (Figure 5.2.5). Carbon nanopearls were observed over most of the surface of the ball as a residue. As seen in Figure 5.2.5, a large volume of nanopearls accumulated adjacent to the wear scar, facing the advancing side of the silicon wafer. The affinity of the nanopearls appeared to be greater for 440C steel ball than silicon wafer in the humid environment. The nanopearls in front of the wear scar were tightly packed and flattened out, and the layer was on the order of several μm in thickness. The nanopearls appeared to have retained their spherical shape.

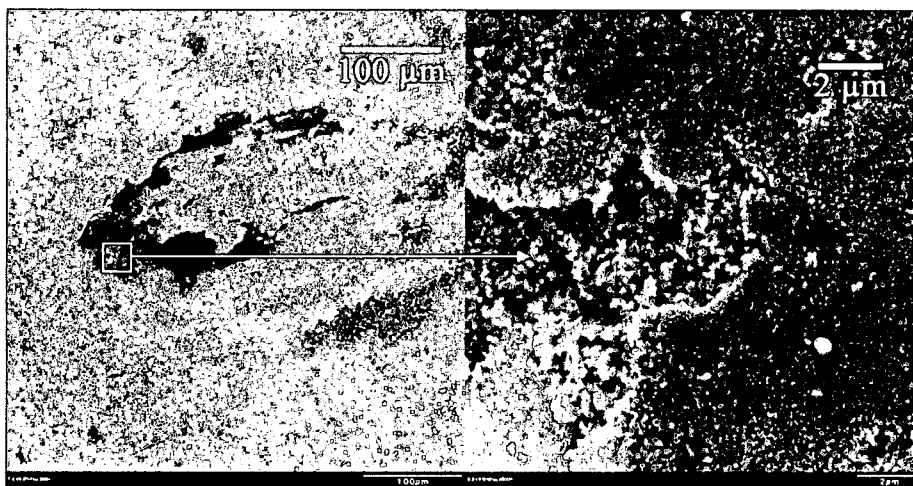


Figure 5.2.5: SEM micrographs of surface of 440C steel ball after pin-on-disk tribometer test in contact with silicon wafer containing carbon nanopearls (40% relative humidity).

For the dry air ball-on-disk tribometer test, the wear track of the silicon wafer appeared to accumulate more wear debris compared to the humid air test specimen (Figure 5.2.6). Higher magnification of wear debris inside the wear track in Figure 5.2.6 showed a porous and loosely attached accumulation of material without the presence of characteristic spherical shapes of nanopearls. An EDS spectrum of a region on the surface encompassing the wear scar showed primarily silicon, with carbon and oxygen also present. A compositional map of the wear scar created using EDS showed a high concentration of carbon debris sites within the wear track, indicating that the debris was composed of carbon nanopearls that underwent a change in morphology due to rubbing between the ball and disk (Figure 5.2.7).

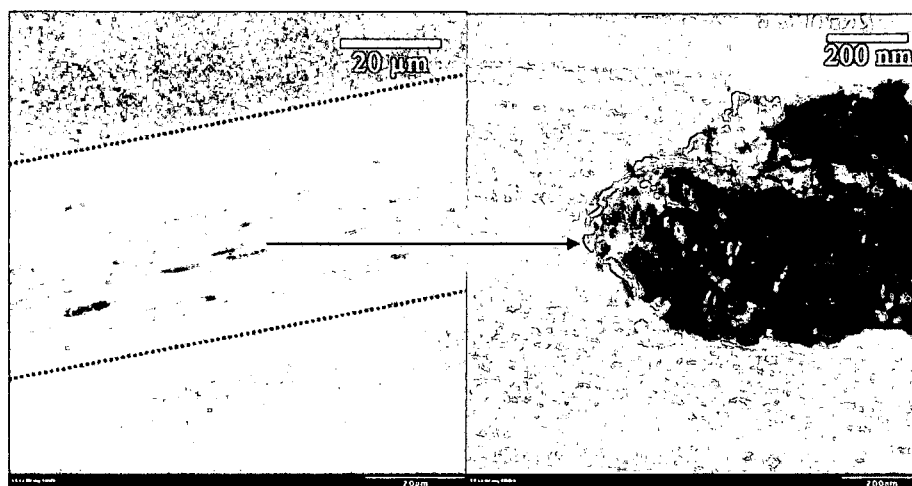


Figure 5.2.6: SEM micrographs of nanopearl-coated surface of silicon wafer after ball-on-disk tribometer test in contact with 440C steel ball bearing (0% relative humidity).

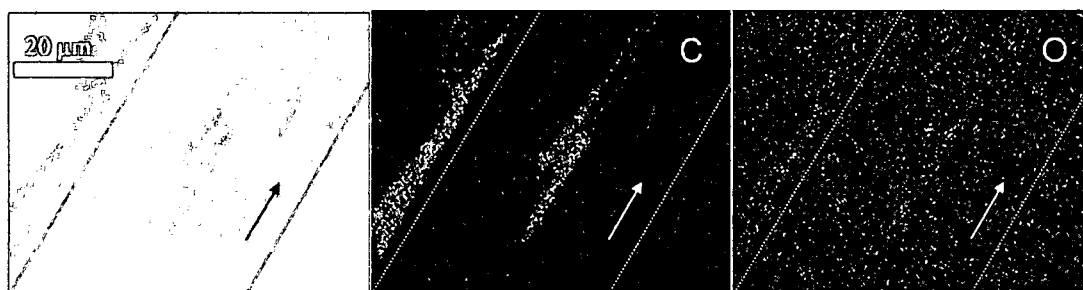


Figure 5.2.7: EDS area composition maps (carbon and oxygen) of the wear track on CNP-coated surface of silicon wafer after ball-on-disk tribometer test (0% relative humidity). Oval indicates wear scar area; arrow indicates sliding direction (Note: scale marker size approximate).

Some CNPs were observed in the contact spot on the matched ball wear scar (Figure 5.2.8), though their presence was much sparser than for the humid air test. In the higher magnification insert of Figure 5.2.8, CNPs appear to have accumulated in a crevice on the surface of the ball bearing. Similar to the humid air tests, the CNPs adjacent to the wear scar were tightly packed and flattened out, and the layer is on the order of several microns in thickness.

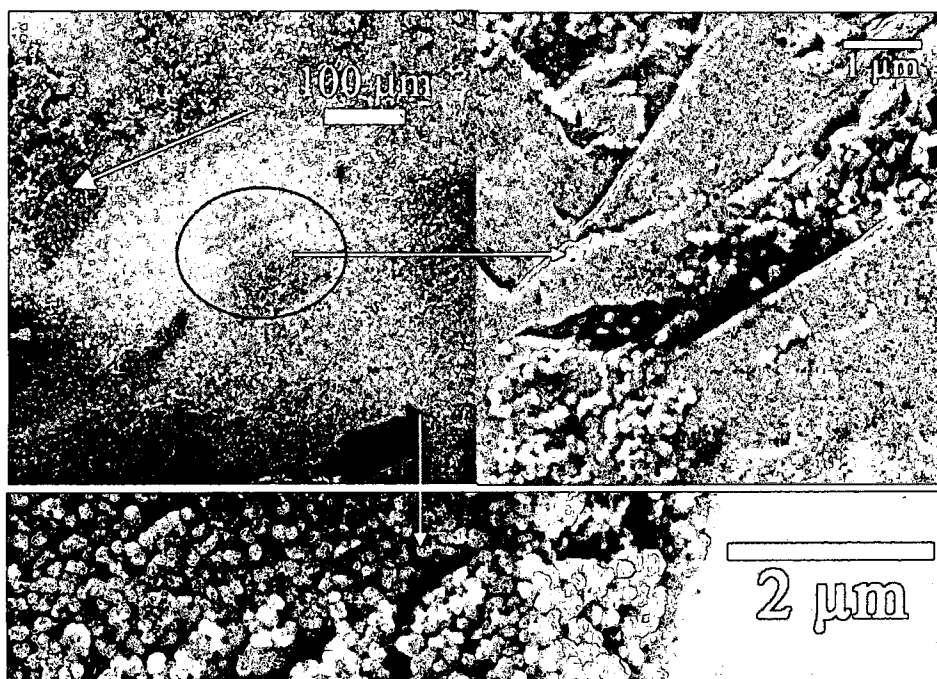


Figure 5.2.8: SEM micrographs of surface of 440C steel ball after ball-on-disk tribometer test in contact with silicon wafer containing carbon nanopearls (0% relative humidity). Arrow indicates sliding direction; oval indicates contact area.

The lubrication effect in the ball-on-disk tests is likely due to the nano-sized graphene flakes contained in the CNPs. However, the tribological behavior of carbon nanopearls under humid and dry environmental conditions contrasts that of graphite. In the dry air case, a transfer film was created in the wear track in which the CNPs were compacted into micron-sized masses and were no longer individual spheres (Figure 5.2.6). At the same time, there was still a possibility for individual flake shearing from the surface of the nanopearls, since the graphene planes are only ~4 nm in size and are surrounded by amorphous material regions as described earlier, which may allow for the ease of material shear. This is in contrast to the well developed microcrystalline graphitic planes in the graphite powder, where shear of graphite

basal planes relative to each other requires the presence of water vapor [48]. Thus in dry conditions the graphite shows higher friction than the nanopearls.

In the humid air case, the wear track did not appear to contain a transfer film. One explanation is that the moisture present on the surface in the humid air helped to reduce locking between individual CNPs, in essence similar to polar fluids which are used to reduce surface energy and disperse nano-powder materials, preventing their interlocking into agglomerates. In these experiments, the absorption of water molecules on CNP surfaces prevented interlocking between the CNPs and the substrate surface, which resulted in removal of the material to the sides of the ball under mechanical pressure and contact sliding, promoting higher friction coefficients. The absence of moisture in the dry air case caused more of the CNPs to remain in the wear track throughout the test, creating the transfer film and lowering the friction coefficient. For much larger (up to 250 micron diameter) graphite powder materials, the presence of water did not lead to powder removal from the wear tracks and the water molecules aided in the shear of the graphite planes via intercalation or edge site mechanism.

Fretting wear tests were conducted in both humid lab air and dry nitrogen environments using a M50 steel ellipsoid and a M50 steel flat disk in order to evaluate the friction behavior of carbon nanopearls in a different wear regime. The presence of CNPs in the fretting contact resulted in reduced friction coefficients for both the humid and dry air cases (Figure 5.2.9). In the humid air, specimens failed at

~300-400 fretting cycles while in the dry air specimens failed at ~500-600 cycles.

Similarly to sliding tests, the CNP material performed better in dry environment than in humid.

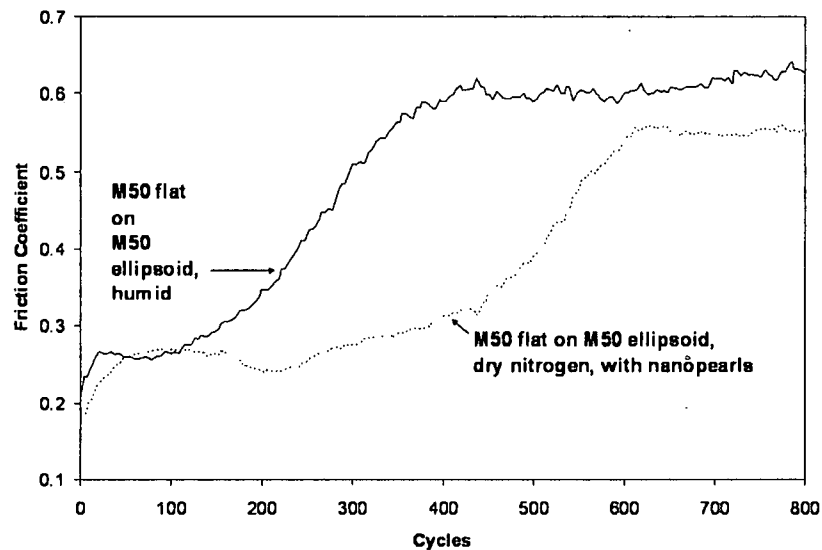


Figure 5.2.9: Friction coefficient vs. number of cycles for M50 steel ellipsoid on M50 flat fretting wear test.

SEM examinations of the wear scar of the humid air specimen showed that the contact area appeared to be mostly free from debris (except for a region near the center of the wear scar) and appeared to be covered with a film layer (Figure 5.2.10). An EDS compositional map showed that the wear scar contained very little carbon but a high concentration of oxygen, indicating that the CNP material was pushed out of the wear area as in the ball-on-disk tests and that the film layer was oxidized steel (Figure 5.2.10).

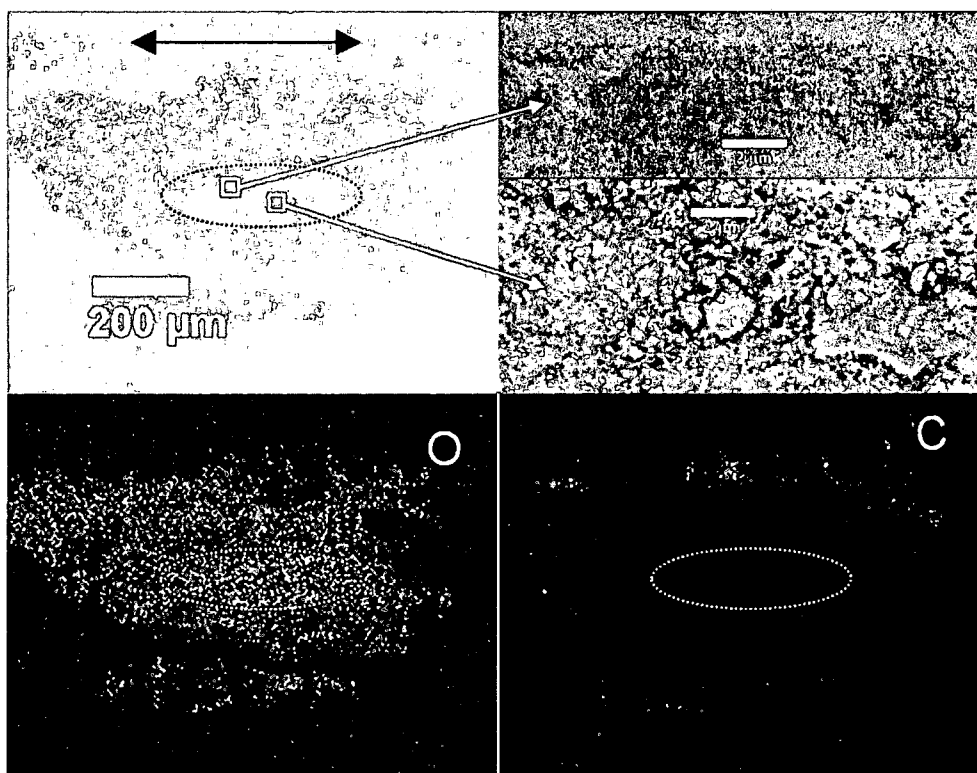


Figure 5.2.10: EDS compositional map (oxygen and carbon) of surface of M50 ellipsoid sample after fretting wear test in humid air environment. Oval indicates contact area; arrow indicates sliding direction.

SEM examinations of the wear scar region of the dry air fretting wear specimen are shown in Figure 5.2.11. A large accumulation of CNP material, presumed to be pushed to the side during the fretting test, was observed adjacent to the wear scar. However, the wear scar also contained stripes of material oriented perpendicular to the fretting direction; SEM examination showed that the material had a flatter texture with no nanopearl spheres observed (Figure 5.2.11). An EDS compositional map showed that the stripes within the wear scar contained carbon, indicating that a transfer film of highly deformed carbon nanopearls was formed as a result of the fretting test (Figure 5.2.11). In summary, carbon nanopearls in high contact stress fretting wear tests using M50 steel samples were pushed completely out from the

wear scar in humid air environments. However, in dry air environments the CNPs became highly deformed and created a transfer film at the wear scar site. This explained their comparatively longer endurance in dry conditions versus humid.

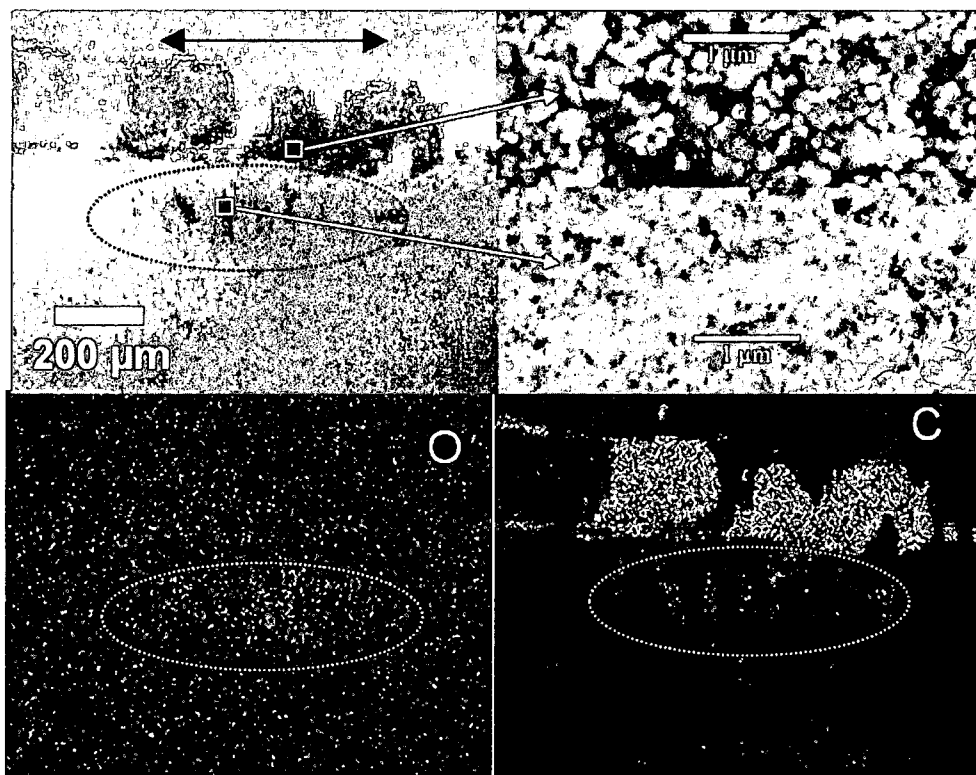


Figure 5.2.11: EDS compositional map (oxygen and carbon) of surface of M50 ellipsoid sample after fretting wear test in dry air environment. Oval indicates contact area; arrow indicates sliding direction.

In summary, the tribological properties of carbon nanopearls were studied in both humid air and dry nitrogen environments and compared to that of graphite powder as a reference material. CNPs showed good lubricating properties in dry conditions, where a transfer film was created in which morphology changed from nano-sized spheres to micron-sized agglomerates consisting of many highly deformed CNPs. The lubricating effect was attributed to the high compressive stress and larger

interplanar spacing of nano-crystalline graphene flakes, and the presence of amorphous carbon regions in between the flakes, which allowed for easy shearing of individual flakes in the dry conditions. In dry environments, the CNP compaction and shear provided a third body transfer film for both sliding and fretting contacts, facilitating friction reduction and longer wear lives. The unusually low sliding friction coefficient of 0.03 in dry conditions was in contrast to the higher friction of graphite powder, which varied between 0.2 and 0.5. Such dramatic relative reduction of friction was attributed to CNP material compaction in the contact area and formation of a transfer film to accommodate sliding velocity. One possible mechanism of the transfer film formation could be peeling off and shearing of small graphene flakes from the wrapped layer structure of carbon nanopearls. In humid environments carbon nanopearls were less lubricious due to their inability to remain in the contact point and accommodate relative motion of the sliding contact. Some transfer film is created during the sliding process in humid environments, providing residual lubrication after the CNPs have been pushed out of the wear track, but the amount of material is much less than that created in dry environments. The CNPs were flattened by the ball contact but were removed from the wear track because moisture prevented interlocking between the intact or flattened CNPs and the silicon surface.

5.2.2 MAPLE-deposited carbon nanopearl films

A thin film sample consisting of CNPs deposited by MAPLE onto a silicon wafer was examined using optical microscopy and Raman spectroscopy (Figure 5.2.12). The deposition parameters of the film were as follows: laser target 0.08 wt. % CNP in methanol, 500mJ laser energy, 3 Hz repetition rate, 7 min laser deposition time, unregulated (vacuum) background pressure, and substrate temperature 100°C. The film contained some micron-sized agglomerations of CNPs, shown in Figure 5.2.12. Raman spectra collected at the spot of an agglomeration reveal the presence of characteristic D and G peaks typical of disordered carbon material containing graphitic crystallites and similar to the methanol drop cast Raman spectra.

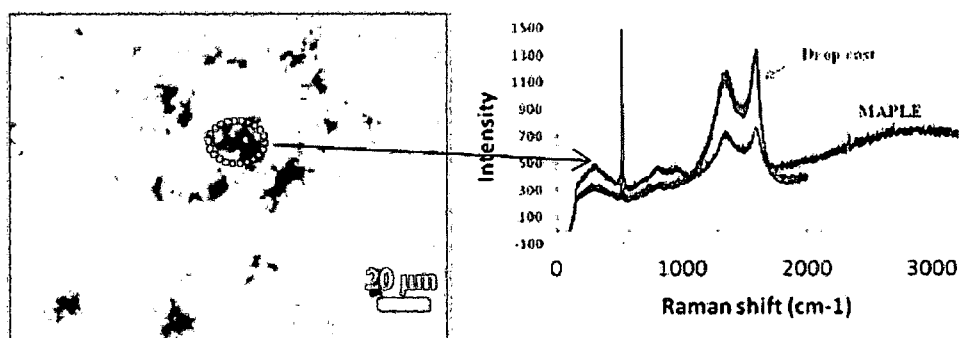


Figure 5.2.12: Optical micrograph and Raman spectrum of MAPLE film (target: 0.08% carbon nanopearls in methanol, 500 mJ, 3 Hz, 7 minute deposition time, 100°C substrate temperature) deposited onto a silicon wafer. Oval indicates region from which the Raman spectrum was collected. Methanol drop cast Raman spectrum shown for comparison.

Ball-on-disk tribometer tests of the MAPLE-deposited film described in the preceding paragraph were conducted in dry nitrogen (0% relative humidity) and humid air (40% relative humidity) environments. In dry nitrogen environment, the average friction

coefficient for 2 of the 3 replicate tests was high (~ 0.6) while very low friction (friction coefficient less than 0.1) was observed for 1 of the 3 replicate tests. The wear tracks were observed using optical microscopy and Raman spectroscopy (Figure 5.2.13). The wear tracks of the two high friction tests contained discoloration in the direction of relative motion of the steel ball and appeared to contain some wear debris or transfer film. Raman spectra from the worn area are consistent with disordered carbon with the possible presence of CNP material. The wear track of the low friction sample did not appear to contain a transfer film or wear debris. Some material was observed adjacent to the wear track on both sides. A Raman spectrum of this material was consistent with disordered carbon and similar to CNPs. The variation in the friction performance between the three replicate samples could be due to the low amount of CNP material on the surface. The two high friction samples probably did not have CNP material at the contact point with the steel ball but the low friction sample probably did.

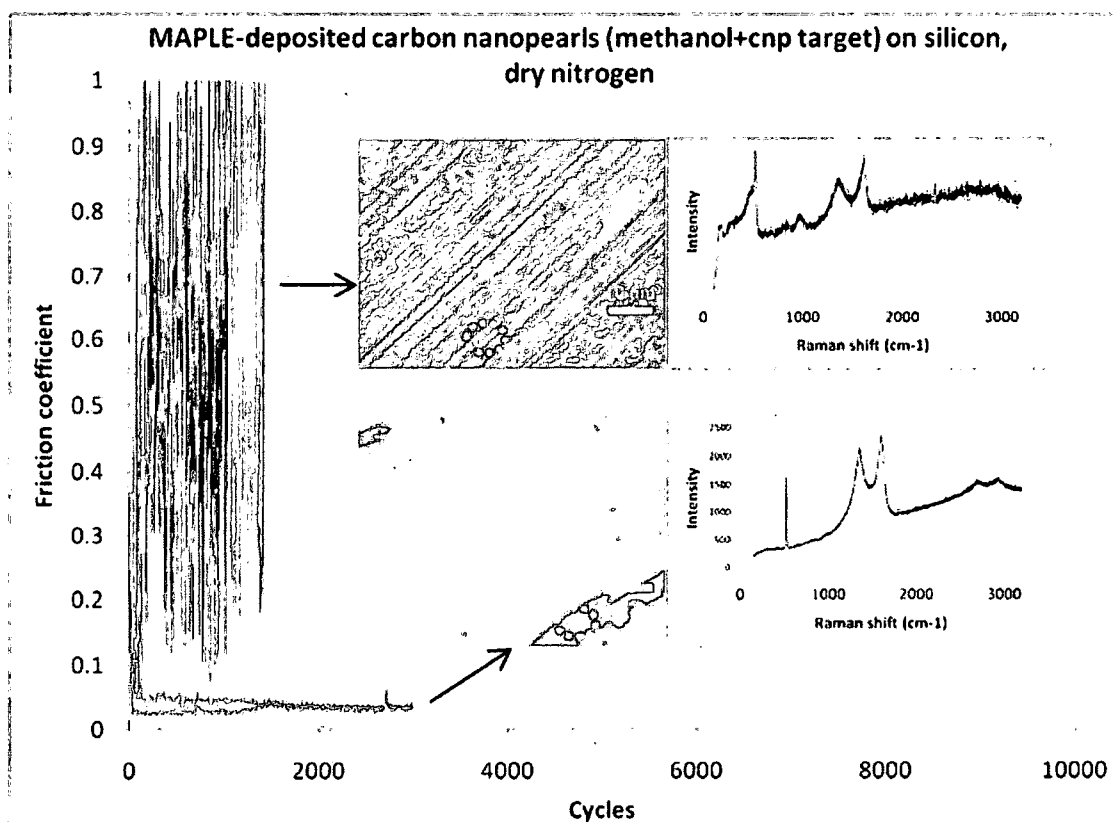


Figure 5.2.13: Friction coefficient of MAPLE film (target: 0.08% carbon nanopearls in methanol, 500 mJ, 3 Hz, 7 minute deposition time, 100°C substrate temperature) deposited onto a silicon wafer during ball-on-disk tribometer testing in dry nitrogen (0% relative humidity). Inset: optical micrographs and Raman spectra of wear tracks. Ovals indicate regions from which the Raman spectra were collected.

The average friction coefficient in humid air environment for the MAPLE deposited film was ~0.3 for all three ball-on-disk tribometer tests. The wear tracks appeared to contain a transfer film or wear debris at the ball contact point (Figure 5.2.14). Raman spectra from this location were not consistent with disordered carbon or CNPs (Figure). The CNPs appeared to be pushed away from the wear track, displaying behavior similar to what occurred in the drop cast CNP films.

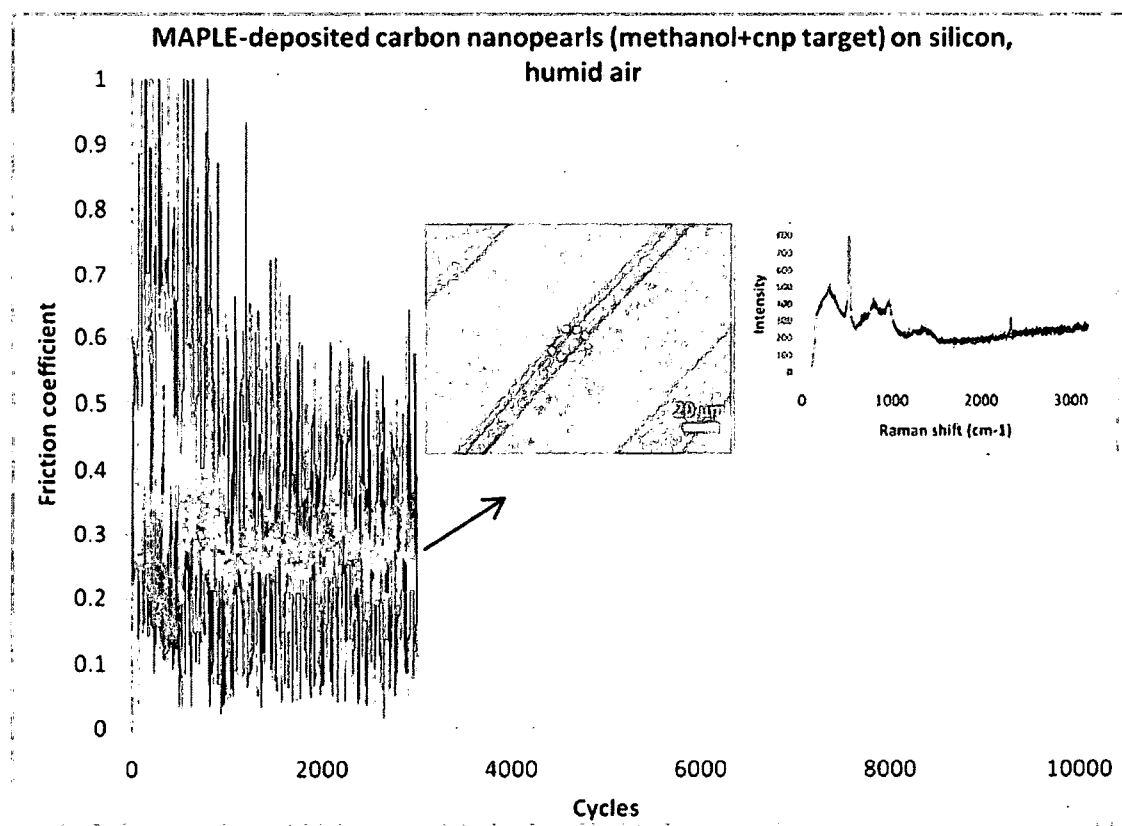


Figure 5.2.14: Friction coefficient of MAPLE film (target: 0.08% carbon nanopearls in methanol, 500 mJ, 3 Hz, 7 minute deposition time, 100°C substrate temperature) deposited onto a silicon wafer during ball-on-disk tribometer testing in humid air (40% relative humidity). Inset: optical micrograph and Raman spectrum of wear track. Oval indicates region from which the Raman spectrum was collected.

In summary, a thin film sample consisting of CNPs deposited by MAPLE onto a silicon wafer was characterized using a ball-on-disk tribometer, optical microscopy, and Raman spectroscopy. The friction performance among three replicate tribometer tests in a dry nitrogen environment had a wide range, probably due to the low amount of CNP material on the surface. In a humid air environment, the CNPs appeared to be pushed out of the wear tracks, behavior that was also observed in drop cast CNP films tested under the same conditions.

5.2.3 MAPLE and magnetron sputter-deposited gold/CNP films

Based on processing regimes identified with the EQP mass spectrometer, composite gold-carbon nanopearl films were synthesized using simultaneous MAPLE and magnetron sputtering on silicon substrates using two background gas mixtures, one at 20% oxygen, 80% argon and the other at 90% oxygen and 10% argon. All other deposition conditions, listed in Table 4.2.2, were identical. The coating deposition rate for the 80% argon sample (20.0 nm/min) was over 2.5 times greater than that of the 10% argon sample (7.4 nm/min), which was expected because the energy transfer between incident atomic ions on the gold target atoms is lower for oxygen compared to argon due to the lower atomic mass of oxygen and the fact that half of the oxygen atoms in molecular ions are reflected from the sputter target as energetic neutrals [84]. In addition, small differences in kinetic energy can have large effect on the sputtering yield, which increases strongly with ion energies in the range 50-500 eV for gold targets [85].

Samples synthesized by MAPLE and magnetron sputtering co-deposition at different oxygen to argon ratios were characterized using XPS (Figure 5.2.15). A sample that was deposited using 100% argon background contained mostly carbon (99.64 atomic % C, 0.36 atomic % Au) while a sample deposited using a background mixture of 90% oxygen and 10% argon (sample MM-20 listed in Table 4.2.2) contained both gold (56 atomic %) and carbon (44 atomic %). These results are in agreement with the hypothesis that carbon deposits accumulate on and are sputtered from target

surfaces in the presence of argon and incorporated into substrate films and that the carbon deposits are reduced or eliminated in the presence of oxygen.

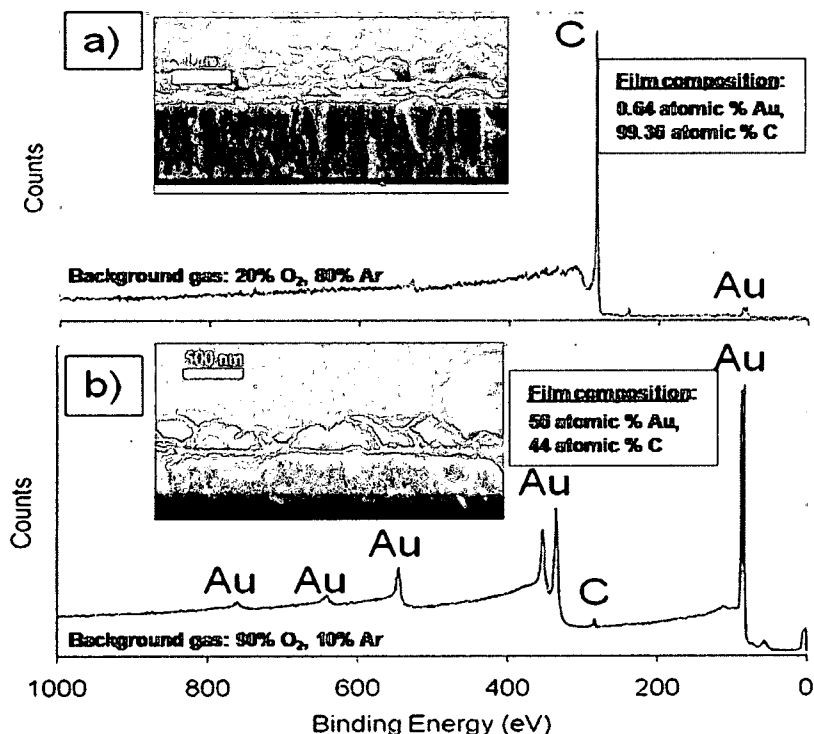


Figure 5.2.15: XPS spectra and cross sectional SEM micrographs of thin films deposited using simultaneous MAPLE (target: 0.08% carbon nanopearls in toluene, 700 mJ, 1 Hz) and magnetron sputtering (Au target, 30W power): a) in 20% oxygen and 80% argon, and b) 90% oxygen and 10% argon as background gases

In order to understand the role of CNPs in lubrication of MAPLE and magnetron sputter-deposited gold thin films, tribological testing was performed on two films deposited onto 440C steel substrates. Details of the depositions are contained in Table 4.2.2 (sample ID# MM-18 and MM-19). Briefly, an adhesive interlayer consisting of chromium and gold was sputtered, then MAPLE (700 mJ, 1 Hz, 20°C substrate temperature, 150V substrate bias) and magnetron sputtering (gold target, 30W) were operated simultaneously for 45 minutes with a background gas

composition of oxygen and argon with flow rates of 75 sccm and 25 sccm respectively. Finally, the magnetron was shut off and MAPLE was operated for 15 more minutes. The only difference between the two samples was the composition of the MAPLE target – one had 0.08 wt.% CNP in toluene while the other one used a target consisting only of toluene. These films were examined using SEM. For comparison, a gold film deposited by sputtering in argon was also examined. For the films deposited using simultaneous MAPLE and magnetron sputtering, the size of the gold grains ranged up to approximately 100 nm in size regardless of whether the MAPLE target was loaded with CNPs (Figure 5.2.16 a and b). CNPs can easily be observed embedded in the gold matrix in Figure 5.2.16a. For the sample that was magnetron sputter-coated with gold with no MAPLE, the average size of the gold grains was much smaller (< 25 nm) and below what could be easily observed at the common magnification at which these micrographs were taken. The larger gold grains in the simultaneous MAPLE/sputter-coated samples are likely a result of the presence of hydrocarbons incorporated into the film from the toluene vapor. The MAPLE and sputter-coated films also contain cracks as a result of tensile stresses in the as-deposited films. These stresses likely resulted from the presence of the larger grains. A detailed study of the effect of toluene vapor on film tensile stress and grain size during sputtering was not performed but would be useful as this hybrid processing technique is further developed.

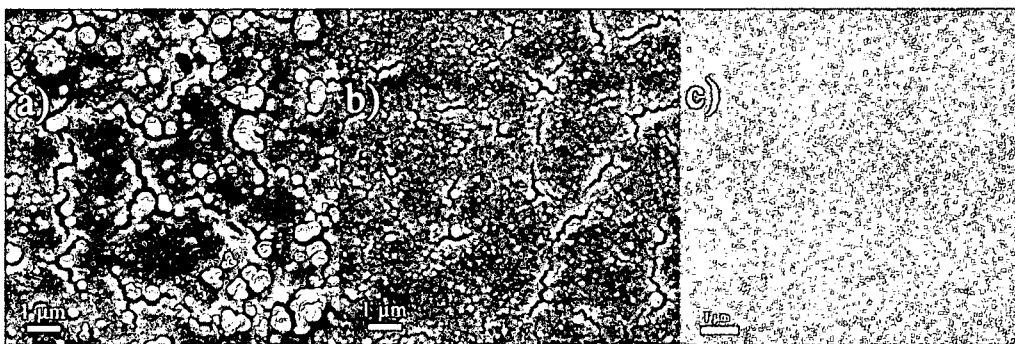


Figure 5.2.16: SEM micrographs of thin films deposited using simultaneous MAPLE and magnetron sputtering (Au target, 30W power): a) AISI 440C substrate, MAPLE target 0.08% CNPs in toluene, 700 mJ, 1 Hz, 15 mTorr, background gas 75 sccm oxygen/25 sccm argon, 20°C substrate temperature; b) AISI 440C substrate, MAPLE target toluene, 700 mJ, 1 Hz, 15 mTorr, background gas 75 sccm oxygen/25 sccm argon, 20°C substrate temperature. Sample c) deposited using sputtering only (Au target, 30W power, 20 mTorr argon @ 100 sccm, 100°C substrate temperature) no MAPLE.

Optical microscopy and Raman spectroscopy of these films were performed (Figures 5.2.17 and 5.2.18). Raman spectra of the two films were similar, suggesting a similar bonding structure, although the morphologies of the films appear quite different, likely due to the CNPs in Sample ID# MM-18.

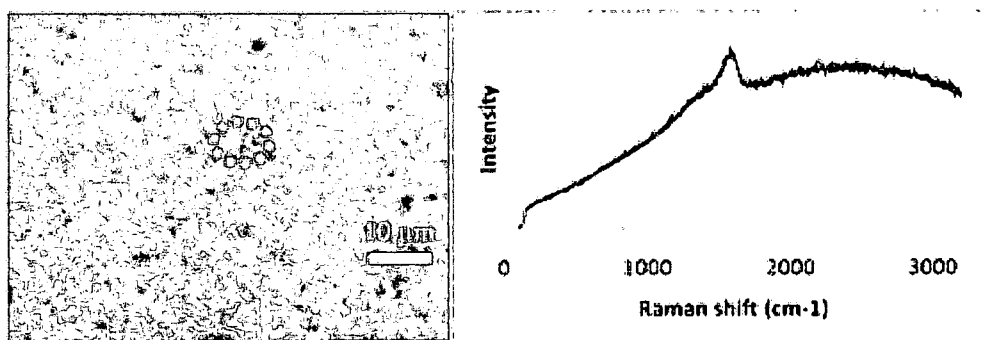


Figure 5.2.17: Sample ID# MM-18: Optical micrograph and Raman spectrum of film deposited using simultaneous MAPLE (target: 0.08% carbon nanopearls in toluene, 700 mJ, 1 Hz, 45 minute deposition time, 20°C substrate temperature, 150V substrate bias, 75 sccm oxygen+25 sccm argon background gases) and magnetron sputtering (Au target, 30W). Oval indicates region from which the Raman spectrum was collected.

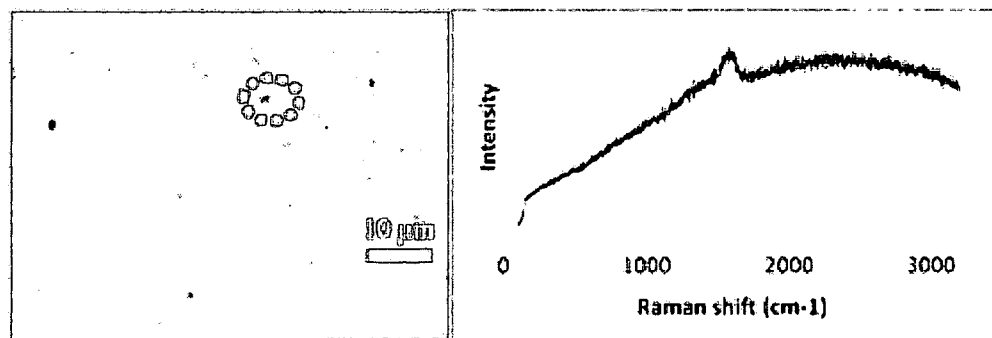


Figure 5.2.18: Sample ID# MM-19: Optical micrograph and Raman spectrum of film deposited using simultaneous MAPLE (target: toluene, 700 mJ, 1 Hz, 45 minute deposition time, 20°C substrate temperature, 150V substrate bias, 75 sccm oxygen+25 sccm argon background gases) and magnetron sputtering (Au target, 30W). Oval indicates region from which the Raman spectrum was collected.

Ball-on-disk tribometer tests of the films described in the preceding paragraph were conducted in dry nitrogen (0% relative humidity) and humid air (40% relative humidity) environments. In dry nitrogen environment, the friction coefficient of both films (deposited using toluene MAPLE targets with and without CNPs) had a low average value of approximately 0.15 (Figure 5.2.19). For comparison, gold films deposited using magnetron sputtering have typical friction coefficients in the range 0.1-0.5; the low end of this range is only observed for a narrow range of film thickness values of ~200 nm [86,87]. In addition, the Raman spectra within the wear tracks of the two films were very similar and were consistent with disordered carbon or CNPs (Figure 5.2.19). The Raman spectra are also both significantly different from the bulk surface in that the D and G peaks are much more pronounced. These results suggest that the behavior of these films is similar to hydrogenated DLC in that low friction is observed and a structure transformation (graphitization) occurs in the wear track during cyclic loading. However, in contrast to typical DLC films that

contain primarily carbon (and up to 50% hydrogen for hydrogenated DLC) these films are composed of gold, carbon, and most likely hydrogen. Several film formation mechanisms are likely in effect: 1) a magnetron sputtering process in which argon and/or oxygen ions are impinging on the magnetron target surface which is composed of both gold and carbonaceous deposits and ejecting both carbon and gold atoms; 2) hydrocarbon vapor, present as a result of toluene melting/evaporation as the laser impinges on the frozen target, is deposited onto the surface by a CVD process; and 3) carbon nanopearls are deposited onto the substrate and magnetron target surfaces by MAPLE (for film deposited using the CNP-loaded MAPLE target).

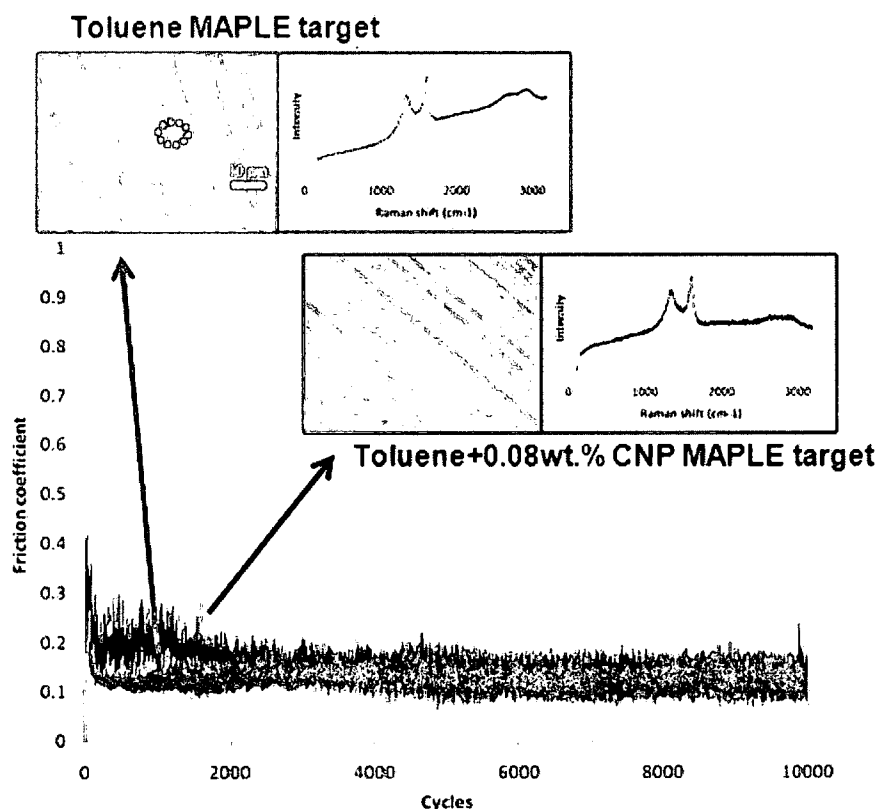


Figure 5.2.19: Friction coefficients during ball-on-disk tribometer testing under dry nitrogen atmosphere (0% relative humidity) of films deposited using toluene MAPLE targets with and without carbon nanopearls. Inset: optical micrographs and Raman spectra of wear tracks. Ovals indicate regions from which the Raman spectra were collected.

In humid air environment, the friction coefficient of the film deposited using a MAPLE target of 0.08 wt.% CNP in toluene had an average value of ~ 0.35 with high amplitude of ~ 0.2 (Figure 5.2.20). For the film deposited using a toluene MAPLE target, the average friction coefficient was ~ 0.2 . The Raman spectra of both films in the wear tracks were similar and consistent with disordered carbon (Figure 5.2.20). As in the dry nitrogen environment, the film deposited using a toluene MAPLE target had a low friction coefficient and graphitization of the bonding structure under friction loading. However, the friction behavior of film deposited using a MAPLE target of 0.08 wt.% CNP in toluene was not consistent between dry and humid environments. The humidity dependence of this film is similar to the drop cast CNP film described in Section 5.2.1. The CNPs likely do not have a strong adhesive bond to the gold matrix, so they are able to separate from the matrix under friction loading and be pushed to the side of the wear track by a similar mechanism as occurs with the drop cast films. The higher friction coefficients observed for the gold-CNP films in humid air are presumed to be a result of craters and wear debris due to pullout of these gold covered CNP clusters. This process is depicted schematically in Figure 5.2.21.

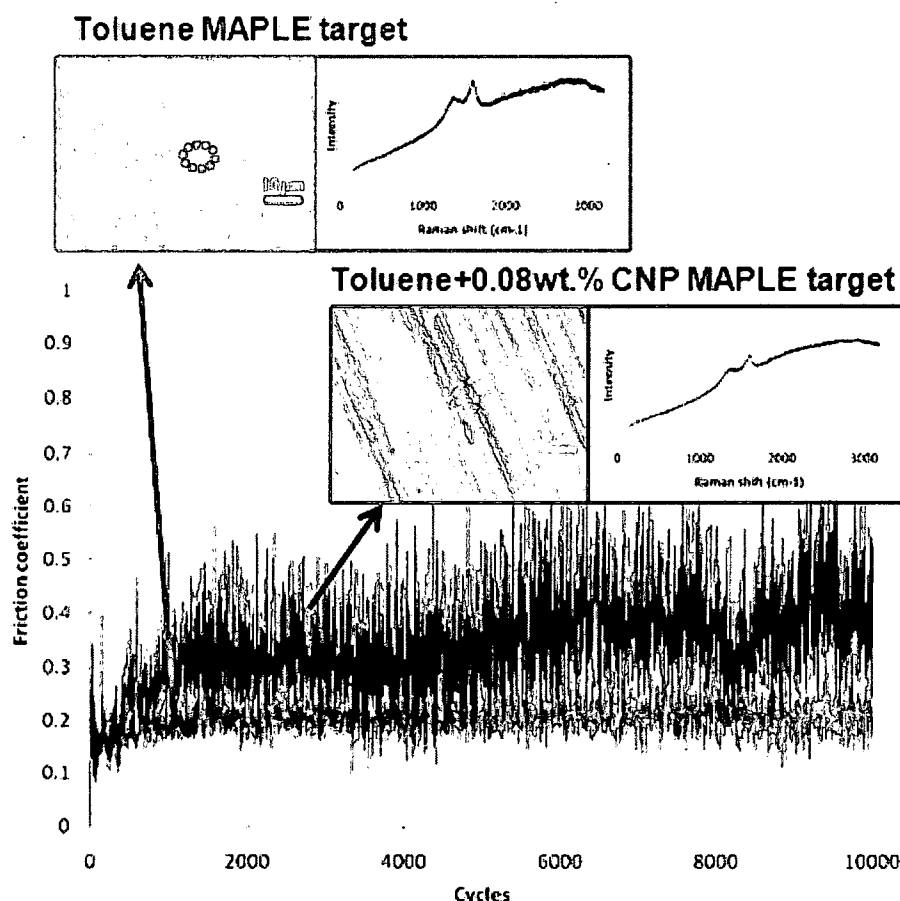


Figure 5.2.20: Friction coefficients during ball-on-disk tribometer testing under humid air atmosphere (40% relative humidity) of films deposited using toluene MAPLE targets with and without carbon nanoparticles. Inset: optical micrographs and Raman spectra of wear tracks. Ovals indicate regions from which the Raman spectra were collected.

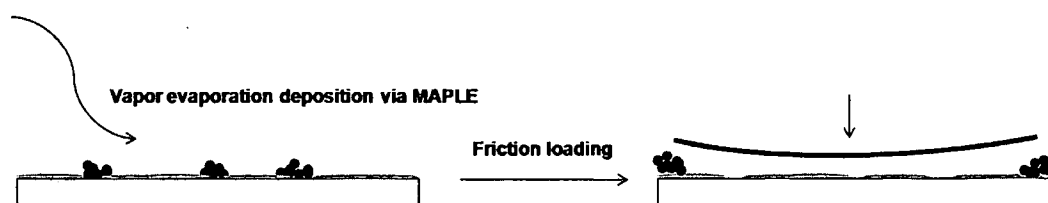


Figure 5.2.21: Schematic drawing showing morphological changes under friction loading for simultaneous MAPLE and sputter-deposited film with CNP in a gold matrix

In addition to the use of oxygen as a background gas (as discussed in section 5.1.3 above) for simultaneous deposition using MAPLE and magnetron sputtering, carbon

impurities on sputter targets and deposited films could also be reduced by a number of other strategies. Solvents containing oxygen in the molecular structure (e.g. methanol, acetone, DMSO) could be used for the MAPLE target matrix. This would reduce the amount of additional oxygen necessary to react with the carbon deposited from the matrix, although these solvents have been shown to produce a lower yield of solute material deposited via the MAPLE process [88]. Another possibility for examining the contribution of ionized and neutral toluene species is the use of an alternative background gas in place of argon to mitigate or eliminate the charge exchange process that generates toluene ions. Furthermore, charge exchange reactions of any kind could be avoided by alternating magnetron sputtering and MAPLE rather than operating them at the same time. Depending on the time between laser and magnetron cycles, most of the toluene vapor could be pumped out of the chamber before it became ionized.

A strategy for avoiding unwanted carbon deposition was explored by sequentially rather than simultaneously depositing CNPs using MAPLE and magnetron sputtering. After depositing a graded chromium/gold interfacial film by sputtering in argon, the magnetron and the argon gas were turned off. MAPLE (target: 0.08% carbon nanopearls in toluene, 700 mJ, 1 Hz) was operated for 60 minutes in vacuum (unregulated background pressure). After the MAPLE deposition, the laser was shut off, the argon gas was turned back on, and gold was sputtered for 45 minutes at 30W. A complete list of deposition parameters and process sequences for this film is listed in Table 4.2.2 (Sample ID# MM-23). After the silicon wafer substrate was removed

from the deposition chamber it was snapped into pieces using a straight-edge to allow examination of the film in cross section. SEM examination revealed that the adhesion between the initial chromium/gold interlayer and the outer sputtered gold layer was very poor. In the SEM micrograph shown in Figure 5.2.22, the outer gold layer can be seen peeling away from the bottom chromium/gold layer. In addition, several sheets of gold are piled on top of one another, which likely occurred as the silicon wafer sample was broken at this location. This result is consistent with the hypothesis that the adhesive bonding between sputtered gold and CNPs is weak. The adhesive bonding strength between gold and amorphous carbon deposited by MAPLE with toluene target is also probably low, leading to the delamination that occurred with this film.

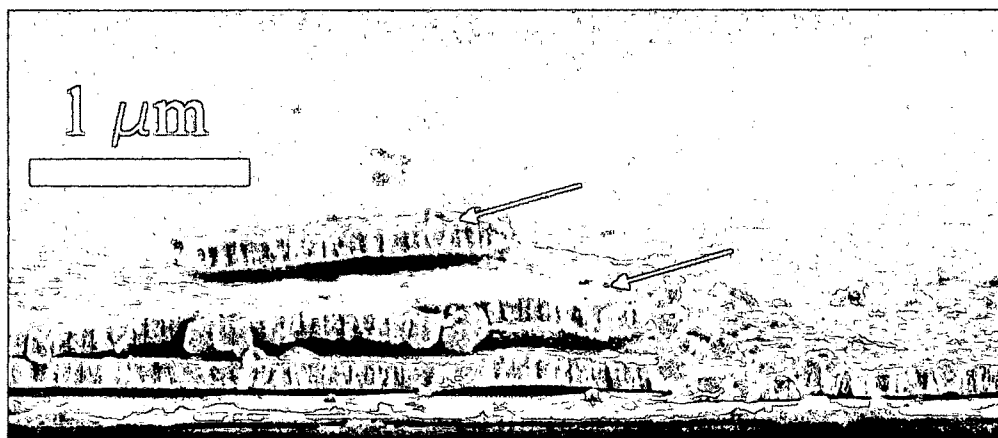


Figure 5.2.22: Cross-sectional SEM micrograph of sequentially-deposited CNP-gold film (sample ID# MM-23 in Table 4.2.2). Arrows indicate sheets of gold that completely delaminated from the gold/chromium interlayer.

In summary, XPS has shown that the use of oxygen background gas during simultaneous MAPLE and magnetron sputtering significantly reduces the amount of carbon deposited on substrate surfaces. This result is in agreement with EQP data

showing that using oxygen background gas reduces the concentration of toluene ions present during the deposition. The behavior of films deposited using simultaneous MAPLE and magnetron sputtering with a background gas composition of 75% oxygen and 25% argon using toluene MAPLE targets is similar to hydrogenated DLC in that a structure transformation (graphitization) occurs in the wear track during cyclic loading resulting in low friction coefficients. This behavior occurs regardless of whether or not the MAPLE target is loaded with CNPs. The exception to this is in a humid air environment where higher friction coefficients are observed for CNP-loaded targets. The adhesive bonding between the CNPs and the gold matrix appears to be low, and under friction loading the CNPs are likely pushed to the side of the wear track by a similar mechanism as occurs with the drop cast films. Higher friction coefficients observed for the gold-CNP films in humid air are presumed to be a result of craters and wear debris due to pullout of these gold covered CNP clusters.

5.3 Process-property-tribological correlations and mechanisms

Prepared as drop cast films, CNPs are effective as a lubricant under conditions where a transfer film can be formed between the substrate surface and ball contact. The CNPs in the transfer film undergo a morphological transformation from spherical particles to a highly deformed morphology (an example is shown in Figure 5.3.1) in which the nanometer-sized graphitic flakes are distributed throughout the transfer film, and essentially these films are very similar to transfer films formed in DLC coatings.

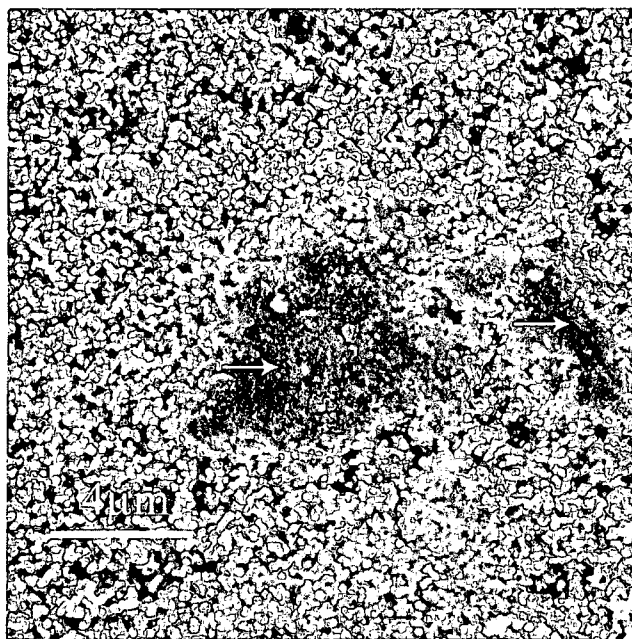


Figure 5.3.1: Drop cast film of CNP on M50 steel after fretting wear test. Arrows indicate contact region where CNPs are flattened and smeared.

It has been demonstrated that CNPs can be combined with gold using simultaneous operation of MAPLE, with CNPs loaded into a toluene matrix, and magnetron sputtering using a gold target to create a nanostructured hybrid film. The resulting materials have good lubricity similar to that of drop cast CNP films. However, the low friction of these films is not solely due to the presence of the CNPs. In fact, carbon and hydrocarbon vapor are incorporated into the films and they can be considered as hydrogenated DLC-gold composites. Under cyclic friction loading, a disordered graphitic transfer film is formed regardless of whether CNPs are present in film or not. Several film formation mechanisms for the DLC-gold composites are likely in effect: 1) magnetron sputtering in which argon and/or oxygen ions are impinging on the magnetron target surface which is composed of both gold and carbonaceous deposits and ejecting both carbon and gold atoms; 2) hydrocarbon

vapor, present as a result of toluene melting/evaporation as the laser impinges on the frozen target, is deposited onto the surface by a CVD process; and 3) carbon nanopearls are deposited onto the substrate and magnetron target surfaces by MAPLE (for film deposited using the CNP-loaded MAPLE target).

6. CONCLUSIONS

The morphology of carbon nanopearl films deposited using a drop cast method was found to be non-uniform and loosely adhered to the substrate. CNP films deposited using a MAPLE system equipped with a 248 nm KrF excimer laser source was found to be influenced by multiple factors, including composition of the matrix solvent, laser energy and repetition rate, background pressure, and substrate temperature. The best parameters for depositing CNP films that are disperse, droplet-free, and have the maximum amount of material deposited with improved adherence compared to drop cast films are as follows: toluene matrix, 700 mJ, 1 Hz, 100°C substrate temperature, and unregulated vacuum pressure.

During co-deposition of thin films using MAPLE (with a frozen CNP-loaded toluene target) and magnetron sputtering (using a gold target) in pure argon, carbon deposits were observed on the gold magnetron sputter target surface, caused by electron ionization of toluene vapor generated from the MAPLE target and charge exchange reactions between toluene vapor and the argon plasma generated by the magnetron. Thin films deposited under these conditions contained high amounts of undesired carbon (99.36 atomic % carbon as measured by XPS) because carbon rather than gold was sputtered from the magnetron target surface. Carbon impurities of co-deposited films were reduced with increasing oxygen concentration using argon-oxygen

mixtures; EQP analysis showed that reactive oxygen species such as O and O⁺ effectively remove unwanted carbon during co-deposition processes.

Friction coefficients of CNPs drop cast onto silicon during ball-on-disk tribometer tests in humid air environments were comparable to that of graphite powder up to 5000 cycles. However, formation of CNP transfer films was inhibited by absorption of water molecules on the surface.

Drop cast CNPs tested under dry conditions showed excellent lubricating properties in sliding contacts, where a transfer film was created in which morphology changed from nano-sized spheres to micron-sized agglomerates consisting of many highly deformed CNPs. The CNP compaction and shear provided a third body transfer film for both sliding and fretting contacts, facilitating friction reduction and longer wear lives. These results support the transfer film formation mechanism in which small graphene flakes are peeled off and sheared from the wrapped layer structure of carbon nanopearls. The friction coefficients measured in dry environments were much lower than for graphite powder, indicating that CNPs could be very useful for space lubrication applications.

The tribological behavior of films deposited using simultaneous MAPLE and magnetron sputtering was similar to hydrogenated DLC in that a structure transformation (graphitization) occurred in the wear track during cyclic loading resulting in low friction coefficients. In fact, carbon and hydrogen fragments from

solvent vapor are incorporated into the films leading to the formation of hydrogenated DLC-gold composites. This behavior occurs for frozen toluene MAPLE targets regardless of whether they are loaded with CNPs. The exception to this is in a humid air environment. The adhesive bonding between the CNPs and the gold matrix was found to be poor, and under friction loading the gold covered-CNP clusters are likely disbonded from the matrix and pushed to the side of the wear track by a similar mechanism as occurs with the drop cast films. The higher friction coefficients observed for the gold-CNP films in humid air environments are presumed to be a result of craters and wear debris due to pullout of these gold covered CNP clusters. CNP-gold nanostructured hybrid thin films deposited using a sequential process with MAPLE and magnetron sputtering also exhibited a low adhesion at the interface between the MAPLE-deposited layer and the magnetron-sputtered gold layer deposited on top of the MAPLE layer. The adherence of these films was acceptable for the tribological tests, but further process optimization for the hybrid composite films may be needed.

These studies demonstrated for the first time that MAPLE combined with sputtering can be used for embedding nanostructured materials available as dispersion solutions into metal or ceramic matrices deposited by sputtering processes. The ability to imbed delicate and/or nanostructured materials within metal or ceramic matrices using this technique could have wide ranging applications beyond tribological coatings, such as biological and bio-inspired hybrid materials, directionally tailored thermal transport materials, and thermoelectrics. However, several challenges to

effectively integrating these processes were identified for the materials studied, i.e. undesired sputtering of carbon and poor adhesion between the dispersed solute and the film matrix. Because the interactions between sputtering and MAPLE processes can be complex, for each application the specific materials (magnetron sputter targets, MAPLE solute and matrix, substrate, etc.) and experimental conditions (background gas and pressure, laser parameters, substrate surface preparation, sputter sequences, magnetron power settings, solute concentration in the MAPLE target, etc.) need to be investigated and understood, resulting in synthesized films with desired properties.

In these studies, the potential of carbon nanopearls to create environmentally stable solid lubricants has been demonstrated for future aerospace needs. This development could drastically change current approaches of lubrication for space applications. Additionally a new MAPLE-sputtering process in which solvent-dispersed nano-scale materials are incorporated into metal and ceramic matrices was developed to enable synthesis of novel nanostructured hybrid materials for a variety of applications.

7 FUTURE STUDIES

Because of the technical challenges that the MAPLE/magnetron sputtering process presents, further process development is needed before the process is ready for use in aerospace solid lubricant thin films and other applications. This development might include exploration of alternate solvents or solvent blends to reduce or eliminate the amount of hydrocarbon species available for reaction or deposition onto surfaces, use of different background gases in which rate of the charge exchange reaction with the toluene would be decreased, or other process modifications. Another idea is to replace CNPs with nano-sized capsules of solid or liquid lubricant material in which the walls of the capsules are made of materials with strong adhesive bonding to the metallic matrix. This would have advantage of replenishing the lubricant as the coating wears and new capsules of lubricant are exposed. Another technical challenge for utilizing solid lubricants deposited using MAPLE or other pulsed laser techniques is to develop strategies for industrial scale production of these films.

REFERENCE LIST

- [1] Hirata, A., Igarashi, M., and Kaito, T.: Study on solid lubricant properties of carbon onions produced by heat treatment of diamond clusters or particles. *Tribology International* 37, 899-905 (2004).
- [2] Levesque, A., Binh, V. T., Semet, V., Guillot, D., Fillit, R. Y., Brookes, M. D., and Nguyen, T. P.: Monodisperse carbon nanopearls in a foam-like arrangement: a new carbon nano-compound for cold cathodes. *Thin Solid Films* 464-465, 308-314 (2004).
- [3] McGill, R. A., Chrisey, D. B., Pique, A., and Mlsna, T. E.: Matrix assisted pulsed laser evaporation (MAPLE) of functionalized polymers: Applications with chemical sensors. 3274, 255-266 (1998).
- [4] Pique, A., McGill, R. A., Chrisey, D. B., Leonhardt, D., Mlsna, T. E., Spargo, B. J., Callahan, J. H., Vachet, R. W., Chung, R., and Bucaro, M. A.: Growth of organic thin films by the matrix assisted pulsed laser evaporation (MAPLE) technique. *Thin Solid Films* 355-356, 536-541 (1999).
- [5] Pique, A., Wu, P., Ringeisen, B. R., Bubb, D. M., Melinger, J. S., McGill, R. A., and Chrisey, D. B.: Processing of functional polymers and organic thin films by the matrix-assisted pulsed laser evaporation (MAPLE) technique. *Applied Surface Science* 186, 408-415 (2002).
- [6] Toftmann, B., Rodrigo, K., Schou, J., and Pedrys, R.: High laser-fluence deposition of organic materials in water ice matrices by "MAPLE". *Applied Surface Science* 247, 211-216 (2005).
- [7] Pierson, Hugh O.: Handbook of carbon, graphite, diamond, and fullerenes: processing, properties, and applications. (1993).
- [8] Bhushan, B.: Introduction to Tribology. 267-277 (2002).
- [9] Fontaine, J., Donnet, C., Grill, A., and LeMogne, T.: Tribochemistry between hydrogen and diamond-like carbon films. *Surface and Coatings Technology* 146-147, 286-291 (2001).
- [10] Grierson, David S. and Carpick, Robert W.: Nanotribology of carbon-based materials. *Nano Today* 2, 12-21 (2007).

- [11] Donnet, C. and Grill, A.: Friction control of diamond-like carbon coatings. *Surface & Coatings Technology* 94-95, 456-462 (1997).
- [12] Voevodin, A. A., Donley, M. S., Zabinski, J. S., and Bultman, J. E.: Mechanical and tribological properties of diamond-like carbon coatings prepared by pulsed laser deposition. *Surface & Coatings Technology* 76-77, 534-539 (1995).
- [13] Ferrari, A. C. and Robertson, J.: Interpretation of Raman spectra of disordered and amorphous carbon. *Physical Review B (Condensed Matter)* 61, 14095-14107 (2000).
- [14] Kroto, H. W., Heath, J. R. O'Brien, S. C., Curl, R. F., and Smalley, R. E.: C₆₀: Buckminsterfullerene. *Nature* 318, 162 (1985).
- [15] Kratschmer, W., Lamb, L. D., Fostiropoulos, K., and Huffman, D. R.: Solid C₆₀: a new form of carbon. *Nature* 347, 354-358 (1990).
- [16] Huong, P. V.: Effect of laser annealing on the structure of fullerene C₆₀. *Materials Letters* 14, 80-82 (1992).
- [17] Harris, P. J. F.: Carbon nanotubes and related structures. (1999).
- [18] Ugarte, D.: Curling and closure of graphitic networks under electron-beam irradiation. *Nature* 359, 707-709 (1992).
- [19] Ugarte, D.: Onion-like graphitic particles. *Carbon* 33, 989-993 (1995).
- [20] Banhart, F.: Irradiation effects in carbon nanostructures. *Reports on Progress in Physics* 62, 1181-1221 (1999).
- [21] Sano, N., Wang, H., Alexandrou, I., Chhowalla, M., Teo, K. B. K., Amaratunga, G. A. J., and Iimura, K.: Properties of carbon onions produced by an arc discharge in water. *Journal of Applied Physics* 92, 2783 (2002).
- [22] Street, K.W., Marchetti, M., Vander Wal, R.L., and Tomasek, A.J.: Evaluation of the Tribological behavior of Nano-Onions in Krytox 143AB. *Tribology Letters* 16, 143-149 (2004).
- [23] Kuznetsov, V. L., Chuvilin, A. L., Butenko, Y. V., Mal'kov, I. Y., Gutakovskii, A. K., Stankus, S. V., and Khairulin, R. A.: Study of onion-like carbon (OLC) formation from ultra disperse diamond (UDD). *Science and Technology of Fullerene Materials Symposium* 105-110 (1994).
- [24] Cabioc'h, T., Jaouen, M., Denanot, M. F., and Bechet, P.: Influence of the implantation parameters on the microstructure of carbon onions

produced by carbon ion implantation. *Applied Physics Letters* 73, 3096-3098 (1998).

- [25] Chen, X. H., Deng, F. M., Wang, J. X., Yang, H. S., Wu, G. T., Zhang, X. B., Peng, J. C., and Li, W. Z.: New method of carbon onion growth by radio-frequency plasma-enhanced chemical vapor deposition. *Chemical Physics Letters* 336, 201-204 (2001).
- [26] Xu, B., Yan, X., Wang, X., Ichinose, H., and Xie, S.: Studies on the growth mechanism of nano-onion-like fullerenes in arc discharge. *Cailiao Rechuli Xuebao/Transactions of Materials and Heat Treatment* 22, 9 (2001).
- [27] Rettenbacher, A. S., Elliott, B., Hudson, J. S., Amirkhanian, A., and Echegoyen, L.: Preparation and Functionalization of Multilayer Fullerenes (Carbon Nano-Onions). *Chemistry - A European Journal* 12, 376-387 (2005).
- [28] Mordkovich, V. Z. and Takeuchi, Y.: Multishell fullerenes by laser vaporization of composite carbon-metal targets. *Chemical Physics Letters* 355, 133-138 (2002).
- [29] Koudoumas, E., Kokkinaki, O., Konstantaki, M., Couris, S., Korovin, S., Detkov, P., Kuznetsov, V., Pimenov, S., and Pustovoi, V.: Onion-like carbon and diamond nanoparticles for optical limiting. *Chemical Physics Letters* 357, 336-340 (2002).
- [30] Keller, N., Maksimova, N. I., Roddatis, V. V., Schur, M., Mestl, G., Butenko, Y. V., Kuznetsov, V. L., and Schlogl, R.: The catalytic use of onion-like carbon materials for styrene synthesis by oxidative dehydrogenation of ethylbenzene. *Angewandte Chemie - International Edition* 41, 1885-1888 (2002).
- [31] Joly-Pottuz, L., Martin, J. M., Dassenoy, F., Vacher, B., Mieno, T., and Ohmae, N.: Carbon nanotubes and onions as lubricant additives. *Proceedings of the World Tribology Congress III - 2005* 2005).
- [32] Miyoshi, K., Takeuchi, S., Suzuki, M., and Watanabe, M.: Solid lubrication by novel carbon-derived materials. *New Diamond and Frontier Carbon Technology* 15, 37-47 (2005).
- [33] Tomita, S., Sakurai, T., Ohta, H., Fujii, M., and Hayashi, S.: Structure and electronic properties of carbon onions. *The Journal of Chemical Physics* 114, 7477-7482 (2001).
- [34] Roy, D., Chhowalla, M., Wang, H., Sano, N., Alexandrou, I., Clyne, T. W., and Amaratunga, G. A. J.: Characterisation of carbon nano-onions

using Raman spectroscopy. Chemical Physics Letters 373, 52-56 (2003).

- [35] Belin, T. and Epron, F.: Characterization methods of carbon nanotubes: a review. Materials Science & Engineering B (Solid-State Materials for Advanced Technology) 119, 105-118 (2005).
- [36] Dresselhaus, M. S., Dresselhaus, G., Charlier, J. C., and Hernandez, E.: Electronic, thermal and mechanical properties of carbon nanotubes. Philosophical Transactions of the Royal Society London, Series A (Mathematical, Physical and Engineering Sciences) 362, 2065-2098 (2006).
- [37] Dresselhaus, M. S., Dresselhaus, G., Saito, R., and Jorio, A.: Raman spectroscopy of carbon nanotubes. Physics Reports 409, 47-99 (2005).
- [38] Mahanandia, P., Vishwakarma, P. N., Nanda, K. K., Prasad, V., Barai, K., Mondal, A. K., Sarangi, S., Dey, G. K., and Subramanyam, S. V.: Synthesis of multi-wall carbon nanotubes by simple pyrolysis. Solid State Communications 145, 143-148 (2008).
- [39] Wang, Z. L. and Kang, Z. C.: Pairing of Pentagonal and Heptagonal Carbon Rings in the Growth of Nanosize Carbon Spheres Synthesized by a Mixed-Valent Oxide-Catalytic Carbonization Process. Journal of physical chemistry 100, 17725-17731 (1996).
- [40] Serp, Ph, Feurer, R., Kalck, Ph, Kihn, Y., Faria, J. L., and Figueiredo, J. L.: A chemical vapour deposition process for the production of carbon nanospheres. Carbon 39, 621-626 (2001).
- [41] Qian, H., Han, F., Zhang, B., Guo, Y., Yue, J., and Peng, B.: Non-catalytic CVD preparation of carbon spheres with a specific size. Carbon 42, 761-766 (2004).
- [42] Dowson, D.: History of Tribology. 2nd, (1998).
- [43] ASM Handbook Vol. 18: Friction, Lubrication, and Wear Technology. (1992).
- [44] Bowden, F. P. and Tabor, D.: The Friction and Lubrication of Solids, Part I. (1950).
- [45] Archard, J. F.: Contact and Rubbing of Flat Surfaces. Journal of Applied Physics 24, 981-988 (1953).
- [46] Patton, S. T. and Zabinski, J. S.: Failure mechanisms of capacitive MEMS RF switch contacts. Tribology Letters 19, 265-272 (2005).

- [47] Barriga, J., Fernandez-Diaz, B., Juarros, A., Ahmed, S. I. U., and Arana, J. L.: Microtribological analysis of gold and copper contacts. *Tribology International* 40, 1526-1530 (2007).
- [48] Savage, R. H.: Graphite lubrication. *Journal of Applied Physics* 19, 1-10 (1948).
- [49] Yen, B. K., Schwickert, B. E., and Toney, M. F.: Origin of low-friction behavior in graphite investigated by surface x-ray diffraction. *Applied Physics Letters* 84, 4702-4704 (2004).
- [50] Muratore, C. and Voevodin, A. A.: Chameleon coatings: adaptive surfaces to reduce friction and wear in extreme environments. *Annual Review of Materials Research* (2008).
- [51] Zaidi, H., Le Huu, T., and Paulmier, D.: Influence of hydrogen contained in hard carbon coatings on their tribological behaviour. *Diamond and Related Materials* 3, 787-790 (1994).
- [52] Le Huu, T., Zaidi, H., and Paulmier, D.: Lubricating properties of diamond-like coating. *Wear* 181-183, 766-770 (1995).
- [53] Juai, R. and Bhushan, B.: Nanoindentation studies of sublimed fullerene films using atomic force microscopy. *Journal of Materials Research* 8, 3019-3022 (1993).
- [54] Thundat, T., Warmack, R. J., Ding, D., and Compton, R. N.: Atomic force microscope investigation of C_{60} adsorbed on silicon and mica. *Applied Physics Letters* 63, 891-893 (1993).
- [55] Schwarz, U. D., Allers, W., Gensterblum, G., and Wiesendanger, R.: Low-load friction behaviour of epitaxial C_{60} monolayers under Hertzian contact. *Physical Review B (Condensed Matter)* 52, 14976-14984 (1995).
- [56] Nakagawa, H., Kibi, S., Tagawa, M., Umeno, M., and Ohmae, N.: Microtribological properties of ultrathin C_{60} films grown by molecular beam epitaxy. *Wear* 238, 45-47 (2000).
- [57] Miura, K., Kamiya, S., and Sasaki, N.: C_{60} molecular bearings. *Physical Review Letters* 90, 055509-1 (2003).
- [58] Okita, S., Matsumuro, A., and Miura, K.: Tribological properties of a C_{60} monolayer film. *Thin Solid Films* 443, 66-70 (2003).
- [59] Blau, P. J. and Habberlin, C. E.: An investigation of the microfrictional behavior of C_{60} particle layers on aluminum. *Thin Solid Films* 219, 129-134 (1992).

- [60] Bhushan, B., Gupta, B. K., Van Cleef, G. W., Capp, C., and Coe, J. V.: Sublimed C₆₀ films for tribology. *Applied Physics Letters* 62, 3253-3255 (1993).
- [61] Zhao, W., Tang, J., Puri, A., Falster, A. U., and Simmons, W. B. J.: Frictional behavior of C₆₀ microparticle-coated steel. 383, 313-318 (1995).
- [62] Matsumuro, A., Takada, Y., Takahashi, Y., Senoo, M., and Kondo, I.: Consolidation of C₆₀ powder by a high-pressure technique up to 5.4 GPa and its mechanical properties. *Journal of Materials Science Letters* 18, 1633-1636 (1999).
- [63] Gubarevich, A. V., Usuba, S., Kakudate, Y., Tanaka, A., and Odawara, O.: Frictional properties of diamond and fullerene nanoparticles sprayed by a high-velocity argon gas on stainless steel substrate. *Diamond and Related Materials* 14, 1549-1555 (2005).
- [64] Ohmae, N., Matsumoto, N., Joly-Pottuz, L., and Kinoshita, H.: Application of onion-like carbon to micro and nanotribology. *Diamond and Related Materials* 16, 1227-1230 (2007).
- [65] Joly-Pottuz, L., Vacher, B., Ohmae, N., Martin, J. M., and Epicier, T.: Anti-wear and friction reducing mechanisms of carbon nano-onions as lubricant additives. *Tribology Letters* 30, 69-80 (2008).
- [66] Yanli, Y., Xiaomin, W., Junjie, G., Xiaowei, Y., and Bingshe, X.: Tribological property of onion-like fullerenes as lubricant additive. *Materials Letters* 62, 2524-2527 (2008).
- [67] Hirata, A. and Yoshioka, N.: Sliding friction properties of carbon nanotube coatings deposited by microwave plasma chemical vapor deposition. *Tribology International* 37, 893-898 (2004).
- [68] Turq, V., Ohmae, N., Martin, J. M., Fontaine, J., Kinoshita, H., and Loubet, J. L.: Influence of humidity on microtribology of vertically aligned carbon nanotube film. *Tribology Letters* 19, 23-28 (2005).
- [69] Dickrell, P. L., Sinnott, S. B., Hahn, D. W., Raravikar, N. R., Schadler, L. S., Ajayan, P. M., and Sawyer, W. G.: Frictional anisotropy of oriented carbon nanotube surfaces. *Tribology Letters* 18, 59-62 (2005).
- [70] Hu, J. J., Jo, S. H., Ren, Z. F., Voevodin, A. A., and Zabinski, J. S.: Tribological behavior and graphitization of carbon nanotubes grown on 440C stainless steel. *Tribology Letters* 19, 119-125 (2005).
- [71] Jacobs, O., Xu, W., Schadel, B., and Wu, W.: Wear behaviour of carbon nanotube reinforced epoxy resin composites. *Tribology Letters* 23, 65-75 (2006).

- [72] Jelinek, M., Kocourek, T., Remsa, J., Cristescu, R., Mihailescu, I. N., and Chrissey, D. B.: MAPLE applications in studying organic thin films. *Laser Physics* 17, 66-70 (2007).
- [73] Coburn, J. W. and Kay, E.: Pressure considerations associated with ion sampling from glow discharges. *Journal of Vacuum Science and Technology* 8, 738-743 (1971).
- [74] Coburn, J. W. and Kay, E.: Positive-ion bombardment of substrates in RF diode glow discharge sputtering. *Journal of Applied Physics* 43, 4965-4971 (1972).
- [75] Muratore, C.: The influence of particle energy distributions on reactively sputtered titanium oxide and titanium nitride thin film compounds. Ph.D. dissertation, Colorado School of Mines (2002).
- [76] Hager, C. H., Jr., Sanders, J. H., and Sharma, S.: Characterization of mixed and gross slip fretting wear regimes in Ti6Al4V interfaces at room temperature. *Wear* 257, 167-180 (2004).
- [77] Sellinger, A. T., Leveugle, E., Gogick, K., Peman, G., Zhigilei, L. V., and Fitz-Gerald, J. M.: Ejection of matrix-polymer clusters in matrix-assisted laser evaporation: experimental observations. *Journal of Physics: Conference Series* 59, 314-317 (2007).
- [78] Vacher, J. R., Jorand, F., Blin-Simiani, N., and Pasquiers, S.: Electron impact ionization cross-sections of toluene. *Chemical Physics Letters* 434, 188-193 (2007).
- [79] Ikezoe, I., Matsuoka, S., Takebe, M., and Viggiano, A.: Gas Phase Ion-Molecule Reaction Rate Constants Through 1986. (1987).
- [80] Landkammer, B., von Keudell, A., and Jacob, W.: Erosion of thin hydrogenated carbon films in oxygen, oxygen/hydrogen and water plasmas. *Journal of Nuclear Materials* 264, 48-55 (1999).
- [81] Cuesta, A., Martinez-Alonso, A., and Tascon, J. M. D.: Carbon reactivity in an oxygen plasma: A comparison with reactivity in molecular oxygen. *Carbon* 39, 1135-1146 (2001).
- [82] Cascarini De Torre, L. E., Bottani, E. J., Martinez-Alonso, A., and Cuesta, A.: Effects of oxygen plasma treatment on the surface of graphitized carbon black. *Carbon* 36, 277-282 (1998).
- [83] Pradhan, D. and Sharon, M.: Carbon nanotubes, nanofilaments and nanobeads by thermal chemical vapor deposition process. *Materials Science and Engineering B: Solid-State Materials for Advanced Technology* 96, 24-28 (2002).

- [84] Westwood, W. D.: Physical Vapor Deposition. Microelectronic Materials and Processes: Proceedings of the NATO Advanced Study Institute on Microelectronic Materials and Processes, Il Ciocco, Castelvechio Pascoli, Italy, June 30-July, 1986 133-201 (1989).
- [85] Yamamura, Y. and Tawara, H.: Energy Dependence of Ion-Induced Sputtering Yields from Monatomic Solids at Normal Incidence. Atomic Data and Nuclear Data Tables 62, 149-253 (1996).
- [86] Sliney, H. E.: Solid Lubricant Materials For High Temperatures - a Review. Tribology International 15, 303-315 (1982).
- [87] Spalvins, T.: A review of recent advances in solid film lubrication. Journal of Vacuum Science & Technology A (Vacuum, Surfaces, and Films) 5, 212-219 (1987).
- [88] Hunter, C. N., Check, M. H., Bultman, J. E., and Voevodin, A. A.: Development of Matrix Assisted Pulsed Laser Evaporation (MAPLE) for deposition of disperse films of carbon nanoparticles. Surface & Coatings Technology 203, 300-306 (2008).

R702035056